Performance of Nanocrystalline Coatings Under Combined Impact and Fatigue Loads

by

Katherine Daley

A thesis submitted in conformity with the requirements
for the degree of Master of Applied Science
Graduate Department of Aerospace Science and Engineering
University of Toronto

Abstract

Performance of Nanocrystalline Coatings Under Combined Impact and Fatigue Loads

Katherine Daley
Master of Applied Science
Graduate Department of Aerospace Science and Engineering
University of Toronto
2020

Nanocrystalline materials offer many advantages for use in aerospace structures due to their small grain size resulting in an increase in strength, toughness and hardness. Due to their high strength-to-weight ratio, nanocrystalline nickel-cobalt and pure cobalt coatings are under consideration for use in aircraft turbine engine fan blades. As fatigue performance is a critical component of the the design of aircraft structures, this thesis work investigates the combined effect of projectile impact up to 25 joules and fatigue loads on a nanocrystalline nickel-cobalt coating with an aluminum substrate. The experiments show coating stress is the strongest predictor of fatigue life, and impact energy is not strongly correlated with the fatigue failure. In addition, stress concentrations inherent in the test specimen geometry and the quality of electrodeposited coatings can have detrimental effects on the fatigue life. These factors must be carefully considered in applications of nanocrystalline coatings where they experience fatigue loads.

Acknowledgements

Firstly, I would like to acknowledge Pratt and Whitney Canada for generously providing funding for this project.

To my supervisor, Dr. Craig Steeves, thank you for the wonderful opportunity to study at the Advanced Aerospace Structures Lab. Thank you for your expert guidance, patience, and humour throughout my studies.

To all my lab mates, Dan, Bharat, Nick, and Steven, thank you for answering my many many questions on all things Matlab and Linux (and more!), and for making my time at UTIAS so enjoyable.

To Sam, without whom I could not have produced this thesis, an extra-special thank you for your unfailing kindness, generosity, and friendship. It was a complete delight working with you.

To my summer students, Isobel and Cole, thank you for all your invaluable smarts and hard work in helping me with my experiments.

To the UTIAS community, including students, professors, and staff, thank you for always being ready to help with all manner of things, including coursework, computer troubles, and lab-demolition services.

To Chris and Petra, thank you for your generous help with the stats (and beer!).

To my North York run crew, I could not have imagined a group of strangers with nothing in common but running outside in all manner of weather could have become such an important part of my life. Thank you for all the endorphins, cookies, and bRUNch!

To all my friends, in Toronto, Sault Ste. Marie, the Yukon, and beyond, thank you for your many words of encouragement and support over the past few years. Our times together are few and far between but you all inspired me to keep going!

To my brother- and sister-in-law, Robbie and Rachel, there are not enough words in the universe to say thank you for taking me in as one of your own for the past two years. To my nephews Evan, Matthew, and Jaxson, thank you for sharing your home with me; watching you grow up before my eyes has been like magic!

To my father-in-law Marty, and to Irwin and Joanne, thank you for always making me feel like part of the family.

To my parents, Claude and Sandra, and to my sisters, Eleanor and Marie, thank you for always believing in me and for always being there to talk about all life's trials and triumphs, large and small.

Finally, to my husband Aaron, thank you for giving me the courage to start, and finish, this thesis, and for always making me laugh, even from three time zones away.

Contents

List of Tables

List of Figures

Chapter 1

Introduction

1.1 Motivation

Titanium and titanium alloys have been widely used in the aerospace industry since the late 1950s [1]. These materials have many advantages including a high strength-to-weight ratio and good corrosion resistance. However, they are costly to extract, process, and shape, and have negative environmental and health impacts [2]. As aerospace companies like Pratt & Whitney Canada (PWC) look to reduce their carbon footprint, alternative materials that can compete with titanium alloys in terms of strength-to-weight ratio and cost, with less environmental impact are of great interest.

Use of nanocrystalline (nano) coatings on top of a light, relativity inexpensive substrate is being studied as one solution. A nano material is defined as having a grain size of one to 250 nanometres (nm) [3]. For comparison, conventional grain sizes in polycrystalline materials are in the range of 10 to 300 micrometres (μm). Nano materials have been shown to have many desirable properties, including greater strength, toughness, and hardness compared to coarser-grained materials. This difference may be due to the larger percentage of atoms that form the grain boundary. Nano coatings on top of a substrate have been shown to provide advantageous properties such as improved wear and corrosion resistance [4].

Knowledge about fatigue life performance is critical to design of aircraft structures, as fatigue is the cause of a significant number of failures [5]. This thesis is an investigation of the performance of these coatings under combined impact and fatigue loads, which has specific applications in aircraft turbine engine fan blades. The fan blades undergo high fatigue loading over their lifetimes [6] and are susceptible to impact damage for example from gravel on a runway or hail strikes [7]. The suitability of nano coatings for these fan blades, currently made from titanium, will be assessed based on the results of this work. On a broader level, the goal of this research is to gain insight into how impact damage correlates to the overall

fatigue life of the coating-substrate system.

1.2 Previous Work at UTIAS

1.2.1 Fatigue Testing on Nano Coated Specimens

The University of Toronto Institute of Aerospace Studies (UTIAS) has previously studied the fatigue performance of nano nickel (nNi) and nano cobalt-phosphorous (nCoP) coatings on aluminum 7255 substrates [8]. This study showed that the quality of the coating was critical in determining an increase or a decrease in fatigue life compared to that of an uncoated substrate. In cases where the coated specimens had a lower fatigue life than uncoated ones, several factors were noted as potential causes, including defects in the substrate, flaws in the nano coating, and debonding of the coating and the substrate.

Inspection with a scanning electron microscope (SEM) detected the flaws in the coating, which reduced the fatigue life of those samples to less than the uncoated samples (see Figure 1.1). The type of coating (nNi or nCoP) also affected the failure mode. The nNi coating failed well before the substrate, and in a different location from the substrate failure.

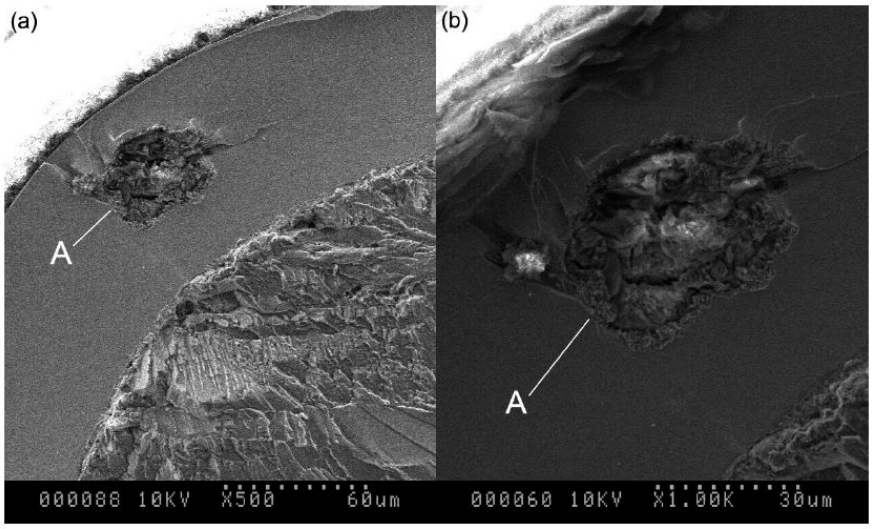

Figure 1.1: SEM image of a nano-coated specimen fatigue fracture surface, showing a defect in the nCoP coating at location A [8].

The nCoP coating and the substrate both failed at the same time and location. It was found that, if there were no flaws or defects, the nCoP coating extended fatigue life. Two distinct populations were identified for each material type and thickness, showing distinct high and low cycles-to-failure groups. The Al substrate material also had irregular geometry outside specified tolerances, with defects detected after failure. Some specimens of uncoated Al 7255 failed unexpectedly and abruptly after the first indications of failure.

Measurements of the strain field in each sample during testing were obtained using Digital Image Correlation (DIC). Each sample was painted with a speckle pattern, allowing the relative position of different points on the surface to be measured over time as the sample was deformed. A typical strain field is shown in and Figure 1.2.

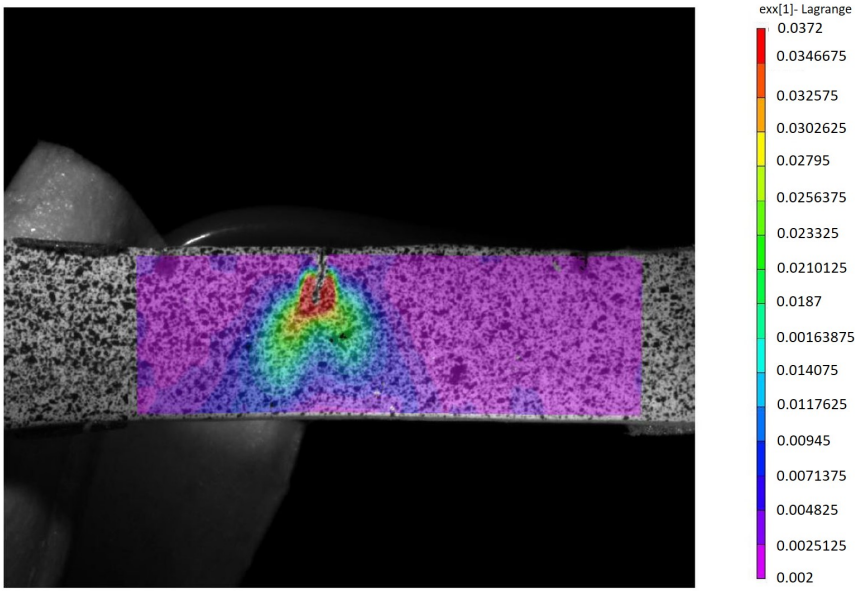

Figure 1.2: Typical strain field indicating the presence of a fatigue crack in an Al 6061 specimen [8].

1.2.2 Impact Testing

A feasibility study for nano-coated composite pipes was done at UTIAS in 2013 [9]. Design parameters of the gas gun include projectile diameter, the gun barrel inner diameter and length, gas reservoir volume, and initial gas pressure. The pressure was measured using a silicon cell pressure transducer, and the projectile velocity exiting the gun was measured using three fibre optic sensors. The impact experiments on the test samples were used to calculate the ballistic limit, which is the velocity where a given projectile will fully penetrate the test sample 50% of the time. A detailed study on the design of a gas gun for use in impact tests was performed by Gottlieb [10]. This study provided guidance in the design of the gas gun that was used for this project.

1.3 Thesis Outline

1.3.1 Literature Review

Fatigue is defined as the progressive damage of a material under repeated cyclic loading [11]. Fatigue damage is considered to be a stochastic process, and fatigue life data for

identical test specimens show a large amount of scatter. Many factors can affect fatigue life including alignment of the test machine, specimen geometry, surface stress concentrations, which includes impact damage, material grain size, and flaws or inclusions on the coating and substrate. As part of the literature review in Chapter 2, many of the these factors were investigated. There are many studies that separately consider fatigue testing, impact damage, behaviour of coated systems, and the material properties and synthesis methods of nano materials. However, there are few which combine impact damage with fatigue testing on nanocrystalline coatings.

1.3.2 Experimental Setup

The experimental setup, discussed in Chapter 3, was designed to investigate the effects of two different coating types, thicknesses, and impact energy levels have on the resultant fatigue life. A total of 60 nano-coated Al 6061-T6 dogbone specimens were manufactured by Integran Technologies Inc. Two coating types, nickel cobalt (nNiCo), known as Nanovate N1210, and pure cobalt (nCo), known as Nanovate R3310, were electrodeposited in two thicknesses, 100 µm, and 250 µm. Fifty uncoated Al 6061-T6 flat specimens were made at the University of Toronto's Mechanical and Industrial Engineering (MIE) Machine Shop to the same geometric specifications.

After calibrating the gas gun, 25 specimens were tested at various impact energy levels, ranging from 2.5 to 25 joules (J), using the same spherical projectile. The impact energy was based on the velocity of the projectile, which was determined by the initial pressure in the gas gun reservoir. The velocity was measured by calculating the time required for the projectile to pass between a fixed distance between two laser gates. During the impact tests the specimens were supported from the back to prevent any bending to isolate the effect of the surface damage.

The impact test specimens and 27 additional specimens underwent force-controlled fatigue testing to failure using an MTS 800 universal testing machine. Strain was measured using three methods, strain gauge, laser extensometer, and digital image correlation.

1.3.3 Analysis

Chapter 4 discusses the analysis of the fractured specimens, specifically the relationship between fatigue life and coating type, coating thickness, and impact energy. DIC analysis was done before and after the impact test, and during the fatigue test. SEM images were taken of several specimens to determine the true cross-sectional area of the test specimens, and to pinpoint the failure origin on the fracture surface. The effect of residual stresses, possibly as a result of the nano coating electrodeposition process, was also investigated.

1.3.4 Conclusions & Recommendations

Finally, Chapter 5 presents the conclusions of this research, and provides several recommendations for future experimental work on this topic. In general, it was found that the coated specimens performed worse in fatigue than the uncoated specimens. The fatigue life is considerably dependent on the stresses in the coating, on interior and exterior coating flaws, as well as the specimen geometry. The experimental results also showed a minimum threshold impact energy below which other fatigue failure initiation mechanisms take precedence over the impact damage.

Chapter 2

Literature Review

2.1 Overview

There are few, if any studies that investigate the combination of impact and fatigue loading on nanocrystalline coatings. Consequently, much of this literature review considers research in each of the following areas: nanocrystalline material properties and synthesis, fatigue of materials, induced stresses and their effect on fatigue life, and impact testing.

2.2 Nanocrystalline Materials

Gleiter [12] provides an overview of nanocrystalline materials, defining them as having a characteristic length on the order of 10 nm. Nano materials are described as microstructurally heterogeneous, meaning they consist of the crystallites themselves and the grain boundaries, which is the region between the crystallites. Crystallites, or grains, are the "building blocks" of the material structure. This heterogeneous structure is illustrated in Figure 2.1. This paper focuses on bulk solids with a nanometre-scale microstructure, rather than nano coatings. However, Gleiter describes a fundamental principle in the material science of solids, which is that the microstructure determines the material properties. The microstructure includes the chemical composition, atomic arrangement, and the dimensionality of the solid. Controlled manipulation of these parameters will change the macroscopic material properties. For example, diamond and graphite have dramatically different hardness due to the different atomic arrangement of their carbon atoms. The reduced grain sizes and increased grain boundaries of nanocyrstalline materials help to explain why their properties are different from coarser-grained materials with the same chemical composition.

Meyers et al. [3] reviews the research progress made in the field of nano materials following Gleiter's research. A nano material is defined having a grain size of one to 250 nm (a wider range than Gleiter). "Conventional" grain sizes are given as 10 to 300 µm. Figure 2.2 shows

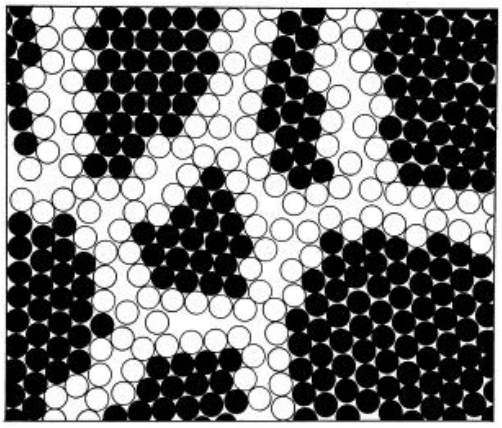

Figure 2.1: Heterogeneous microstructure a nano material. The black circles indicate the crystallite atoms, and the open circles indicate the grain boundary atoms [12].

an SEM image of a nano and polycrystalline diamond coating on a silicone substrate, showing the difference in scales between the grain sizes.

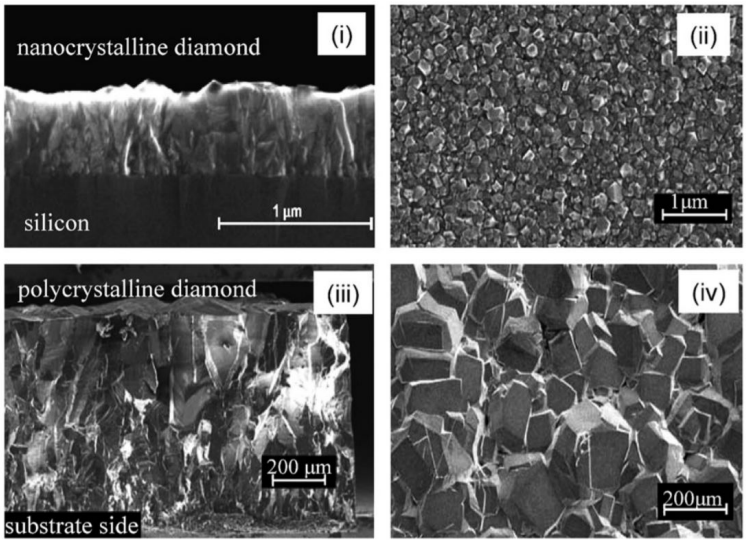

Figure 2.2: SEM images of nanocrystalline (subfigures(i) and (ii)) polycrystalline (subfigures (iii) and (iv)) diamond coatings on a silicon substrate. The average grain size of the nano coating is reported as 40 nm (or 0.4 µm) and 160 µm in the polycrystalline coating [13].

Nano materials have been shown to have many desirable properties, including greater strength, toughness and hardness compared to coarser-grained materials. This difference may be due to the larger percentage of atoms that form the grain boundary. The detrimental effect of synthesis- or manufacturing-induced defects on material properties such as yield strength, ductility, strain hardening, strain rate sensitivity, creep, and fatigue is extensively discussed. Further discussion on yield strength and fatigue are found in Sections 2.2.1 and 2.3.1, respectively.

Barai and Weng [14] discuss how the constitutive models of nano materials have been improved over time. Experiments showed that there is not a constant stress distribution in both the grains and the grain boundaries. The boundaries are softer than the grain interiors, and have rate-dependent plastic behaviour. However, as discussed by Zhu et al [15], there is not yet consensus on how to calculate the grain boundary thickness properly.

2.2.1 The Hall-Petch Effect

The phenomenon whereby the grain size of a material is inversely proportional to yield strength is known as the Hall-Petch effect. There is debate on whether or not the Hall-Petch relation holds or reverses for nanometre-sized grains [3]. Meyers et al. conclude that there is likely a plateau in the yield strength below grain sizes of 10 to 15 nm. An increase in yield strength leads to an increase in fatigue life, though faster crack-growth velocities have also been observed, compared with coarse-grained materials. It is thought the very small grain sizes provide a "smoother path" for crack growth, and the dominant plastic deformation mechanisms depend on the grain size, even within the nano material classification. Experiments show that the ductility is strongly dependent on the type of deformation mechanism.

The breakdown of the Hall-Petch relation is discussed in several papers on nano materials. Trelewicz and Schuh [16] show in quasi-static tests on nickel-tungsten alloys, the Hall-Petch relation no longer is evident at grain sizes of 20 nm or less, indicating a peak in yield strength at that grain size. However, in dynamic indentation tests, a peak in yield strength was observed at a grain size of 12 nm.

The out-of-plane loading conditions showed a critical grain size (i.e. where the maximum strength was observed) was 16 nm in compression and 18 nm in tension [14]. The in-plane loading conditions showed a critical grain size of 35 nm in compression and 38 nm in tension. The shear loading case showed a critical grain size of 35 nm. The authors state that the differences in critical grain sizes between the difference conditions are due to the fact that the nano grain boundary regions are anisotropic.

2.2.2 Synthesis techniques

There are many methods for fabricating nano metals, as outlined by Meyers [3], including inert gas condensation, mechanical alloying crystallization from amorphous solids, and severe plastic deformation. Electrodeposition was used by Integran to coat the test specimens used in this thesis work. The substrates and coating material are placed in a bath containing metal salts. Once a current is passed between then, the substrate acts as the cathode and negatively charged ions of the coating material are deposited. Applying the current as a pulse will cause grain refinement, as illustrated shown in Figure 2.3.

Electrodeposition of cobalt-nickel-phosphorous coatings is discussed by Ma et al. [18]

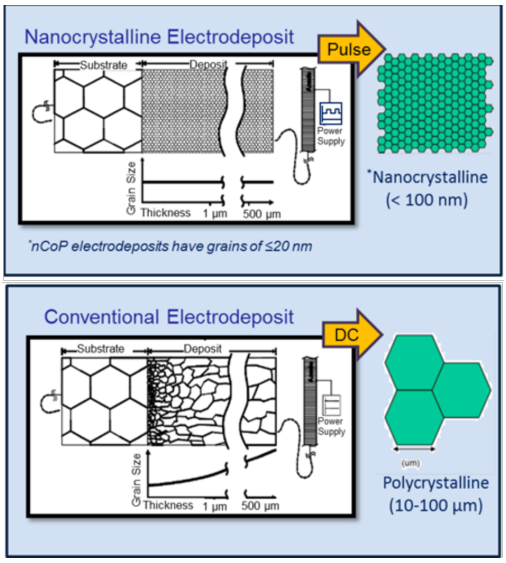

Figure 2.3: Electrodeposition technique for a nanocrystalline metal (cobalt-phosphorous, Co-P) and for coarser-grained polycrystalline material [17]. This technique was used to coat the test specimens for this research.

as a replacement for hard chromium, due to the wear and corrosion resistance. The main advantage of the electrodeposition method is that it provides good coating performance (such as uniformity of thickness, which will affect the overall effectiveness of the coating) at a low cost and high speed, compared to other methods such as inert gas condensation [3].

Mroz et al. [19] discuss a potential detriment to the electrodeposition process. Hydrogen is produced during the cathode reaction and may diffuse into the substrate and cause embrittlement, though there is not much data on how much is produced. Several other studies look at residual stresses caused by electrodeposition, discussed further in Section 2.3.2.

2.2.3 Nanocrystalline Coatings

Barai and Weng [14] look at how to relate a peak in strength of a nano coating to a critical grain size, using a computational model of the coating as a plane-stress plate consisting of zones representing the grain boundaries and grain interiors. A coating with high strength will also have good performance in terms of wear resistance and hardness, which are all desirable properties. Since many studies consider bulk materials, the authors decided to look at how to develop stress-strain curves for a two-dimensional surface coating. The cross-section of the coating was made up of columnar grains through the thickness, with harder grain interiors and softer grain boundaries. An effective stiffness was calculated in order to develop the stress-strain relation for the coating, which behaves anisotropically. A diagram of the grain interior and boundary is shown in Figure 2.4.

The derived stress-strain equations were used to generate curves for both tensile and

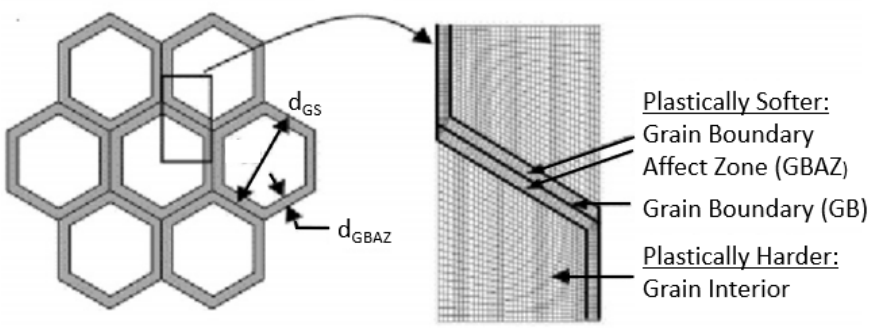

Figure 2.4: Diagram of a nanocyrstalline grain, showing the grain boundary, grain interior, grain size diamter (d_{GS}) and grain boundary thickness (d_{GBAZ})[14].

compressive loads in in- and out-of-plane directions for a zircronium nitride coating. The out-of-plane stress-strain curves at a range of grain sizes are shown in Figure 2.5. The material experiences a hardening as the grain size decreases from 100 to 20 nm, as expected by the Hall-Petch effect, then a softening from 20 nm to 10 nm, as the volume fraction of the softer grain boundary increases. The difference in stress between tension and compression, called the strength differential, is most pronounced at a grain size of 10 nm. The in-plane stress-strain curves are shown in Figure 2.5, and show a hardening as grain size decreases from 200 nm to 30 nm. The strength differential is again highest at a grain size of 10 nm. The authors state their work will help in determining a critical grain size, i.e. the grain size which provides the greatest strength. This critical grain size may change depending on the loading direction and whether the load is in tension or compression.

The toughness of nano coatings and films is discussed by Zhang et al. [20]. This paper discusses the importance of bonding between the coating and the substrate. The resistance to delamination is equally important as resistance to crack initiation in determining how long a material can withstand a certain load. The authors model the coating as a plane-stress composite plate with grains as through-thickness columns, where the normal and shear stresses are assumed to be zero.

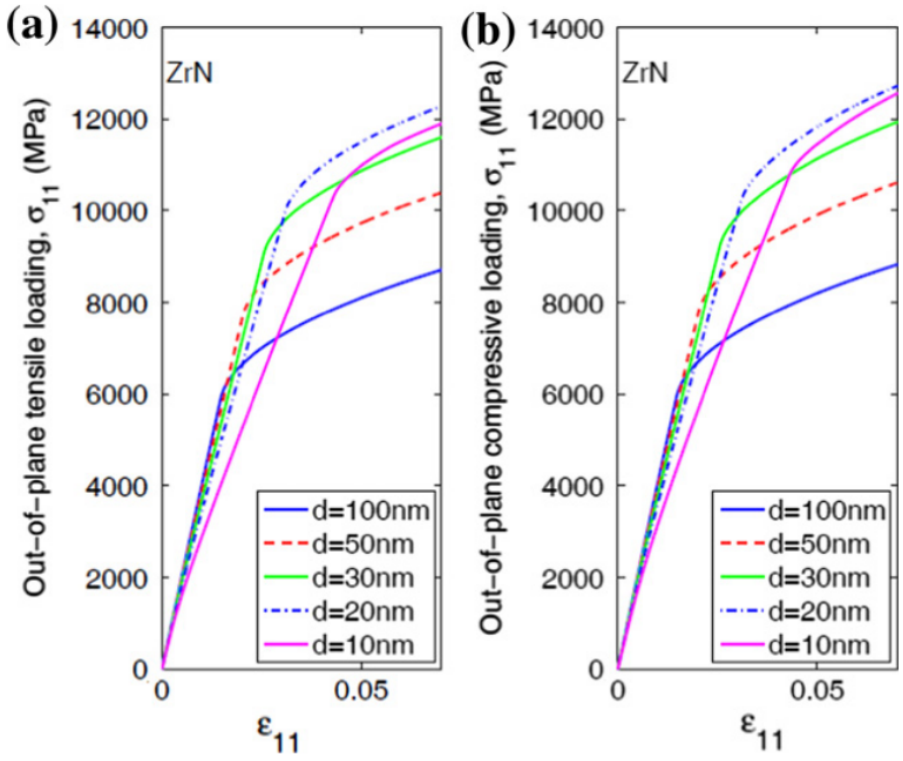

Figure 2.5: Tension (a) and compression (b) out-of-plane stress-strain curve of nano ZrN coating at various grain sizes [14].

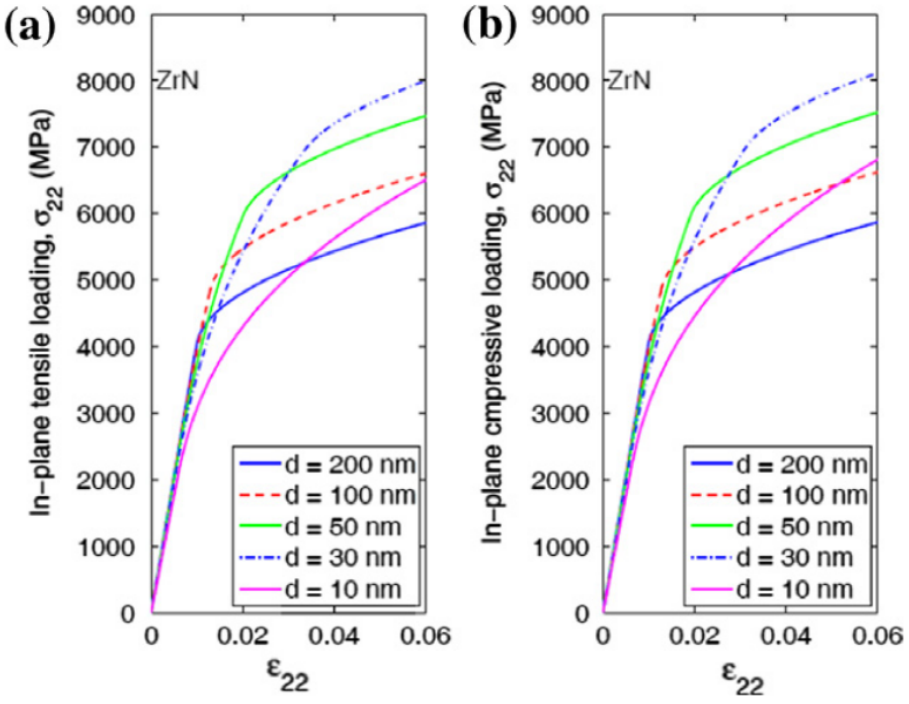

Figure 2.6: Tension (a) and compression (b) in-plane stress-strain curve of nano ZrN coating at various grain sizes [14].

2.3 Fatigue

Suresh [11] provides a comprehensive treatment on many aspects on fatigue failure in various materials. The first research on fatigue was done in the middle of the 19th century, and became more necessary with the development of bridges, railways and eventually aircraft, when unexpected and catastrophic failures were observed. Mechanical fatigue is defined as a change in material properties based on application of cyclic stresses or strains. Fatigue failure occurs at a peak load much smaller than a static failure load, and is the result of the growth of a single dominant flaw. The failure is characterized by the presence of striations, which are ripples on the fracture surface indicating the rate of crack growth. Total fatigue life is the number of cyclic cycles (N) needed for failure of a test specimen at a specified stress (S). Repeating a fatigue test many times at many stress levels will produce the material's S-N curve. An example of an S-N curve of Al 6061-T6 is shown in Figure 2.7. The maximum applied load is 43 ksi, or about 296 MPa, which is the tensile strength according to Kaufman [21]. The R value refers to the ratio of minimum to maximum applied stress during the loading cycle. If the specimen is in compression at the minimum stress, the R value is negative.

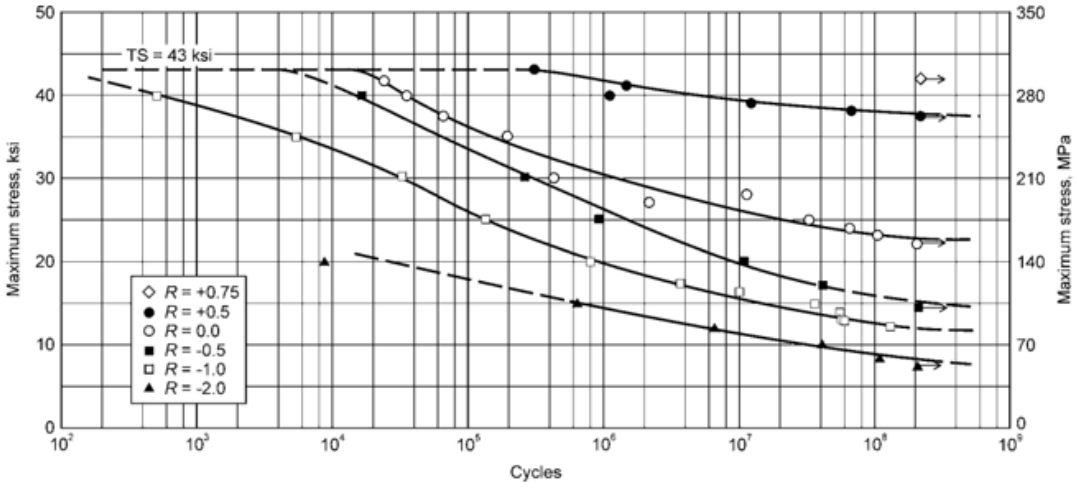

Figure 2.7: S-N curve of Al-6061 rolled bar under axial stress at various R values [21].

There are two broad types of mechanical fatigue: high-cycle and low-cycle. In high cycle fatigue, the maximum stress applied to a specimen during the loading cycle is below the elastic yield point for the material. Low-cycle fatigue applies a stress in the plastic zone, and will cause permanent deformation and generally will have a fatigue life of less than 10^5 cycles [22]. Certain materials have a fatigue limit, which is a stress below which fatigue damage or failure will not occur, even after millions of cycles. Steel, for example, has a well defined

fatigue limit, though aluminum does not.

Suresh [11] outlines the general progression of fatigue damage upon application of a cyclic load as follows: nucleation of permanent damage in the microstructure along a slip direction; formation of microscopic cracks, known as stage 1 cracking; growth of the cracks into a dominant crack; stable propagation of the dominant crack, with the formation of striation, known as stage 2 cracking; and final failure. Figure 2.8 shows an example of a stage 1 and stage 2 crack in a ductile polycrystalline material, where the crack initiated at an extrusion on the material surface.

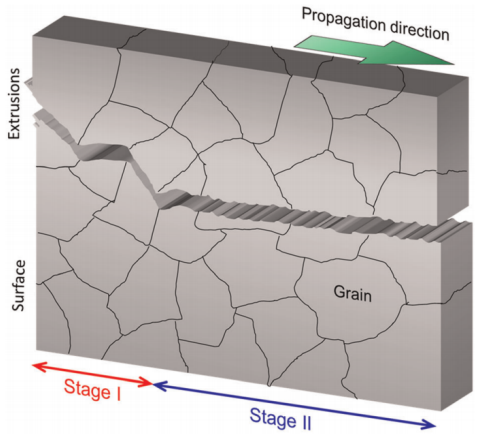

Figure 2.8: Diagram of a stage 1 crack, which is on the scale of the microstructure, and a stage 2 crack, characterized by a higher stress state and the formation of striations [23].

Surface roughness has been identified as a common location for fatigue crack initiation, and polishing test specimens has been shown in some cases to improve greatly the fatigue life. Crack propagation rate is dependent on many factors including the applied stress, the geometry of the crack, test frequency, and the environmental conditions of the test. In stage 1, plastic deformation confined to a few grain diameters. In stage 2, the stress intensity is increased and the crack progresses independently of the grain boundaries. Striations formed at this stage, and their spacing correlates to average crack growth rate per loading cycle, which can be used in post-failure analysis as a history of the crack growth. An SEM image of fatigue striations in an aluminum specimen is shown in Figure 2.9.

Much of the literature on fatigue performance and deformation mechanisms are on high purity metals where the crystal structure is well known and controlled. The manufacturing process and impurities found in "commercial materials" such as those used in this thesis work will have an impact on the fatigue failure mechanisms. Suresh [11] notes it has been shown many times that a small change in the microstructure of a component will lead to a substantial difference in the fatigue life and failure mechanism.

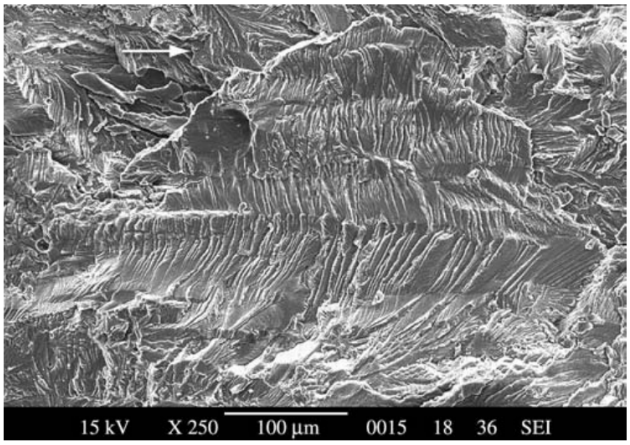

Figure 2.9: SEM image of striations from a stage II crack in a Al 2024 fatigue test specimen. The white arrow indicates the crack propagation direction [23].

2.3.1 Fatigue of Nanocrystalline Coatings

In general, improved fatigue life of nano metals compared to conventional polycrystalline materials is due to the smaller grain sizes, and the larger volume fraction of the softer grain boundaries, as previously discussed. However, Padilla et al. [24] list several instances where grain growth has been seen in the local areas of crack formation and propagation after tension-tension fatigue loading, which would then reduce the overall fatigue life. Fatigue cracks are observed to begin at both sites of internal and surface defects. The electrodeposition process may result in impurities, inclusions, precipitates and residual stress, among other sources of defects, which will affect the fatigue life. Bouzakis et al. [25] investigate the interface fatigue strength of diamond nano coatings on cemented carbide substrates. The bonding strength of the diamond coating over repetitive loading is a critical factor when determining the useful life of a cutting tool. The interface toughness is evaluated using the inclined impact test, then the tangential and normal interface stiffness and the shear failure stress can be calculated. Over repetitive loading, the interface bond is damaged, leading to lifting and failure of the coating, characterized by bulging caused by the release of residual stresses developed when the coating was produced. Debonding between the coating and the substrate has been observed in nNi fatigue tests done at UTIAS [8].

In the experiments by Bouzakis et al., cylindrical test specimens were coated using hot filament chemical vapour deposition, to a thickness of 5 µm. Scanning electron microscopy (SEM) and dispersive X-ray analysis were used to examine the structure and composition of the coating, though the grain size of the coating was not mentioned. A cyclical load was applied for a constant impact time of 1 ms at an inclination of 15°. The heights of the bulges that developed in the coating were measured using confocal microscopy. At the maximum

load of 850 N, cracks quickly developed in the interface region, and bulges in the coating were observed after 40,000 cycles. The coating was considered totally destroyed after an additional 10,000 cycles. At a load of 750 N, the delamination of the coating was slower; bulges were observed forming at 70,000 cycles, and failure occurred after an additional 70,000 cycles. At 730 N, no damage to the coating was observed after 1.5 million cycles, so this was considered the critical load associated with the fatigue strength of the interface.

2.3.2 Influence of Induced Stress on Fatigue

Residual stresses are defined as those existing within a material when no external loads are applied. Rossini et al. [26] provide an overview of how to measure these stresses in bulk material. They affect many material properties, including fatigue life. Residual stresses originate in manufacturing and processing operations, such as machining and electrodeposition. In terms of fatigue life, compressive residual stresses are often considered beneficial to a component, since crack propagation is prevented, while tensile stresses are considered detrimental. For coatings or films, while residual stresses might be a substantial fraction of the overall applied stress, they are rarely measured or reported in the literature [24].

The methods used to measure residual stresses are classified as to how destructive they are to the component. Destructive techniques rely on removing a significant amount of material. For example, the sectioning technique relies on measuring the strain on the surface while removing successive strips of material. This method provides good results but does not preserve the specimen. An example of a semi-destructive technique is hole-drilling. Using a strain gauge on the surface of the specimen, the change in strain is measured as a hole is drilled through the thickness, releasing the residual stresses. This technique is considered more practical than destructive techniques, and the specimen is better preserved. X-ray diffraction (XRD) is a non-destructive technique and perfectly preserves the component. XRD measures the atomic spacing while a control specimen is under a known loading condition, and compares the results to the specimen of interest. The disadvantage beyond the equipment needed is that the x-rays can only reach a short distance under the surface. El-Sherik et al. used XRD was used to look at residual stresses in nNi electrodeposits [27]. Three thicknesses of coatings, 10 μm, 25 μm and 75μm with two grain sizes, 10 nm and 5 μm, were deposited on various types of substrates. It was found that the residual stresses were most effected by the substrate type, specifically the greater the difference in the lattice parameters (i.e. the dimensions of the crystal structure) relative to that of the coating, the greater the residual stresses.

Pathak et al. [28] discuss the effect of higher current density during electrodeposition plating, which increases the speed of manufacture and increases the possible plating thickness has

been shown to increase the residual stresses in the coating. The experimental results on electrodeposited microcrystalline nickels, which are highly anisotropic, showed the shape of the grains and their orientation in the cross-section changed with an increase in current density. The residual stress, hardness, and grain size increased as the current density increased, while the effective modulus decreased. The coating thickness was also investigated, and ranged from 18 μm to 90 μm. Creating a thicker coating in general leads to a lower residual stress, and the increase in residual stresses with increasing current density was less pronounced in thicker coatings. The calculation of the residual stress was based on the material properties of the nickel, plus the change in curvature of the substrate before and after coating.

Hadian and Gabe [29] looked at not only current density when considering residual stresses but also the bath composition and pH, number of cycles, and coating material. They also considered how to measure the residual stresses during the plating process. An alternative to measuring the deflection of the specimen is to use an internal stress meter, which measures the change in length (expansion or contraction) of the substrate using a type of dial gauge. Higher current densities resulted in better adhesion in smaller grain sizes when used in conjunction with pulse plating (i.e. current is applied at a specific on/off ratio). Pulse plating lead to harder coatings compared with a direct current method. Lower current densities caused higher tensile stresses; this effect is more pronounced in thin coatings (10 μm) compared to thick ones (25 μm), and seems to be opposite the trend observed in Pathak et al. [28]. However, Hadian and Gabe [29] considered many more variables which each had an effect, and considered larger current densities.

2.4 Impact Tests

Borvik et al. [30] performed gas gun tests to study the perforation of steel plates by various projectile shapes (flat, hemispherical, and conical). The results show the nose shape greatly affects the impact response of the target. The authors proposed the following kinetic energy transfer: some of the energy goes into deforming of the target (for example, global bending), some into local plastic deformation near the impact site, and the remainder into deformation of the projectile. Morniere et al. [31] discuss modelling impact damage and dynamics of fibre-metal laminates, with particular consideration of thin layers (in particular, aluminum alloy alternated with fibre glass), rather than thick plates. The damage area after impact is affected by the buckling of the debonded aluminum layers, the stacking sequence of the layers, and metal cracking on the non-impacted side. The impact response was divided into three stages; indentation, perforation, and penetration, shown in Figure 2.10. These stages were also used when developing a numerical model of the impact.

The amount of energy absorbed in the delamination of the layers was found to be a

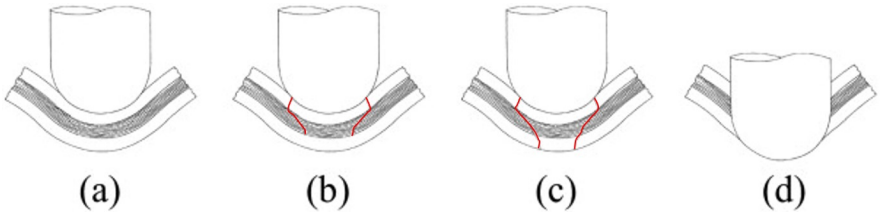

Figure 2.10: Stages of impact for a fibre-metal laminate: a) indentation; b) partial perforation; c) complete perforation; and d) penetration [31].

function of the impact speed and the size of the indenter. The relative sizes were not discussed, but small indenters caused the impact energy to be dissipated though cracking at the impact site and delamination, while large indenters caused the energy to be dissipated through deformation of the global structure.

Li et al. [32] considered the influence of impact on fatigue, specifically the effect of different projectile shapes. Two-mm thick dogbone specimens were hit with a drop indenter at various heights to control the impact energy, which ranged from 13 to 52 joules, using three different projectile shapes (spherical, conical and u-shaped). Tension-tension fatigue tests were done on the indented specimens, as well as on intact and pre-deflected specimens. The applied stress was set to 150 MPa, which corresponds to 50 % of the yield strength of the material, with an R value of 0.06. Four specimens from each group were tested, for a total of 48 specimens. The results showed the pre-deflected specimens had similar fatigue life to the intact specimens. The dented specimens had a lower fatigue life than the intact specimens, and predictably the fatigue life reduction corresponded to the impact depth. The shape of the projectile did affect the growth rate of the "macro" crack, that is, a crack that can be observed with the naked eye. The conical indentor increased the crack growth rate while the while the spherical and u-shape indentors slowed the growth rate. The hardened plastic zone around the indentation site, which has strengthening effect on the fatigue life, is damaged due to the sharp point of the conical indentor.

Draper et al. [33] studied the effect of ballistic impact on the high cycle fatigue performance of titanium turbine fan blades. The specimens had a dog-bone profile with an elliptical cross-section, similar to the leading edge of the turbine blade. In order to look at the influence of a large number of variables on the fatigue life, including projectile impact energy, projectile hardness, ambient temperature, thickness of the test specimen, impact locations on the test specimen, an analysis of variance (ANOVA) method was used to model the effects, and determine the relative significance of each variable. The experiment was divided into several phases. The first phase looked at the effect of various impact energies, ranging from 0.33 J to 2 J, and two projectile sizes. The range of impact energies represent impacts from "domestic" debris coming from inside the engine, rather than "foreign, which come

from the external environment. Once a suitable projectile diameter was determined, design of experiments principles were applied to determine which variables were had a significant effect on the fatigue life. The selected variables for the remaining phases of the experiment were energy of impact, specimen thickness, and projectile hardness. In the final phase, the specimens were tested at two impact energies, 0.71 J and 1.52 J, and at four load ratios. The energy levels were represented expected damage coming from within the engine itself, such as fragments from honeycomb seals or coatings, rather than foreign objects such as hail strikes. Four specimens were tested for each combination of impact energy and load ratio. The results showed that the impact energy had the biggest effect on fatigue life of the variables considered in the study. Crack length was measured post-impact using SEM and was determined to be the strongest predictor of remnant fatigue life.

2.4.1 Impact and Nanocrystalline Materials

Zhu et al. [15] investigate impact behaviour and deformation mechanisms of bulk nano nickel under high strain rates using a split hopkinson pressure bar impact experiment. The bulk nano nickel was synthesized by high-energy ball milling, whereby the nanostructure is achieved by repeated deformation of the material [3]. The specimens had a grain size of approximately 50 nm at the start of the test, measured using x-ray diffraction [34]. The specimens were tested at strain rates of 961 s^{-1}, 1107 s^{-1}, and 1330 s^{-1}. They were also tested at a quasi-static rate of 10^{-4} s^{-1}. The results showed a higher impact strength as the strain rate increased, and a relation of the deformation mechanisms of nano materials to the strain rate.

The authors theorize that this phenomenon is due to the fact that plastic deformation in nano metals is due to grain boundary sliding in combination with dislocation gliding. It has been accepted that dislocation gliding is the main plastic deformation mechanism for coarse-grained materials, and grain boundary sliding is the main mechanism for nano-grained materials, due to the increased volume fraction of the grain boundary. However, due to the high strain-rates, the dislocation gliding is thought to have an effect since there was generation of pile-ups in the grain interior. A constitutive model was developed using these two deformation mechanisms, which was able to predict the impact yield strength seen in the experiments.

The model divided the nano material into two phases, the grain interior and the grain boundary, as shown in Figure 2.11). The grain boundary was further divided into two parts, the four side layers around the cubic grain, and the two top and bottom layers. The volume fraction of each phase and part was expressed as a function of the grain size and the grain boundary thickness, which is used to calculate the overall material stress and strain.

Each volume fraction is used when calculating the overall stress and strain; the material is effectively modelled as a composite.

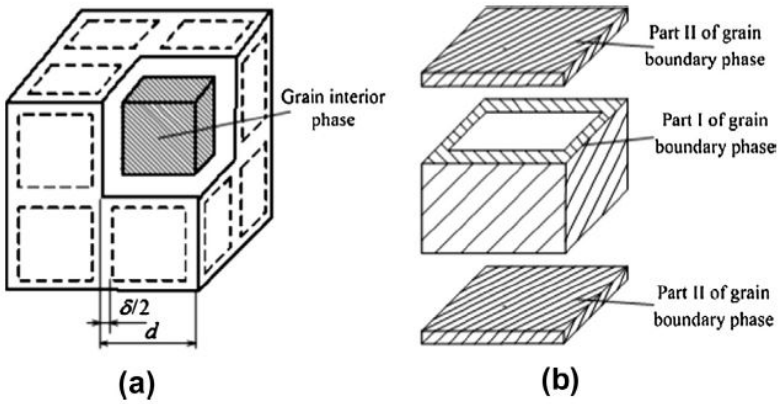

Figure 2.11: Constitutive nano material model showing a) the unit cell, where δ is the grain boundary thickness and d is the grain size, and b) the grain interior and grain boundary phases [15].

Karimpoor et al. [35] conducted Charpy impact tests, which determine the amount of energy absorbed during fracture of a notched sample as a measure of toughness, on both bulk nano and polycrystalline cobalt. Nano cobalt is mentioned as an environmentally friendly alternative to chromium coatings. The 2.5 mm thick nano cobalt, synthesized by electrodeposition with a grain size of 18 nm is compared to 10 mm thick polycrystalline cobalt with grain sizes of 1 µm and 10 µm. The grain sizes were measured using x-ray diffraction. As expected due to the Hall-Petch relation, where yield strength increases as grain size decreases, the hardness of nano cobalt was measured as twice that of polycrystalline cobalt.

However, the authors note that in their study the toughness did not improve as the grain size decreased from 10 µm to 18 nm. It has been shown in other nano materials that fracture toughness improves as grain size decreases down to a critical grain size [3]. The authors theorize that this may be because the expected toughness values were derived from thin tensile specimens under quasi-static load (i.e. about 0.2 mm thick), which might not be comparable to those obtained during high strain rate impact tests on thicker bulk specimens (2.5 mm). Another study on nano diamond coatings was performed by Skordaris [36] to look at how temperature variations affect the results of the inclined impact test. The test specimens were similar to [25], with the same coating thickness of 5 µm, and the same inclined indenter setup. The critical impact force for the coating to survive one million cycles at temperatures ranging from about 0°C to 400°C was calculated, and the results showed that critical impact force decreases as temperature increases. The experimental results were used to validate a three-dimensional FEM model previously developed by the author [37].

The results of the experiment and FEM model show the prediction of the critical shear stress is affected by the operational conditions, as well as the manufacturing process, due to thermal and residual stresses.

An important factor in the FEM model is the type of contact element used to model the interface [36]. The contact element is modelled using springs of variable stiffness with normal and tangential components,which take into account any residual stresses that may exist from the deposition process [37]. In the indenter impact area, delamination is implemented using a failure criterion nullifying the spring, signifying there is no longer any surface tension in the coating at that point. The areas of the coating that are not impacted by the indenter are assumed to have constant adhesion.

2.5 Conclusion

In summary, while fatigue data has an inherent amount of variability [38], the literature shows many factors will affect the fatigue life of a given test specimen, including the imparted impact energy [32], [33], the grain size [24], and residual stresses [24], [26].

Chapter 3

Experiments

As discussed in the Introduction, the primary goal for this research was to investigate the performance of nanocrystalline nNiCo and nCo coatings under combined impact and fatigue loading. Therefore, the main requirements for the experimental setup included:

1. An adequate number of both coated and uncoated specimens of the same geometry (the uncoated specimens were used to determine the substrate material properties);
2. A method of applying impact damage to a test specimen at various energies;
3. A method of measuring the projectile velocity during the impact test, in order to calculate the applied impact energy;
4. A method of performing a fatigue test while capturing stress and strain data; and
5. A method of analysing the fracture surface.

3.1 Specimens

The geometry of the uncoated specimens and the substrates of the coated specimens is shown in Figure 3.1. The nominal overall length was 9.30 in, or 236.22 mm, with a thickness of 0.125 in, or 3.175 mm. The gauge section had a nominal length 1.570 in, or 39.878 mm, and a width of 13.970 mm. The geometry and preparation conform to ASTM E466 [39], which covers room temperature uniaxial force controlled fatigue tests where the specimen remains primarily in the elastic regime. Aluminum 6061-T6 was chosen as the substrate for these experiments, as this alloy is inexpensive, readily available, and easy to machine. The Al 7255 used in the previous UTIAS experiments was difficult to obtain and machine and exhibited poor bonding to the nanometal coating in some instances [8]. The substrates were manufactured using a water-jet cutter at PWC and then stress-relieved at 300°F for one

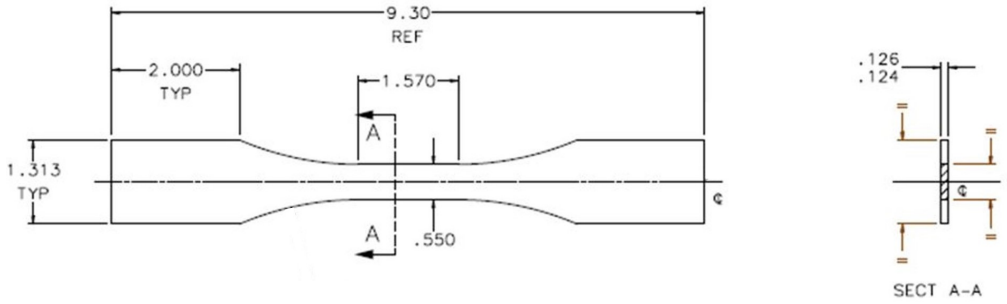

Figure 3.1: Fatigue test specimen substrate, dimensions in inches.

hour. Additional uncoated specimens were made at the University of Toronto's Mechanical and Industrial Engineering (MIE) Machine Shop using the same process.

The substrates produced at PWC were given to Integran Technologies Inc. (Integran) for the electrodeposition coating process. Two different nanocrystalline coatings were selected by PWC for this project: nNiCo, known as Nanovate N1210, and nCo, known as Nanovate R3310. For each coating type, substrates were coated with two nominal thicknesses: 100 μm and 250 μm.

Table 3.1 shows the as-measured dimensions of each group of the 34 specimens that were tested. Before testing, specimens were sanded to a mirror-like finish to remove nodules on the surface that affected the accuracy of the measurements. The specimens were progressively polished using sandpaper (150, 400, 800, 1000 and 1500 grit) and finally with either 3000 grit sandpaper or 0.05 μm diamond polish. The coated specimens had a nominal substrate cross-sectional area of 44.355 mm^2 based on the dimensions provided in Figure 3.1. This was used to calculate the total coating area.

Table 3.1: Fatigue Results for Uncoated and Coated 100 μm nNiCo Flat Specimens

Specimen ID	Width [mm]	Thickness [mm]	Coating Thickness [μm]	Edge Coating Thickness [μm]	Coating Area [μm^2]
Uncoated No Impact					
P3	14.14	3.16	N/A	N/A	N/A
P4	14.13	3.17	N/A	N/A	N/A
P6	14.15	3.17	N/A	N/A	N/A
P7	14.22	3.14	N/A	N/A	N/A
P8	14.20	3.15	N/A	N/A	N/A
P9	14.23	3.14	N/A	N/A	N/A

Table 3.1: Fatigue Results for Uncoated and Coated 100 µm nNiCo Flat Specimens

Specimen ID	Width [mm]	Thickness [mm]	Coating Thickness [µm]	Edge Coating Thickness [µm]	Coating Area [µm^2]
P10	14.19	3.14	N/A	N/A	N/A
P11	14.24	3.20	N/A	N/A	N/A
P12	14.25	3.14	N/A	N/A	N/A
P13	14.18	3.18	N/A	N/A	N/A
P14	14.20	3.17	N/A	N/A	N/A
P15	14.15	3.17	N/A	N/A	N/A
P17	14.12	3.18	N/A	N/A	N/A
P18	14.08	3.18	N/A	N/A	N/A
100 µm nNiCo Coated					
H1	14.45	3.44	132.5	283.3	5.342
H2	14.53	3.52	174.2	283.3	6.863
H3	14.34	3.35	89.2	181.7	3.698
H4	14.47	3.51	169.2	248.3	6.471
H5	14.47	3.48	160.8	251.7	6.061
H10	14.29	3.36	94.2	158.3	3.696
H11	14.45	3.50	164.2	240.0	6.268
H13	14.47	3.58	203.8	251.7	7.496
H14	14.38	3.43	129.2	206.7	5.028
H15	14.52	3.59	208.8	275.0	7.699
H16	14.30	3.48	154.2	166.7	5.468
250 µm nNiCo					
F1	14.93	3.85	339.2	478.3	13.16
F2	14.93	3.85	337.5	481.7	13.14
F3	15.06	3.83	325.8	546.7	13.29
F4	14.84	3.86	342.5	436.7	12.94
F5	14.86	3.84	332.5	443.6	12.69
F6	14.91	3.88	350.8	471.7	13.46
F10	14.84	3.77	297.5	433.3	11.58
F11	14.80	3.74	280.8	413.7	10.94

Table 3.1: Fatigue Results for Uncoated and Coated 100 µm nNiCo Flat Specimens

Specimen ID	Width [mm]	Thickness [mm]	Coating Thickness [µm]	Edge Coating Thickness [µm]	Coating Area [μm^2]
F12	14.91	3.82	320.8	471.7	12.56
F13	14.82	3.78	300.8	425.0	11.62
F15	14.84	3.74	280.8	433.3	11.08
100 µm nCo Coated					
G11	14.36	3.47	147.5	195.0	5.997
G15	14.40	3.50	160.8	215.0	5.474
250 µm nCo Coated					
E9	15.01	3.81	318.8	520.0	12.87

3.2 Impact Tests

3.2.1 Gas Gun Design

The gas gun was designed to subject a stationary test specimen to impact damage via a spherical projectile [10], and has been used in previous impact experiments done at UTIAS [9]. Activated using a solenoid valve, high pressure gas (in this case, air) forces the projectile down a low pressure channel, or barrel. The design parameters include the projectile diameter, the channel diameter, the gas reservoir volume, the gun barrel length, and initial gas pressure. The initial constraints were a projectile velocity of less than the speed of sound (about 343 m/s), and a projectile diameter should be smaller than the width of the specimen gauge section (13.97 mm). As suggested by Bouzakis et al. [25], a small variation in impact velocity might greatly affect the amount of impact damage. Therefore, the test plan included a range of velocities to look at the sensitivity of the projectile velocity on the performance of the coating, up to a maximum of 250 m/s. The previous impact experiment setup was sized for a 46 g projectile, which had a diameter of 22.35 mm. This was too large for the test specimens, so a projectile diameter of 3/8 in (or 9.525 mm) was selected. The necessary barrel length was calculated at various input pressures using on the projectile launcher FORTRAN code described in [10], using a gas reservoir volume of 813.5 cm^3, and an inner barrel diameter of 9.6 mm. A sketch of the cross-section of the pressure reservoir showing its dimensions and details of the bleed valve, pressure gauge, and air inlet and outlet is shown in Figure 3.2. This dimensions shown in this sketch were used to calculate a precise estimate of the reservoir volume. The plot of output barrel lengths versus projectile length from the FORTRAN code

is shown in Figure 3.3.

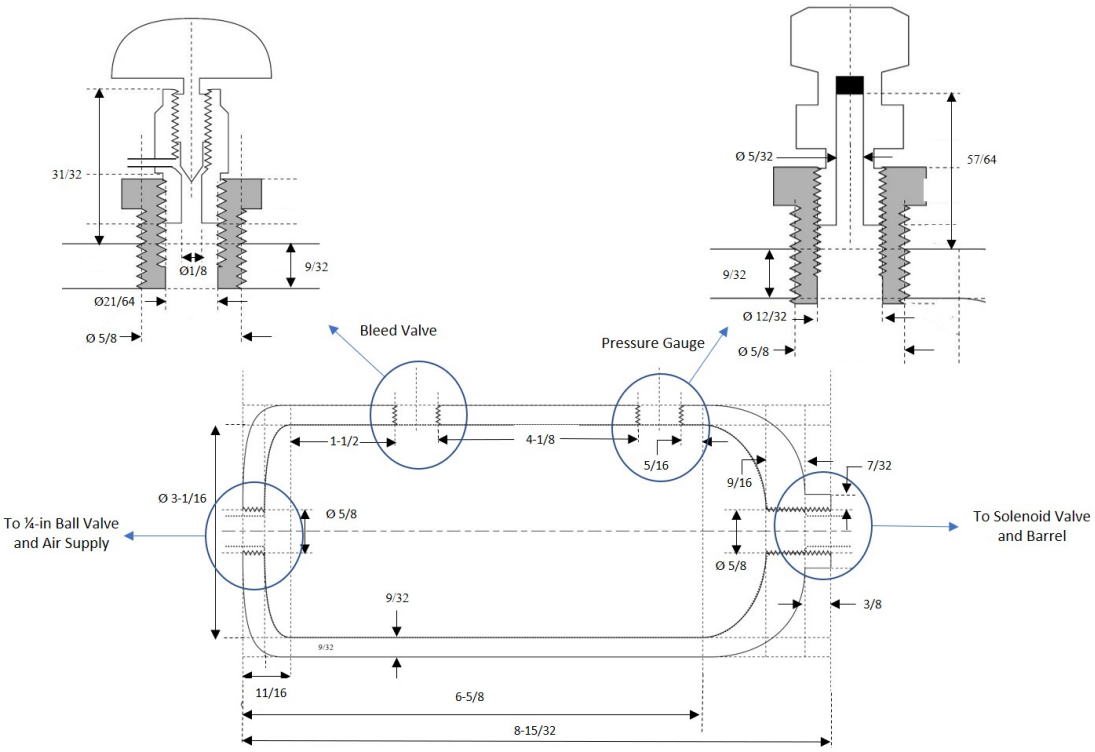

Figure 3.2: Gas gun high pressure reservoir schematic cross section. Dimensions in inches. Adapted from a drawing by Gottlieb [10].

Balancing lab space requirements and manufacturing costs with the predicted projectile speeds at a reasonable range of pressures, a barrel length of 2 metres was selected. As recommended in by Gottlieb [10], the inner diameter of the barrel was sized to be slightly larger than the projectile, to avoid an interference fit and to allow some airflow around the projectile. The inner diameter was specified as 0.5% larger than the projectile size, or 9.573 mm. However, the ball bearings did not properly fit once the barrel was made, so 11/32 in (8.732 mm) steel projectiles were used, which have a nominal density of 7850 kg/m^3.

The UTIAS compressed air has a maximum gauge pressure of 100 psi, or 6.8 atm. Velocities higher than about 130 m/s need either compressed air tanks or by using a compressor in conjunction with the house air. The high pressure air was released into the barrel via a 3/8 inch Graznow 21HN3KY110 normally closed solenoid valve.

3.2.2 Instrumentation

Pressure was measured using an Omega PX482A-100GI pressure gauge, which was connected to LabView via a NI 9219 current module and CDAQ-9171 chassis, and powered using a Sopudar SPD-120W power supply. The optical gates and data acquisition were sized to

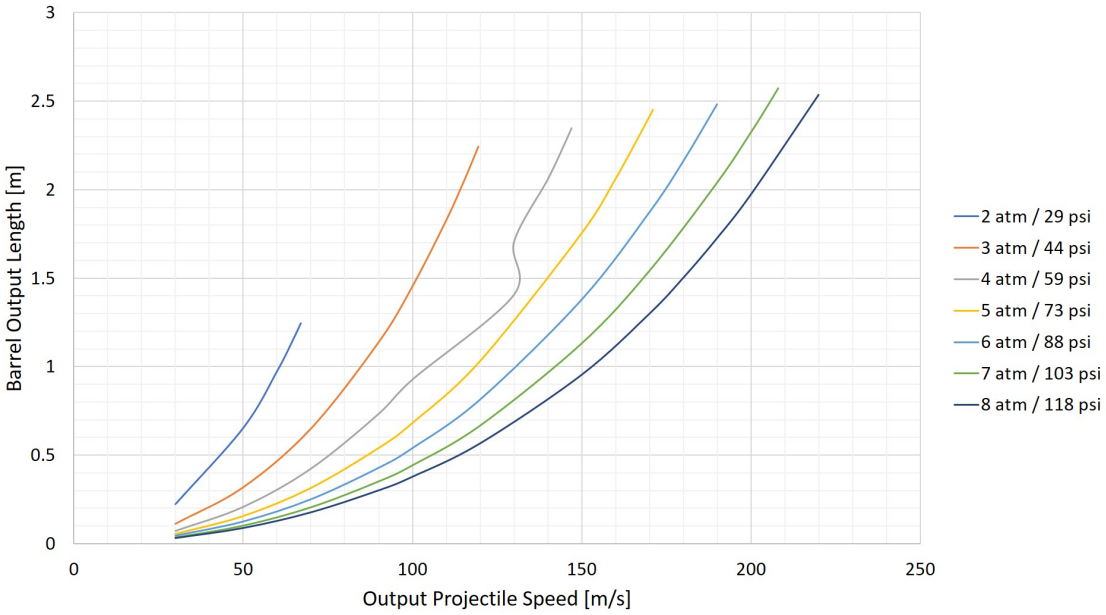

Figure 3.3: Gas gun code output projectile speed versus barrel length at various input pressures.

capture effectively a maximum velocity of 250 m/s. The velocity was calculated by taking the time difference between when each laser is broken by the projectile (corresponding to a voltage drop), and dividing by the distance between the diodes. The acceptable velocity error was on the order of 1%, so the sampling rate and rise times of the laser diodes and the data acquisition system were selected accordingly.

The optical gates consisted of two Delta Photonics CPS635 Laser Diode Modules, each paired with a PDA10A2 Si Fixed Gain Detector. The detector has a rise time of 2.3 ns with a bandwidth of 150 MHz. The mounting holes in the gun barrel collar were 5.00 in, or 127 mm, apart. The voltage drop was captured with a Tektronics TBS1064 60 MHz oscilloscope with a sampling rate of 1 gigasamples per second (Gs/s) and a display memory of 2500 points.

If the projectile is detected after it almost fully passes the first diode, and immediately upon reaching the second, this reduces the effect distance between the detectors to 125.7 mm, or 1.3 mm less than the nominal. The amount of time the projectile takes to travel 1.3 mm at the maximum speed of 300 m/s is 4.3 x 10^{-6} s, and is taken as the rise time. A common rule of thumb for relating bandwidth (BW) to rise time (RT) is given in [40]:

$$BW = \frac{0.35}{RT}. \tag{3.1}$$

The oscilloscope manufacturer recommends an instrument have about five times more bandwidth than the output of Equation 3.1 The necessary bandwidth is therefore 405 kHz, which is much less than the bandwidth of the selected oscilloscope. The opposite case, where

the effective distance between the detectors is increased to 128.3 mm has a similar result.

3.2.3 Impact Test Setup

In order to isolate the effect of impact on the coating surface from damage from global bending, the specimen were fully supported from the back. The specimen holder was mounted in a wooden 2 ft x 2 ft x 3 ft catch chamber. To prevent the projectile ricochet from injuring people or damaging equipment, the gun barrel end was placed through a 6 mm polycarbonate shield attached to the front of the catch chamber. A sketch showing the test setup design is shown in Figure 3.4.

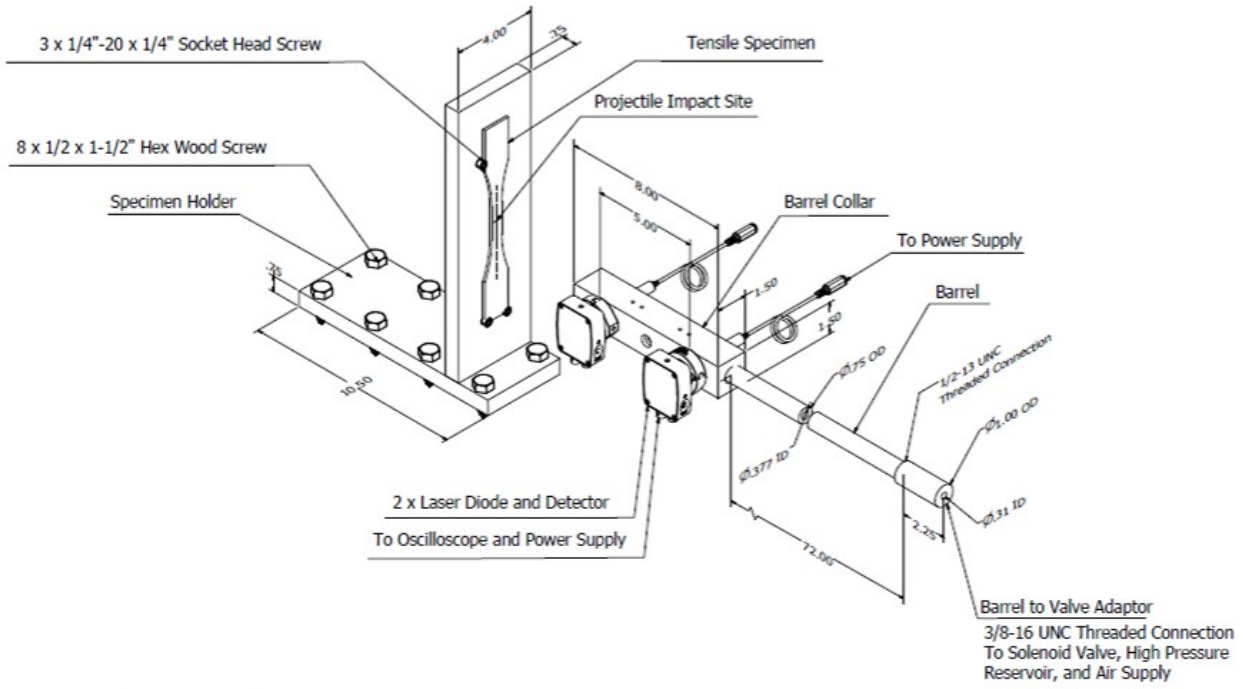

Figure 3.4: Sketch showing the gun specimen holder, gun barrel, and laser diodes and detectors.

3.2.4 Velocity and Impact Energy Calculation

The gas gun was tested without any test specimens to calibrate the pressure in the reservoir with the measured output current of the gauge, and to calibrate the pressure with the measured velocity of the projectile. Figure 3.5 shows the measured output velocity and calculated impact energy versus the measured initial pressure. An example of the oscilloscope trace during a test with a velocity of 84 m/s is shown in Figure 3.6.

3.2.5 Impact Test Procedure

Once the impact test setup was complete, the following procedure was followed for each impact test:

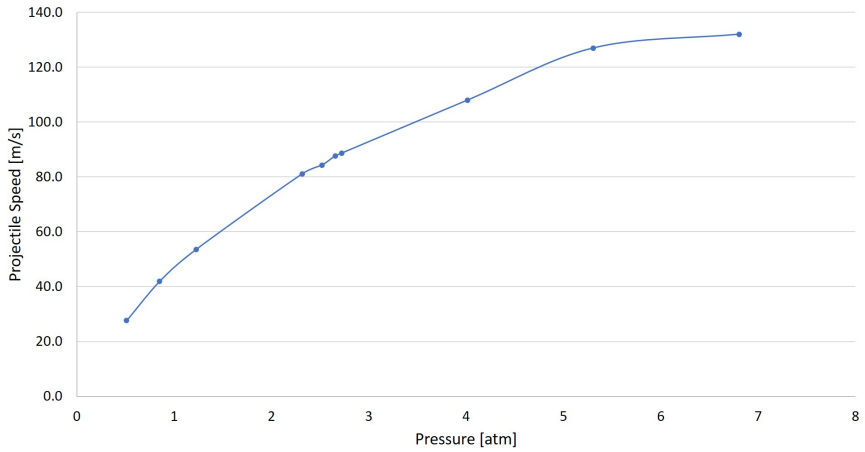

Figure 3.5: Experimental results of projectile speed and impact energy versus reservoir pressure.

1. Load the projectile into the barrel by allowing it to roll down the length toward the pressure vessel, ensuring it does not get stuck along the way.
2. Place the specimen in the specimen holder. Ensure it is placed correctly using the alignment screws and the scope laser.
3. Connect the high pressure reservoir to the air supply via a quick connect hose. Using LabView to record the pressure data, bring the reservoir to the desired initial pressure using the house air supply.
4. Ensure the laser diode detectors are being read correctly by the oscilloscope. Set the seconds per division appropriately for the anticipated speed. Set the trigger to edge type at an appropriate voltage so that the data is recorded once the voltage drop is detected on the first laser diode as the projectile passes. Set the oscilloscope to record a single event.
5. With correct ear and eye protection, while standing in the designated safety zone, energize the solenoid valve to launch the projectile.
6. Extract the oscilloscope data to calculate the speed and kinetic energy of the projectile, and save the pressure data from LabView.
7. Measure the depth of the impact indentation using a dial gauge.

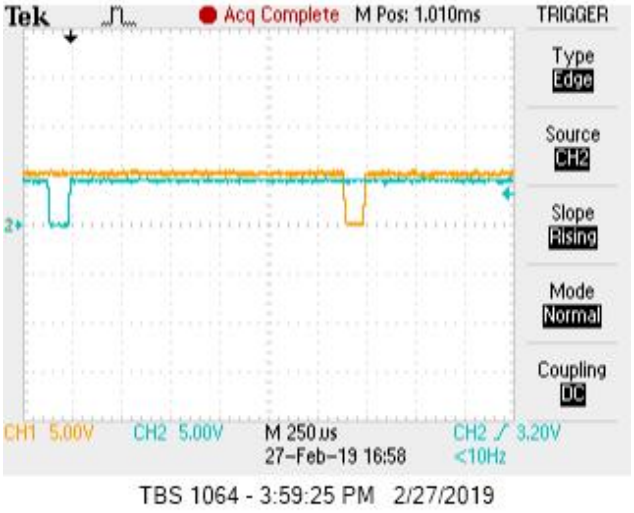

Figure 3.6: Example of oscilloscope trace of a projectile with a speed of 84 m/s, showing the velocity drop of each diode as the projectile passes.

3.3 Fatigue Test

The test procedure developed for the fatigue experiments is based on ASTM E466 [39]. Applied force, strain (via three methods), load frame cross-head displacement were collected during each test. The test setup is shown in Figure 3.7.

3.3.1 Equipment and Data Collection

The testing was done using an MTS 880 model 380.10 uniaxial load frame. This machine has a 100 kN load capacity, capable of cross-head displacement of 50 m/s. Hydraulic wedge grips (model 647.10) were used to accommodate the flat test specimens.

Three methods of strain measurement were used, including a strain gauge, a non-contact laser extensometer, and digital image correlation. One strain gauge (Tokyo Sokki FLA-5-11-3L) was applied axially using cyanoacrylate glue near the centreline of the specimen gauge section. The LE-05 laser extensometer (Electronic Instruments Research) requires two pieces of retro-reflective tape applied to the short edge of the gauge section to calculate the relative change in distance between the tapes. This relative change in distance represents the elongation of the specimen and thus a strain.

A black and white speckle pattern was applied to one face of the specimen in the gauge section. As recommend by [40] the flexible white base paint was chosen so it would continue to adhere to the surface as the specimen was elongated during the test. Photos were taken using a Point Grey GRAS-50S5M-C 5.0 mega-pixel monochromatic digital camera with 2448

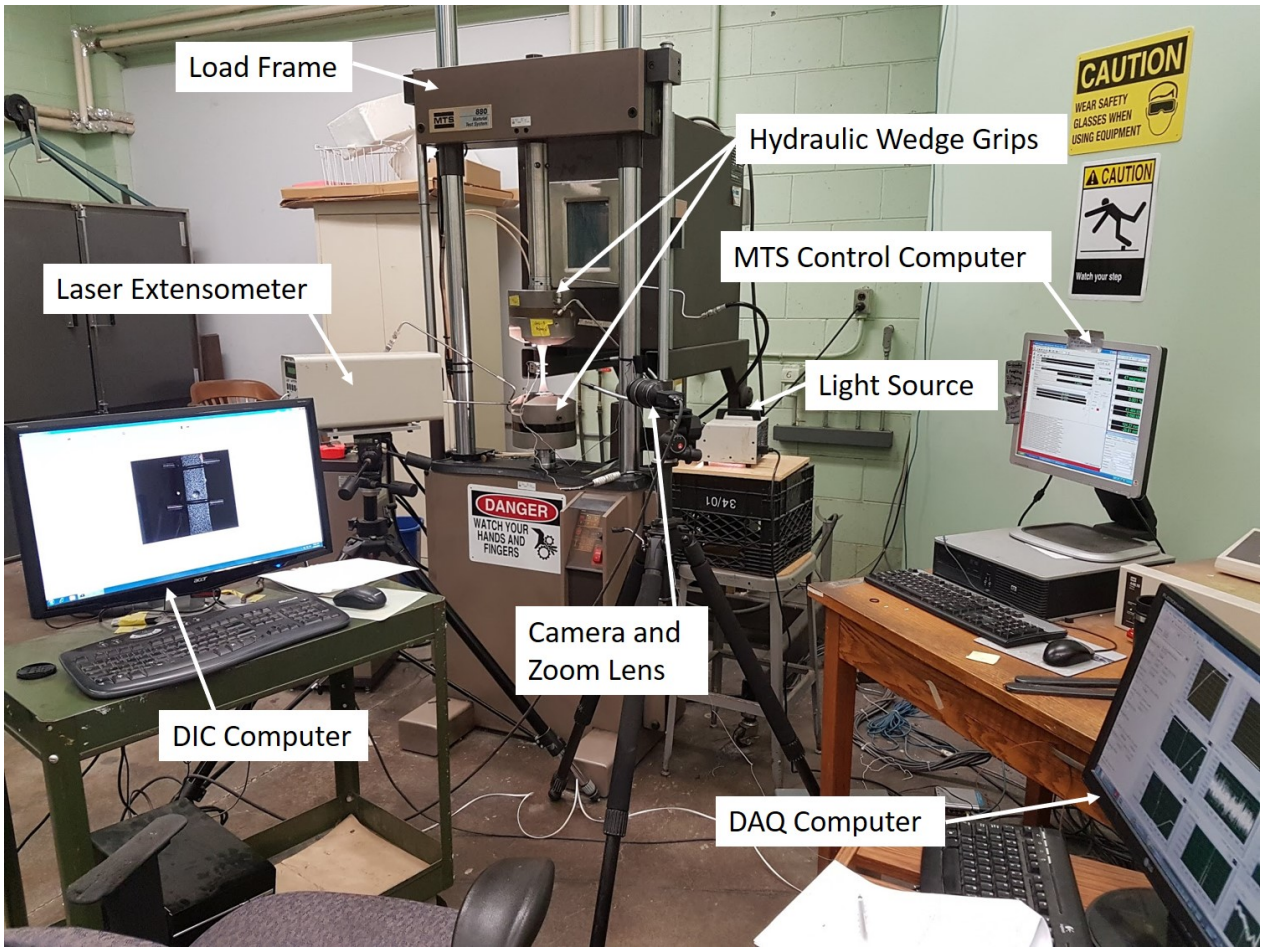

Figure 3.7: Typical fatigue test setup.

x 2048 resolution. This camera has square pixels which is preferred as it simplifies the DIC analysis [40]. A Tamron DiSP 90 mm lens was attached using an F to C-mount adapter. The photos were captured using the VIC-2D software by Correlated Solutions, installed on a second PC. Adequate lighting was provided by a Cole-Parmer FOI-150 fibre optic illuminator.

The strain and MTS data were collected using a National Instruments NI SC-2345 data acquisition (DAQ) carrier. The laser extensometer, MTS force and MTS displacement data were collected using a SCC-FT01 feed-through module, and the strain gauge data were collected using a SCC-SG01 strain gauge module. The MTS machine and fatigue tests are controlled through MT Station Manager and MTS Model 793.10 Multipurpose Testware software. The DAQ data is recorded through National Instruments LabView software.

3.3.2 Fatigue Test Procedure

The following is the test procedure used at UTIAS to perform the coated specimen load-controlled fatigue tests:

1. After the axial strain gauge is glued on and allowed to dry, mount the specimen into MTS 880 machine. Use alignment guides attached to the grips and a level to ensure the specimen is straight.

2. Ensure all instrumentation is correctly wired into the DAQ, and apply the retro-reflective tape. Zero the force, displacement and strain values.

3. Apply displacement-controlled loading at a rate of 0.5 mm/min until the measured strain is equivalent to 0.5%. Unload, then repeat three times. Confirm the obtained force-strain curve is linear (implying only elastic deformation). For the coated specimens, calculate the coating modulus as described in Section 3.3.3, Equation 3.6.

4. Apply displacement-controlled loading at a rate of 0.5 mm/min until the measured strain is equivalent to 0.6%. From experimental data for the substrate aluminum, this value corresponds with 291 MPa. The force which corresponds to a specimen strain of 0.6% is set as the maximum force for the fatigue test.

5. Unload the specimen at the same strain rate. The minimum force is found at the minimum strain value on the unloading line. The minimum strain value is obtained from equations 3.7 through 3.9 in section 3.3.4.

6. Program the fatigue test script in the MTS MultiPurpose TestWare software. The script uses the maximum and minimum forces determined in steps 4 and 5. Set the test rate. Initial tests were done at 1.5 Hz but later tests were done at 10 Hz. Photos for DIC analysis and strain data collection to determine hysteresis loops can only be done during "slow" cycles (at a rate of 0.1 Hz) so the selection of cycle groups is made based on how much resolution is desired. Typically, slow cycles were programmed after every 1000 to 5000 cycles in the early stages of the test, and reduced to every 250 or 500 cycles near the anticipated end of the test to ensure strain data near the fracture point is captured with as much resolution as possible. This is to balance data needed for the DIC analysis against the time taken to complete the test.

7. Run the fatigue test until failure.

8. Remove the fractured specimen halves from the machine, with care not to damage the fracture surfaces.

9. Perform post-fracture SEM analysis on specimens deemed to be of interest.

3.3.3 Calculation of the Coating Elastic Modulus

The calculation of the elastic modulus of the coating assumes:

1. Coating and substrate undergo only elastic deformation at strains less than 0.3%.

2. The substrate elastic modulus is known.

3. The strain in the coating ϵ_C is equal to the strain in the substrate ϵ_S:

$$\epsilon_C = \epsilon_S. \tag{3.2}$$

4. The total force F_T applied to the specimen is the sum of the force in the coating F_C and the force in the substrate F_S:

$$F_T = F_C + F_S. \tag{3.3}$$

The modulus was calculated based on a least squares fit of the unloading data between strains of 0.1% to 0.3%. The change in force in the substrate over the the elastic range from 0.1 to 0.3 % strain, ΔF_{Se} is:

$$\Delta F_{Se} = \Delta\sigma_{Se} A_S = \Delta\epsilon_{Se} E_S A_S, \tag{3.4}$$

where $\Delta\sigma_{Se}$ is the change in stress in the substrate over the elastic range, A_S is the cross-sectional area of the substrate, $\Delta\epsilon_{Se}$ is the change in strain in the substrate, and E_S is the elastic modulus of the substrate. The change in force in the coating over the elastic range from 0.1 to 0.3 % strain, ΔF_{Ce} is:

$$\Delta F_{Ce} = \Delta F_{Te} - \Delta F_{Se}, \tag{3.5}$$

where ΔF_{Te} is the change in total force applied to the specimen over the elastic range. The coating modulus E_C can be calculated by re-arranging Equation 3.4 as:

$$E_C = \frac{\Delta\sigma_{Ce}}{\Delta\epsilon_{Ce}} = \frac{\Delta F_{Ce} A_C}{\Delta\epsilon_{Ce}} \tag{3.6}$$

where $\Delta\sigma_{Ce}$ is the change in stress in the coating over the elastic range, $\Delta\epsilon_{Ce}$ is the change in strain in the coating, ΔF_{Ce} is the change in force in the coating, calculated in Equation 3.5, and A_C is the cross-sectional area of the coating.

3.3.4 Calculation of the Minimum Applied Force

The calculation of the maximum and minimum applied forces assume that the aluminum substrate stress-strain behaviour is known. The maximum strain ϵ_{max} applied to the specimen was selected to correspond to a maximum substrate stress σ_{max_s} of 291 MPa. The strain ϵ_{max} is thus 0.6%. The force value which corresponded to ϵ_{max_s} on the specimen force-strain curve was taken as the maximum force F_{max}, as shown in Figure 3.8.

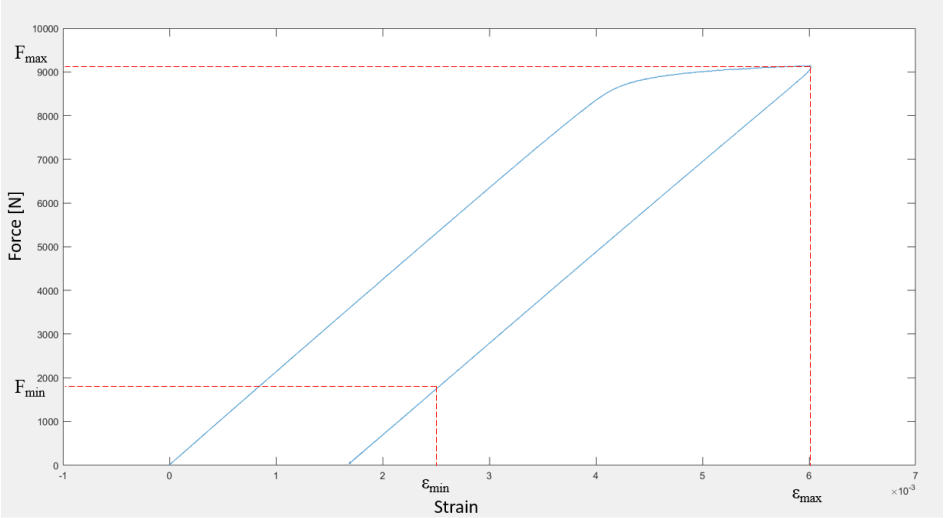

Figure 3.8: Typical specimen force-strain curve showing minimum and maximum force and strain.

The desired substrate R value is 0.01, which gives a targeted minimum stress, σ_{min_s} of:

$$\sigma_{min_s} = R\sigma_{max_s} = 2.91\,\text{MPa} \tag{3.7}$$

The minimum force that will be applied to the specimen, F_{min}, assumes elastic unloading occurs in the substrate. It is calculated by first determining the change in strain in the substrate $\Delta\epsilon_s$, caused by the reduction in load:

$$\Delta\epsilon_s = \frac{\sigma_{max_s} - \sigma_{min_s}}{E_s} \tag{3.8}$$

The minimum strain in the substrate is thus:

$$\epsilon_{min_s} = \epsilon_{max_s} - \Delta\epsilon_s \tag{3.9}$$

Since the strain in the substrate and coating are equal (Equation 3.2), the minimum applied force F_{min} can be read directly from the force-strain curve curve at the strain ϵ_{min} per Figure 3.8.

Chapter 4

Results and Analysis

4.1 Experimental Results

The results of the impact and fatigue test results are shown in Table 4.1. The coating area and thickness columns are repeated from Table 3.1 in Chapter 3. The impact velocity and energy were calculated per Section 3.2.5, and the coating modulus E_C per Section 3.3.3. Figure 4.1 shows a summary plot of fatigue life versus impact energy for all test specimens. The most immediate observation is that the uncoated specimens had much higher fatigue lives than the nano coated specimens, even after the impact tests. Note the uncoated specimens, with the exception of P14 and P18, had a targeted maximum stress in the substrate, σ_{Smax}, of 310 MPa. All remaining specimens were tested to σ_{Smax} of 291 MPa.

Table 4.1: Fatigue Results for Uncoated and Coated Flat Specimens

Specimen ID	Coating Area [μm^2]	Coating Thickness [μm]	Impact Velocity [m/s]	Impact Energy [J]	Indentation Depth [mm]	Coating Modulus E_C [GPa]	Fatigue Life [cycles]
Uncoated No Impact							
P3	-	-	-	-	-	-	21,934
P4	-	-	-	-	-	-	27,020
P6	-	-	-	-	-	-	25,878
P8	-	-	84.3	9.6	0.741	-	19,020
P9	-	-	64.7	5.7	0.542	-	25,041
P10	-	-	41.5	2.4	0.330	-	18,231
P11	-	-	109.7	16.4	0.944	-	13,200
P12	-	-	123.3	20.8	1.067	-	15,521
P13	-	-	-	-	-	-	19,120

Table 4.1: Fatigue Results for Uncoated and Coated Flat Specimens

Specimen ID	Coating Area [μm^2]	Coating Thickness [μm]	Impact Velocity [m/s]	Impact Energy [J]	Indentation Depth [mm]	Coating Modulus E_C [GPa]	Fatigue Life [cycles]
P14*	-	-	-	-	-	-	39,454
P15	-	-	-	-	-	-	22,086
P17	-	-	-	-	-	-	26,210
P18*	-	-	-	-	-	-	68,800
100 μm nNiCo Coated							
H1	5.342	132.5	-	0.0	-	151	7,836
H2	6.863	174.2	-	0.0	-	149	3,920
H3	3.698	89.7	110.1	16.6	0.720	311	2,776
H4	6.471	169.2	63.3	5.5	0.381	156	8,579
H5	6.061	154.2	120.6	19.9	1.012	183	3,570
H10	3.696	94.2	93.2	11.8	0.677	279	7,237
H11	6.268	164.2	135.5	25.0	1.084	184	6,752
H12	6.192	172.5	93.9	12.1	0.643	188	5,633
H13	7.496	203.7	84.2	9.7	0.639	132	5,673
H14	5.028	129.2	70.7	6.9	0.601	202	10,754
H15	7.699	205	41.8	2.4	0.271	124	9,696
H16	5.468	154.2	96.9	12.8	0.728	153	6,118
250 μm nNiCo							
F1	13.16	339.2	-	0.0	-	177	5,197
F2	13.14	337.5	-	0.0	-	175	4,870
F3	13.29	325.8	43.7	2.6	0.254	194	6,340
F4	12.94	342.5	63.2	5.5	0.406	196	3,808
F5	12.69	332.5	83.3	9.7	0.610	192	4,173
F6	13.46	350.8	98.4	13.2	0.720	202	1,507
F7	13.57	347.5	121.2	20.1	0.940	184	2,984
F10	11.58	297.5	106.5	15.5	0.847	178	6,188
F11	10.94	280.8	134.2	24.7	0.940	202	3,215
F12	12.56	320.8	94.0	12.1	0.715	190	7,394
F13	11.62	300.8	89.7	11.0	0.631	224	3,540
F15	11.08	280.8	70.6	6.8	0.457	182	9,278

Table 4.1: Fatigue Results for Uncoated and Coated Flat Specimens

Specimen ID	Coating Area [μm^2]	Coating Thickness [μm]	Impact Velocity [m/s]	Impact Energy [J]	Indentation Depth [mm]	Coating Modulus E_C [GPa]	Fatigue Life [cycles]
100 μm nCo Coated							
G11	5.997	147.5	-	-	-	140	1,731
G15	5.474	160.8	-	-	-	124	5,41
250 μm nCo Coated							
E9	12.87	318.7	15.01	-	-	144	1
*specimen was tested at σ_{Smax} of 310 MPa							

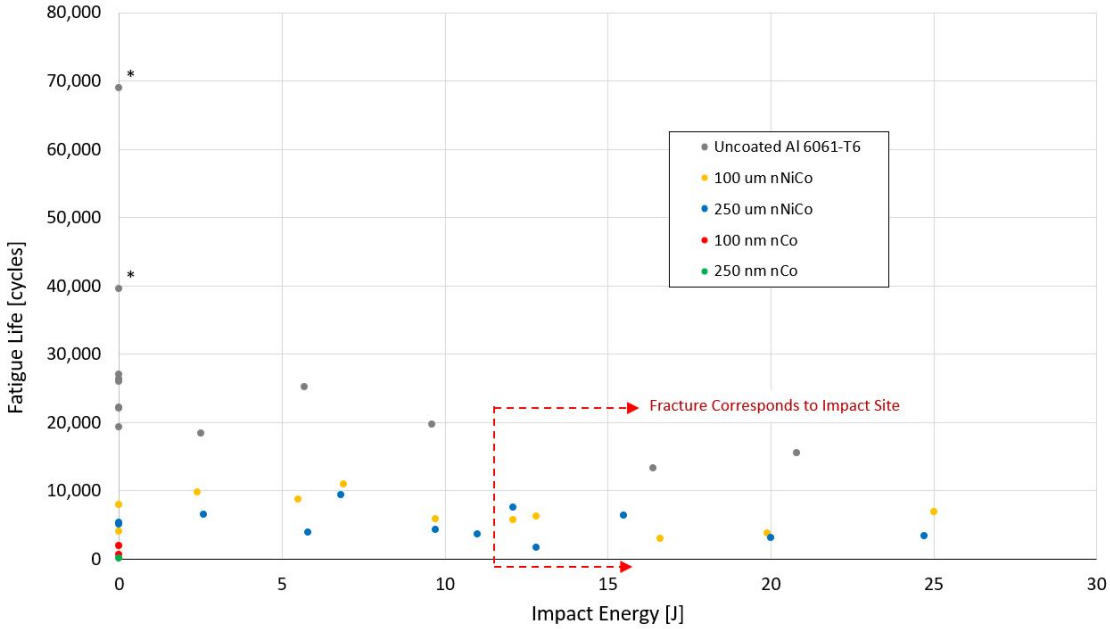

Figure 4.1: Fatigue life vs. impact energy for all test specimens. All uncoated specimens were tested at σ_{Smax} of 310 MPa, with the exception of those indicated by the asterix which were tested at 291 MPa. All coated specimens were tested at σ_{Smax} of 291 MPa. The arrows indicate the specimens where the fracture point corresponds to the site of the projectile impact.

Figure 4.2 shows the fatigue life versus impact energy for the nano coated specimens alone, and illustrates that the nCo specimens performed poorly relative to the nNiCo specimens. Due to the low fatigue lives of the three nCo specimens that had not been subjected to impact, it was decided to focus the impact testing effort on the nNiCo coating. The plot also shows that the thinner 100 μm specimens performed slightly better than the 250 μm specimens. One exception is H3, which had a shorter fatigue life than F10. However, it

was noted after the test that the projectile used on H3 had a sharp edge, causing a stress concentration in the impact indentation. Figures 4.1 and 4.2 also show that in all cases, impact energies above 11 J cause failure at the site of the projectile impact, while specimens with impact energies lower than 11 J broke at one of the corners in the gauge section.

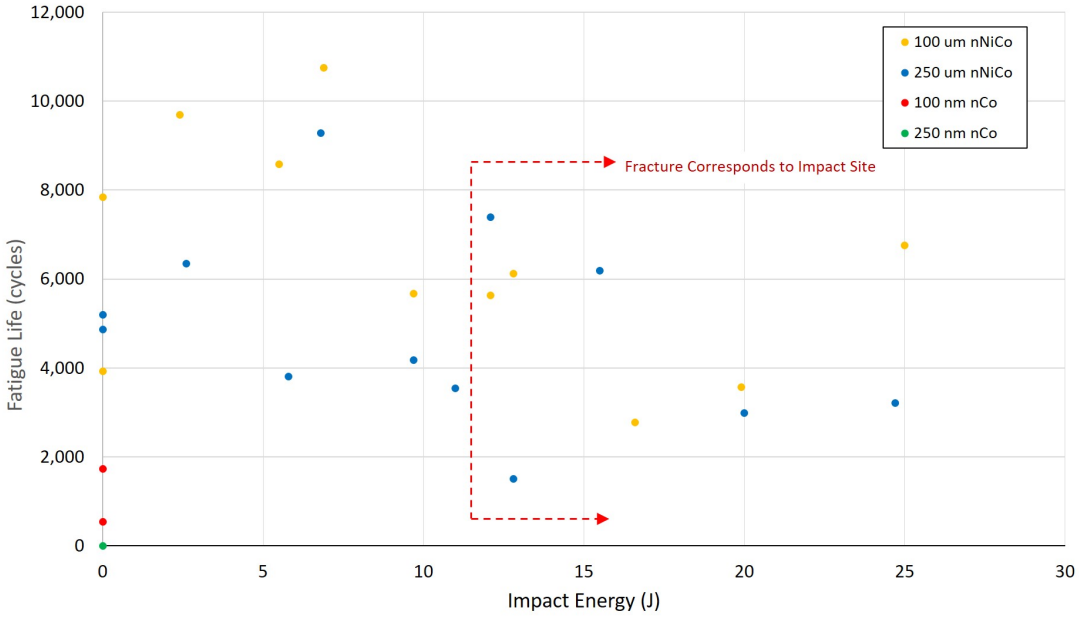

Figure 4.2: Fatigue life versus impact energy for all nano coated specimens, which were tested at σ_{Smax} of 291 MPa. The arrows indicate the specimens where the fracture point corresponds to the site of the projectile impact.

4.2 Discussion

In general, the fatigue life is not strongly correlated to impact energy or projectile impact depth, contrary to what was initially hypothesised. An analysis of the experimental data show it is the maximum stress in the coating that most strongly determines the fatigue life, not that in the substrate as was assumed. There is evidence that the stresses in both the coating and substrate include residual stresses that existed prior to testing, likely induced during the electroplating process in addition to stresses from the applied load during the test. These findings were established by first considering the results in terms of the average fatigue life of the non-impact specimens, the coating elastic modulus, and the indentation depth and the effect of the impact on fatigue life. Digital Image Correlation (DIC) analysis was used to investigate the strains in the coating after the impact test and during the fatigue tests, and the fracture surfaces were analysed Scanning Electron Microscopy (SEM). Finally, using methodology developed from the results of fatigue tests on cylindrical coated specimens [41], the total stress, including applied and induced stresses, were calculated and used to construct

an S-N curve for both the coating and the substrate.

4.2.1 Fatigue Life of Non-Impact Specimens

The average fatigue life for the non-impact uncoated specimens tested to σ_{Smax} of 310 MPa is 23,708 with a standard deviation of 3,123 cycles, and a range of 7,900 cycles. The average fatigue life for the two uncoated specimens tested to σ_{Smax} of 291 MPa is 54,127 with a range of 29,346 cycles. The average fatigue life for non-impact 100 µm nNiCo specimens was 5,878 with a range of 3,916 cycles. The non-impact 250 µm nNiCo specimens had a slightly lower average fatigue life of 3,027 cycles with a smaller range of 327 cycles. The average fatigue life for the 100 µm nCo was 1,257 with a range of 78 cycles. The 250 µm nCo specimen E9 failed after only one cycle.

The poor fatigue performance of the coated specimens was initially unexpected, as it was assumed that the stresses in the substrate would drive fatigue behaviour and the stronger coating would act as a protective layer. In general nano materials can have improved fatigue performance [3]. However, a refinement in grain size may lead to poor performance in low cycle fatigue, which is characterized by plastic deformation in each cycle, due to non-linear stress-strain performance during loading and unloading [42]. The target substrate stress of 291 MPa, is between the 0.2% yield point of 275 MPa and the ultimate tensile strength of 310 MPa of Al 6061-T6 [43]. The fatigue lives of specimens P14 and P18 fall close to the published S-N curve in Chapter 2 Figure 2.7.

It was initially assumed that at 0.6% strain, the coating would remain elastic while the substrate yielded. According to Integran, the nNiCo coating had a yield strength in the range of 900 to 1200 MPa. At 0.6% strain and assuming an elastic modulus of 198 GPa, the coating had a nominal coating stress σ_{cmax} of 1186 MPa, meaning that the coating could possibly yield in the fatigue tests. The reduced performance of nano materials in low cycle fatigue is one potential explanation for the results of these experiments.

4.2.2 Coating Elastic Modulus

The elastic modulus for each specimen was calculated using Equation 3.6, using the initial elastic strain data per Step 3 in Section 3.3.2 of Chapter 3. For the nNiCo specimens, the average E_C was calculated as 188 GPa, with a standard deviation of 42 GPa. For the nCo specimens, the average E_C was 137 GPa, with a standard deviation of 11 GPa. Integran provided an estimate of 197.6 GPa for the nNiCo coating, calculated from nano-indentation tests. The elastic modulus for a nano material is lower than that of a polycrystalline equivalent; for comparison, pure polycrystalline nickel and cobalt have published modulus of elasticity of 199.5 GPa and 211 GPa, respectively [43].

The coating cross-sectional area has a large effect on the calculation of the elastic modulus.

For example, an error of 1% in the total measured area will change the calculated coating modulus by about 8%. The calculated E_C values for specimens H3 and H10 in Table 4.1 are quite high, and out of the expected range. The measured coating areas for these specimens is also low compared to the average, suggesting that a measurement error might have occurred. If the measured total thickness of specimen H3, for example, is increased from 3.35 mm to 3.50 mm, the coating thickness would then be 5.80 μm^2, and the coating modulus would then be calculated as 205 GPa, a result much closer to the expected value. While the specimens were sanded to ensure more accurate measurements, the uneven surface characteristics, such as nodules, contributed to the measurement uncertainty. When specimens H3 and H10 are excluded, the standard deviation of the nNiCo coating modulus is reduced from 42 to 27. This result is closer to what was found by Giallonardo et al. [44]. In their experiment they tested eight bulk nNi and nNi-Fe specimens, each under 5 elastic loading conditions, and reported a range of 5 to 20 GPa for the elastic modulus standard deviation values.

4.2.3 Indentation Depth

A plot of the indentation depth versus impact energy is shown in Figure 4.3. The data is shown with a second order polynomial line of best fit. Note that specimen H3, with an impact energy of 16.6 J, was removed from this plot due to the sharp edges on the projectile. This plot shows that the coatings reduce the impact depth of the projectile by approximately 10% to 20% at lower impact energies. The minimum threshold energy required for the final fatigue fracture to correspond to the projectile impact site is about 12 J, which equates to an impact depth of greater than 0.65 mm. This is about 18% to 20% of the total measured specimen thickness. As the impact energy increases, the specimens with thinner coatings behave more similarly to the uncoated specimens.

Figures 4.3 shows a clear increase in deformation both to the nNiCo coating and substrate as the impact energy increases. However, Figure 4.4 shows the overall fatigue life has a weak correlation to the indentation depth, and thus to impact energy. The larger slope of the linear line of best fit indicates the uncoated specimens have a stronger correlation between indentation depth and fatigue life. This plot suggests that the existence of the coating has a detrimental effect on the fatigue life, which is more significant than any reduction in fatigue life due to impact energy. The thicker nNiCo coating protects the specimen from impact damage, in the sense that the projectile cannot travel as far through the thickness, but does not appear to improve the fatigue life overall and in fact makes a specimen more susceptible to fatigue damage (per Figure 4.2).

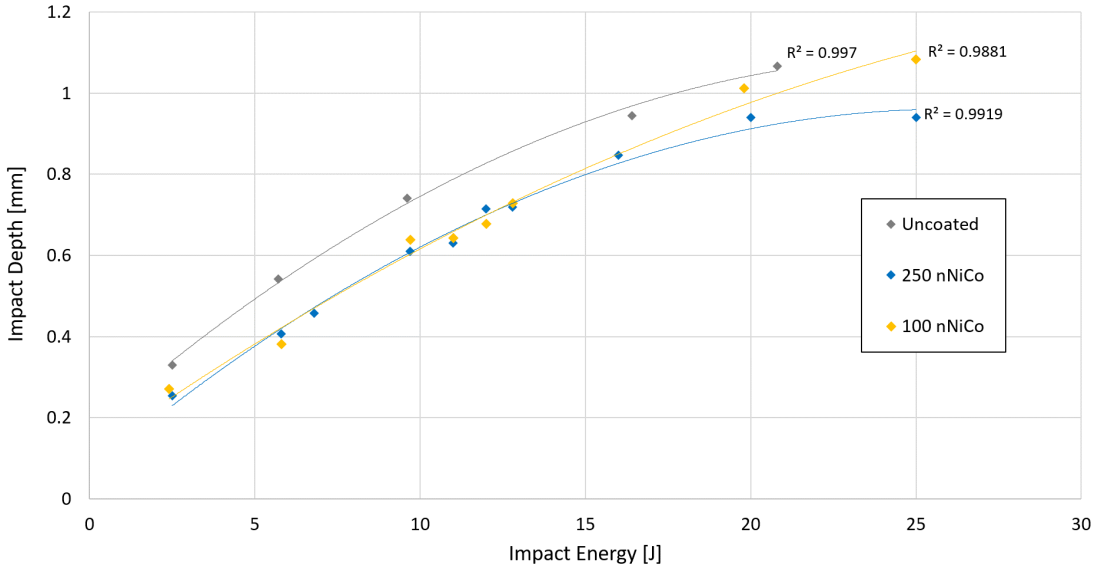

Figure 4.3: Projectile impact depth versus impact energy for uncoated and nNiCo coated specimens. The arrows indicate the specimens where the fracture point corresponds to the site of the projectile impact.

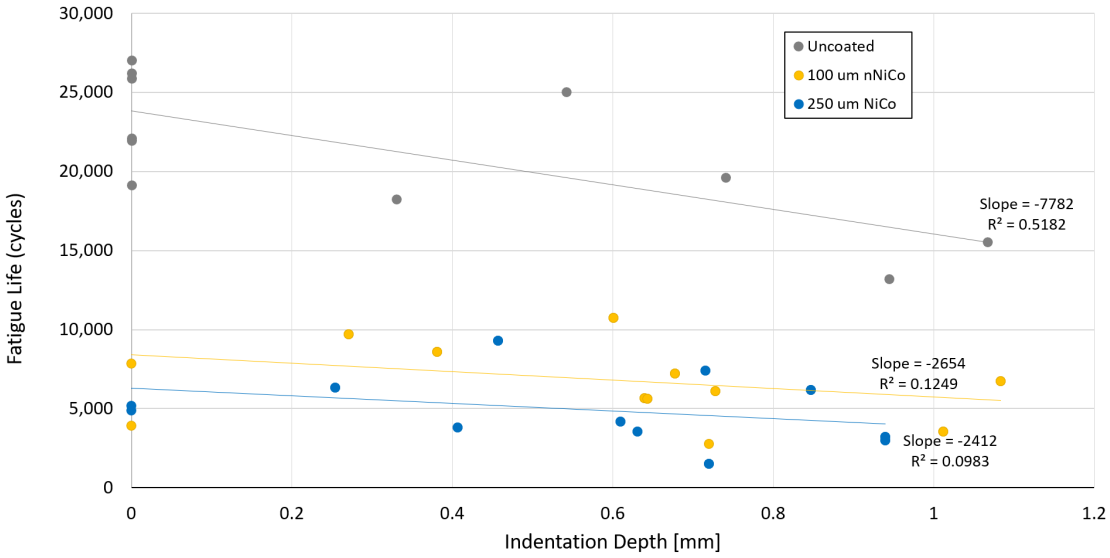

Figure 4.4: Fatigue life versus indentation depth with linear lines of best fit for uncoated and nNiCo coated specimens. Note that the uncoated specimens were tested at at σ_{Smax} of 310 MPa, and the coated nNiCo specimens were tested at at σ_{Smax} of 291 MPa.

4.2.4 DIC Analysis

Post-Impact DIC Analysis

The front and back of each impact test specimen were painted with the speckle pattern described in Section in order to estimate the strain imparted by the projectile impact, and to determine if it would correlate to the final fatigue life. The images were analysed using VIC-2D (Correlated Systems). The selected region of interest is indicated by the coloured areas. The specimen edges and area directly at the projectile impact (on both sides) were removed from the region of interest as damaged paint in these areas causes errors in the analysis. The algorithm in the software tracks a square group of pixels within a subset across the deformed images (i.e. images showing the specimen under load), and compares them to a reference image (i.e. an image showing the specimen under no load) to calculate the relative motion of each pixel. Next, the strain is calculated in the direction of the image's x-axis, ϵ_{xx}, y-axis, ϵ_{yy}, and in shear ϵ_{xy}. The step size, which is the number of points within the subset to be analysed, was 5. The smaller the step size, the more points are analysed, and the analysis time is inversely related to the square of the step size. A rule of thumb is that subset size should be larger than the size of the speckles, and the step size should be about one-quarter of the subset size. The subset size, which is the number of pixels in one length of the square, was selected as 21 and the step size was 5.

The results of the DIC analysis, presented in part in Figures 4.7 to 4.16 images show the same strain pattern at each impact energy level, with the exception of specimen F6 (Figure 4.16a): in the immediate area around of the projectile impact, there is a region of compression in the axial direction and a region of tension in the transverse direction. At all impact energy levels, the change is strain is detectable across the full width of the gauge section. The strain maps show that while the strain in the specimens at the start of the fatigue test due to the projectile impact is correlated to the impact energy, final fatigue life is not strongly correlated to the maximum tensile strain observed in each specimen. Figures 4.5 and 4.6 show the poor correlation. They also show that the maximum tensile strains are higher at the back of the impact specimen, rather than on the impact side. It was noted in SEM images of the fracture surfaces of many specimens that the failure origin point was on the support (back) side rather than the impact side. This is likely caused by the reaction force of the specimen support, and the additional tensile stresses at this point contributed to the origin of the fatigue crack.

A selection of DIC images is shown here. Figures 4.7 to 4.9 show specimens tests with an impact energy of around 20 J, P12, H5, and F7. The uncoated specimen P12 has the largest maximum strains in tension and compression, which is expected as aluminum is considerably less stiff than nNiCo. Specimen H5, which had an estimated coating thickness of about 154

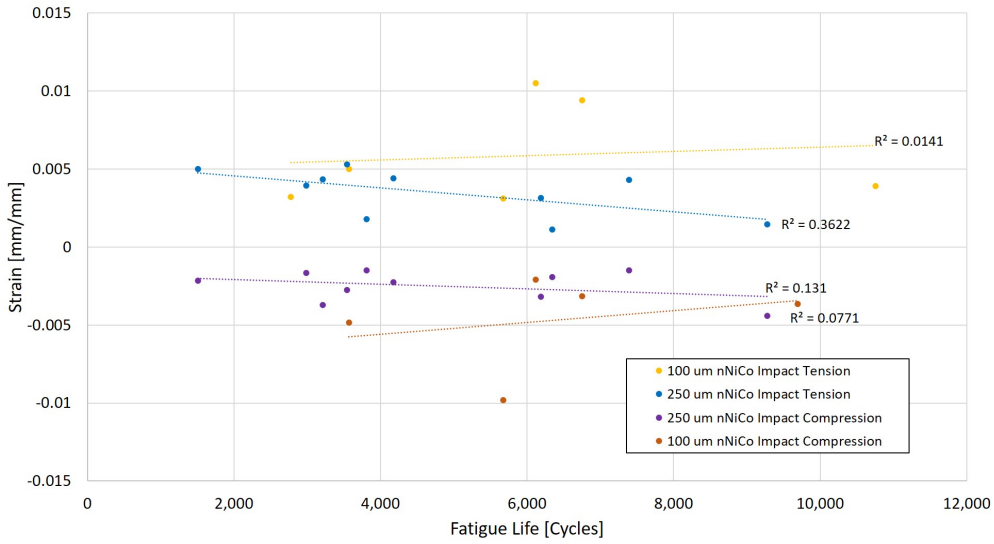

Figure 4.5: DIC maximum strain values in 100 and 250 µm nNiCo impact test specimens on the projectile impact side. R^2 values for linear line of best fit are shown for each data set, indicating poor correlation between maximum strain values in the specimen due to impact and final fatigue life.

µm had higher strains than specimen F7, which had a coating thickness of about 357 µm. The same trend is observed in Figures 4.10 to 4.12, showing specimens tested with an impact energy of around 5.6 J, P9, H4, F4. Finally Figures 4.13 to 4.16 look at the threshold impact energy needed to cause a fracture corresponding to the projectile impact site. Figures 4.13 and 4.14 show specimens H13 and F5 which had an impact energy of about 10 J. Figures 4.15 and 4.16 show specimens H16 and F6 had an impact energy of about 13 J and did fracture at the impact site.

Fatigue Test Strain DIC Analysis

DIC images were taken at regular intervals during the test during the slow cycles in Section 3.3.2 Step 6. A small representative selection of these images is discussed in this section. Note that the colour scales are not consistent between images. Specimen H1 had a coating thickness of approximately 132 µm and a life of 7,836. Interestingly, specimen F12, which had a coating thickness of approximately 321 µm and was tested with an impact energy of 12 J, had a very similar fatigue life of 7,394 cycles. While these tests only represent single data points in their respective test regimes, this shows that there are many factors which contribute to fatigue life, not simply impact energy and coating thickness. The DIC analysis of 250 µm nCo specimen G1, which has an estimated coating thickness of 319 µm, had a fatigue life of one cycle and so is also included here.

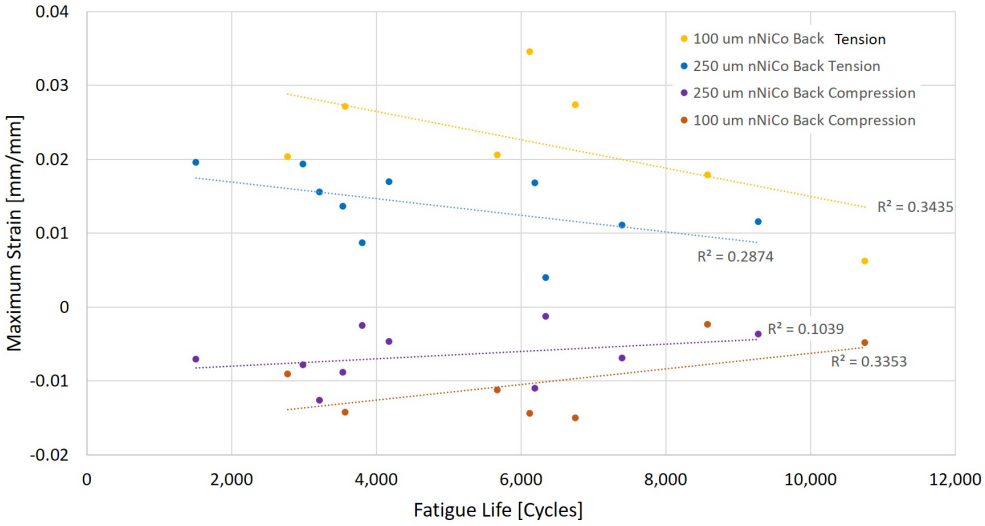

Figure 4.6: DIC maximum strain values in 100 and 250 µm nNiCo impact test specimens on the support side. R^2 values for linear line of best fit are shown for each data set, indicating poor correlation between maximum strain values in the specimen due to impact and final fatigue life.

Specimen H1 Figure 4.17a shows the maximum strain applied during the first cycle, which is confirmed to be approximately 0.6% as per the test plan. The strain map at the end the first cycle is shown in Figure 4.17b, and shows a relatively constant strain through the gauge length of the specimen (the range is 0.003145 mm/mm to 0.0037 mm/mm). Figure 4.18a shows the final image taken before failure, at cycle 6003, showing the characteristic plastic strain contour indicating a fatigue crack [45] [46]. This pattern emerged during cycle 6002 (Figure 4.19b) but was not observable at cycle 4002 (Figure 4.19a). An image of the fractured specimen is shown in Figure 4.18b.

Specimen F12 250 µm nNiCo specimen F12 was tested with an impact energy of 12 J. The area around the indentation initially has the lowest strain, as shown in Figure 4.20a, which could be providing a strengthening effect to the material, similar to shot peening. Shot peening impacts residual compressive stresses in a metal by inducing plastic deformations via a large number of successive impacts all over the surface and can improve the fatigue life of the material [47]. After 4,424 cycles, a high tensile strain in at the indentation is first observed, shown in Figure 4.20b. This stress concentration persisted and the specimen broke at the indentation site at 7364 cycles (Figure 4.21).

Specimen E9 250 µm nCo specimen E9 failed after only one cycle, and it was first thought that it had been overstressed. However, by looking at the DIC images in Figure 4.22a though Figure 4.22c, the average strain in the specimen during the first cycle was approximately 0.6%. The fracture origin point was observed from the first image taken, at a load of about 3,000 N, corresponding to a stress in the coating of about 230 MPa. Since the specimen was not

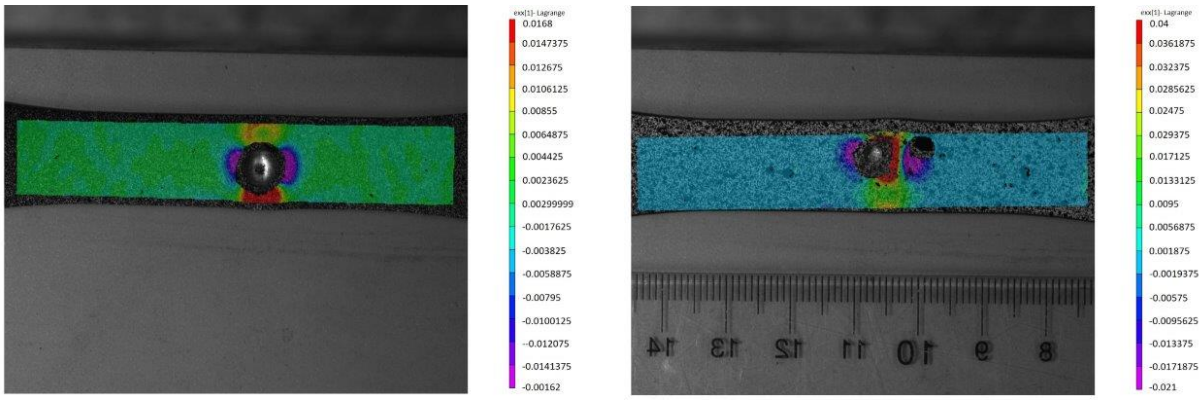

(a) Post-impact axial strain ϵ_{xx} on the front side of the projectile indentation.

(b) Post-impact axial strain ϵ_{xx} on the support side of the projectile indentation.

Figure 4.7: Post-Impact DIC analysis of specimen P12. The projectile had an impact energy of 20.8 J.

overstressed, the fracture surface was photographed to investigate a potential cause of the early failure, see Section 4.2.5.

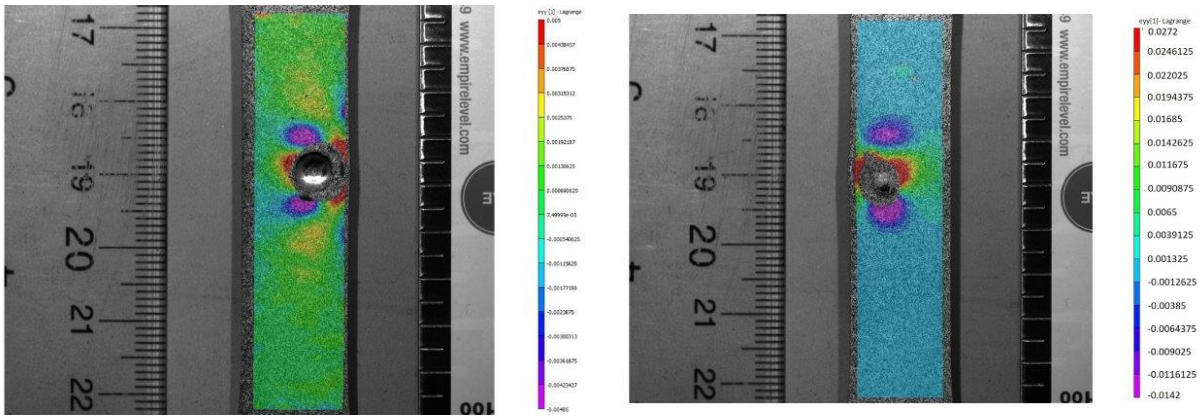

(a) Post-impact axial strain ϵ_{yy} on the front side of the projectile indentation.

(b) Post-impact axial strain ϵ_{yy} on the support side of the projectile indentation.

Figure 4.8: Post-Impact DIC analysis of specimen H5. The projectile had an impact energy of 19.8 J.

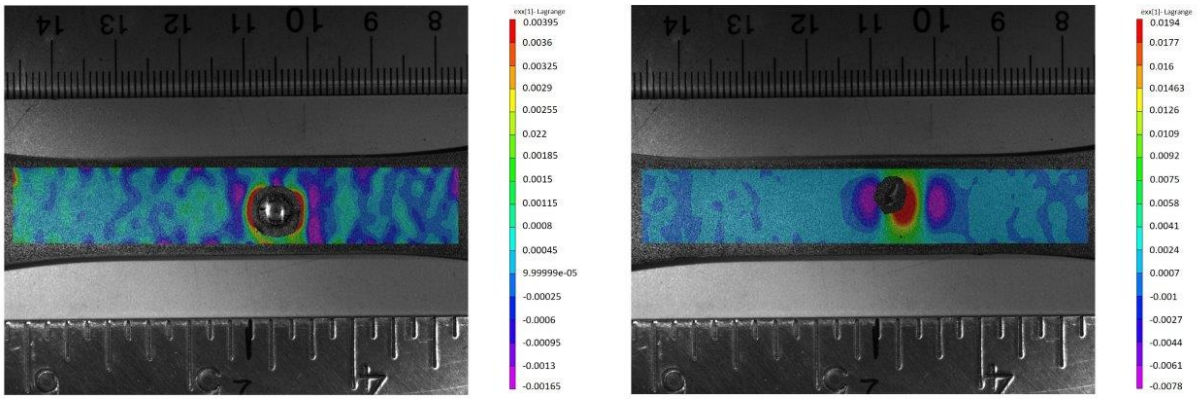

(a) Post-impact axial strain ϵ_{xx} on the front side of the projectile indentation.

(b) Post-impact axial strain ϵ_{xx} on the support side of the projectile indentation.

Figure 4.9: Post-Impact DIC analysis of specimen F7. The projectile had an impact energy of 20 J.

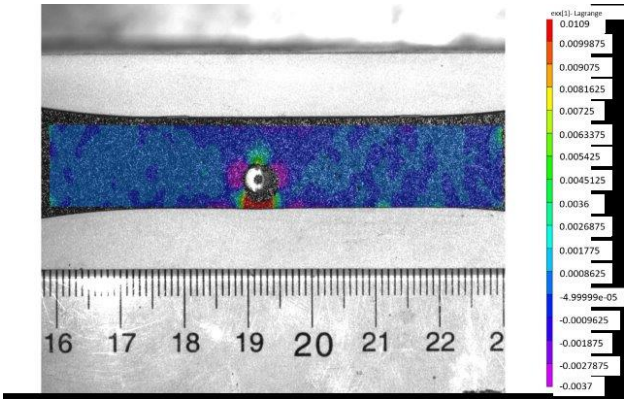

(a) Post-impact axial strain ϵ_{xx} on the front side of the projectile indentation.

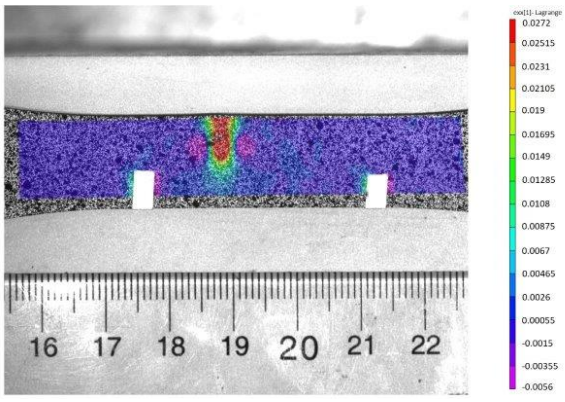

(b) Post-impact axial strain ϵ_{xx} on the support side of the projectile indentation.

Figure 4.10: Post-Impact DIC analysis of specimen P9. The projectile had an impact energy of 5.7 J.

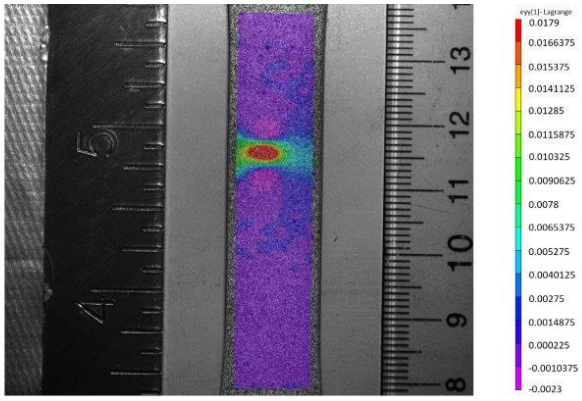

Figure 4.11: Post-impact axial strain ϵ_{yy} on the support side of the projectile indentation of specimen H4. There was no reference image taken for the impact side. The projectile had an impact energy of 5.8 J.

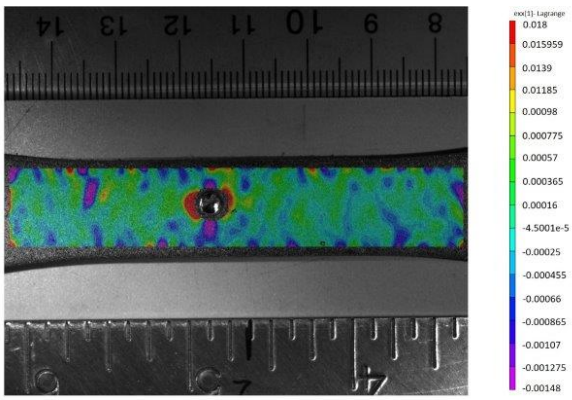

(a) Post-impact axial strain ϵ_{xx} on the front side of the projectile indentation.

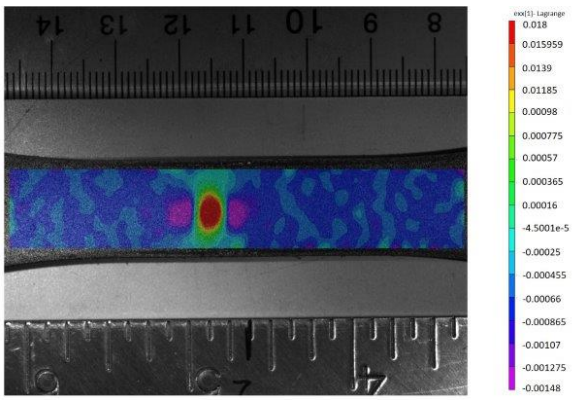

(b) Post-impact axial strain ϵ_{xx} on the support side of the projectile indentation.

Figure 4.12: Post-Impact DIC analysis of specimen F4. The projectile had an impact energy of 5.8 J.

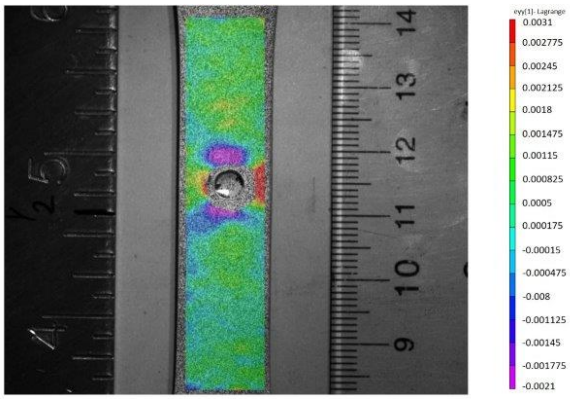

(a) Post-impact axial strain ϵ_{yy} on the front side of the projectile indentation.

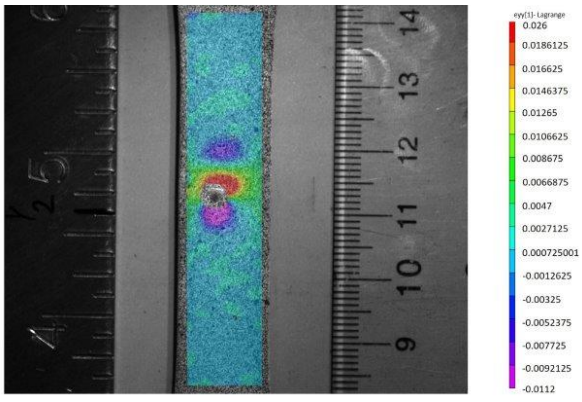

(b) Post-impact axial strain ϵ_{yy} on the support side of the projectile indentation.

Figure 4.13: Post-Impact DIC analysis of specimen H13. The projectile had an impact energy of 9.7 J.

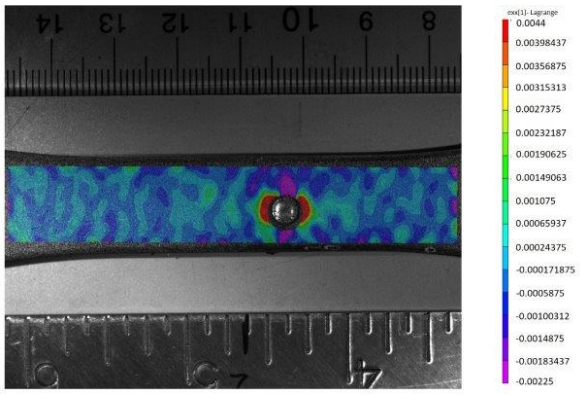

(a) Post-impact axial strain ϵ_{xx} on the front side of the projectile indentation.

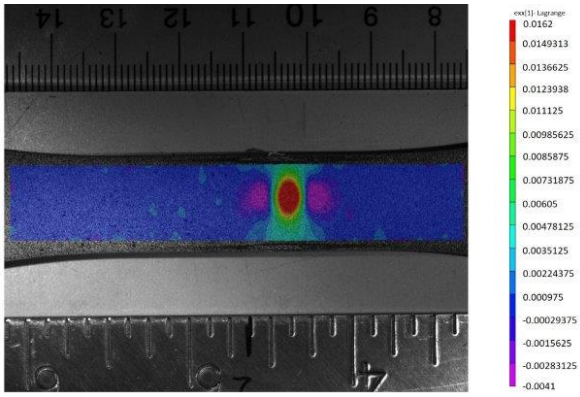

(b) Post-impact axial strain ϵ_{xx} on the support side of the projectile indentation.

Figure 4.14: Post-Impact DIC analysis of specimen F5. The projectile had an impact energy of 9.7 J.

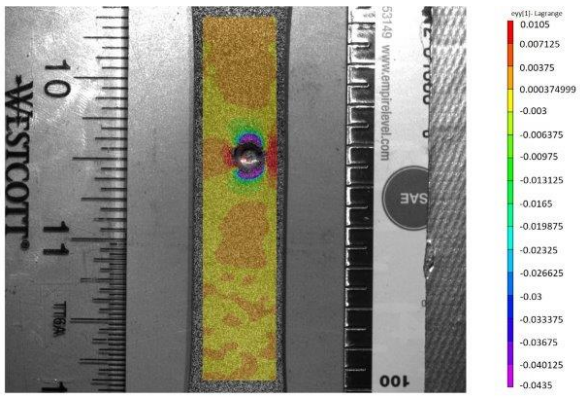

(a) Post-impact axial strain ϵ_{yy} on the front side of the projectile indentation.

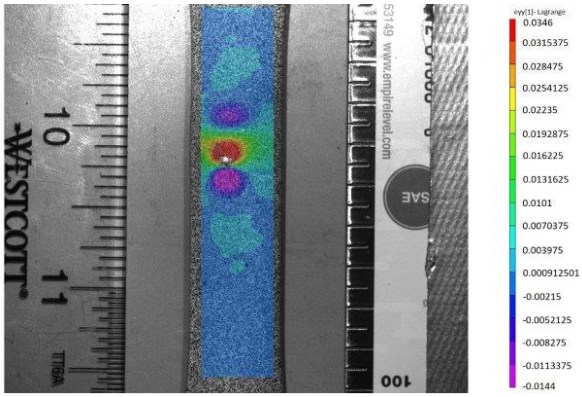

(b) Post-impact axial strain ϵ_{yy} on the support side of the projectile indentation.

Figure 4.15: Post-Impact DIC analysis of specimen H16. The projectile had an impact energy of 12.8 J.

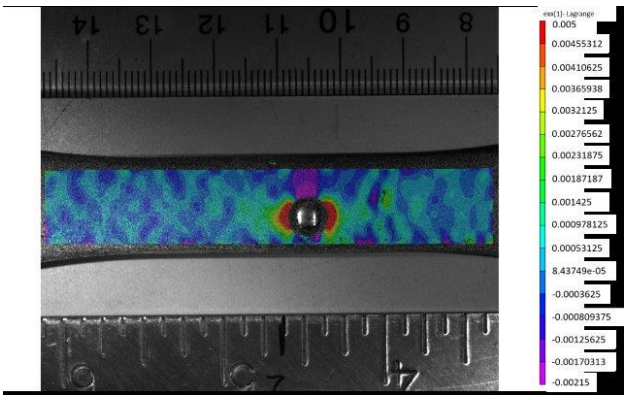

(a) Post-impact axial strain ϵ_{xx} on the front side of the projectile indentation.

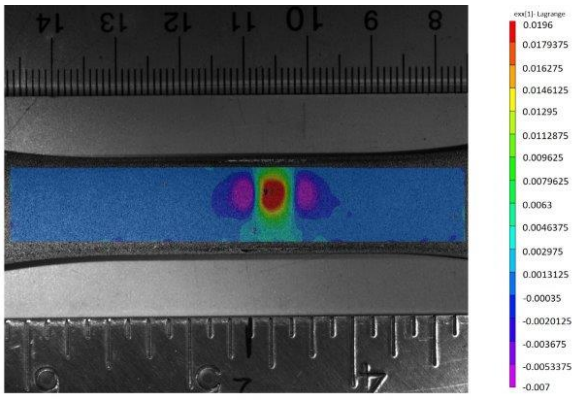

(b) Post-impact axial strain ϵ_{xx} on the support side of the projectile indentation.

Figure 4.16: Post-Impact DIC analysis of specimen F6. The projectile had an impact energy of 13.2 J.

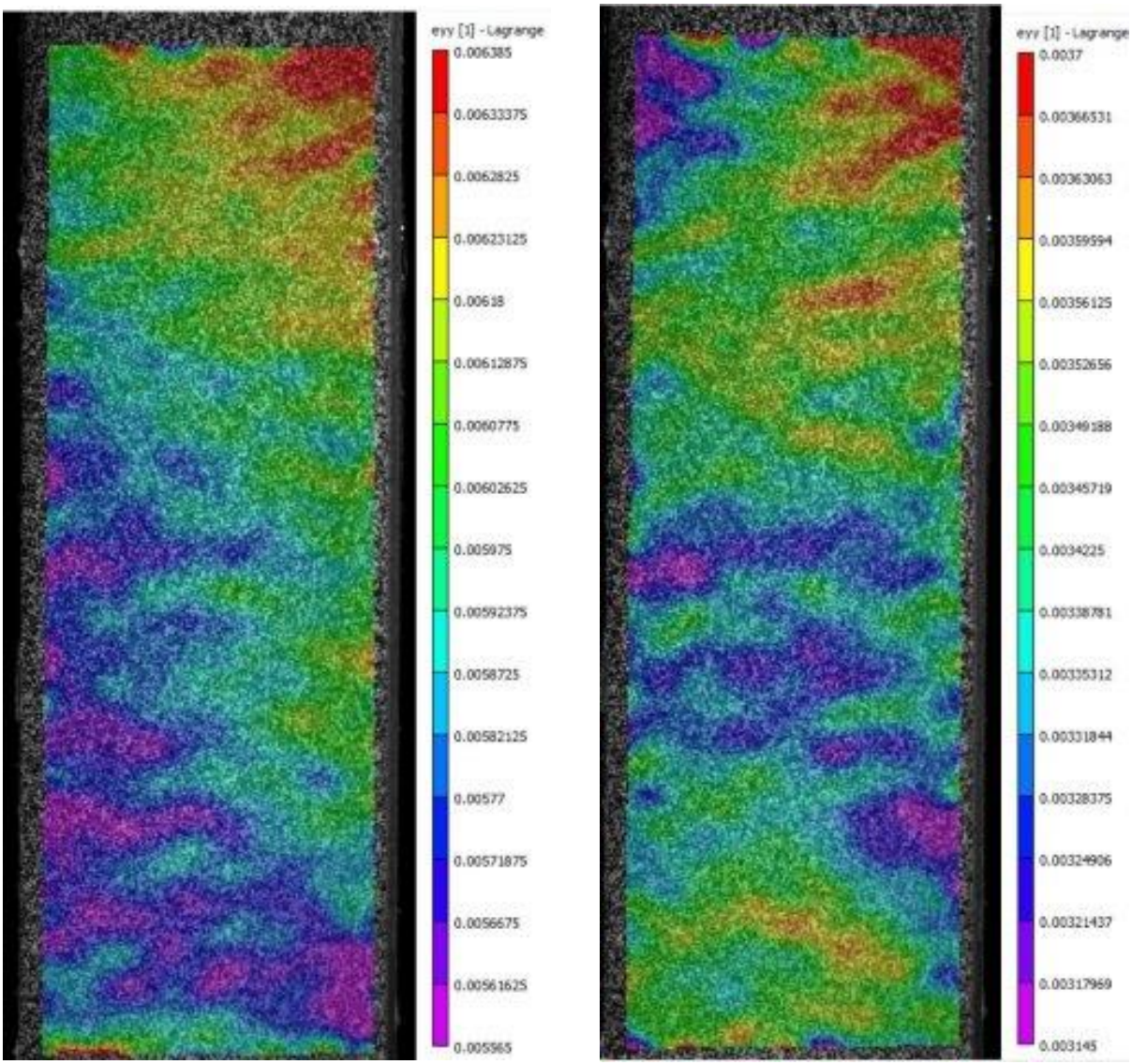

(a) **(b)**

Figure 4.17: DIC analysis of 100 µm nNiCo specimen H1. (a) Average strain in the gauge section was 0.6% strain at maximum applied load in first cycle. (b) DIC analysis strain map after first fatigue cycle.

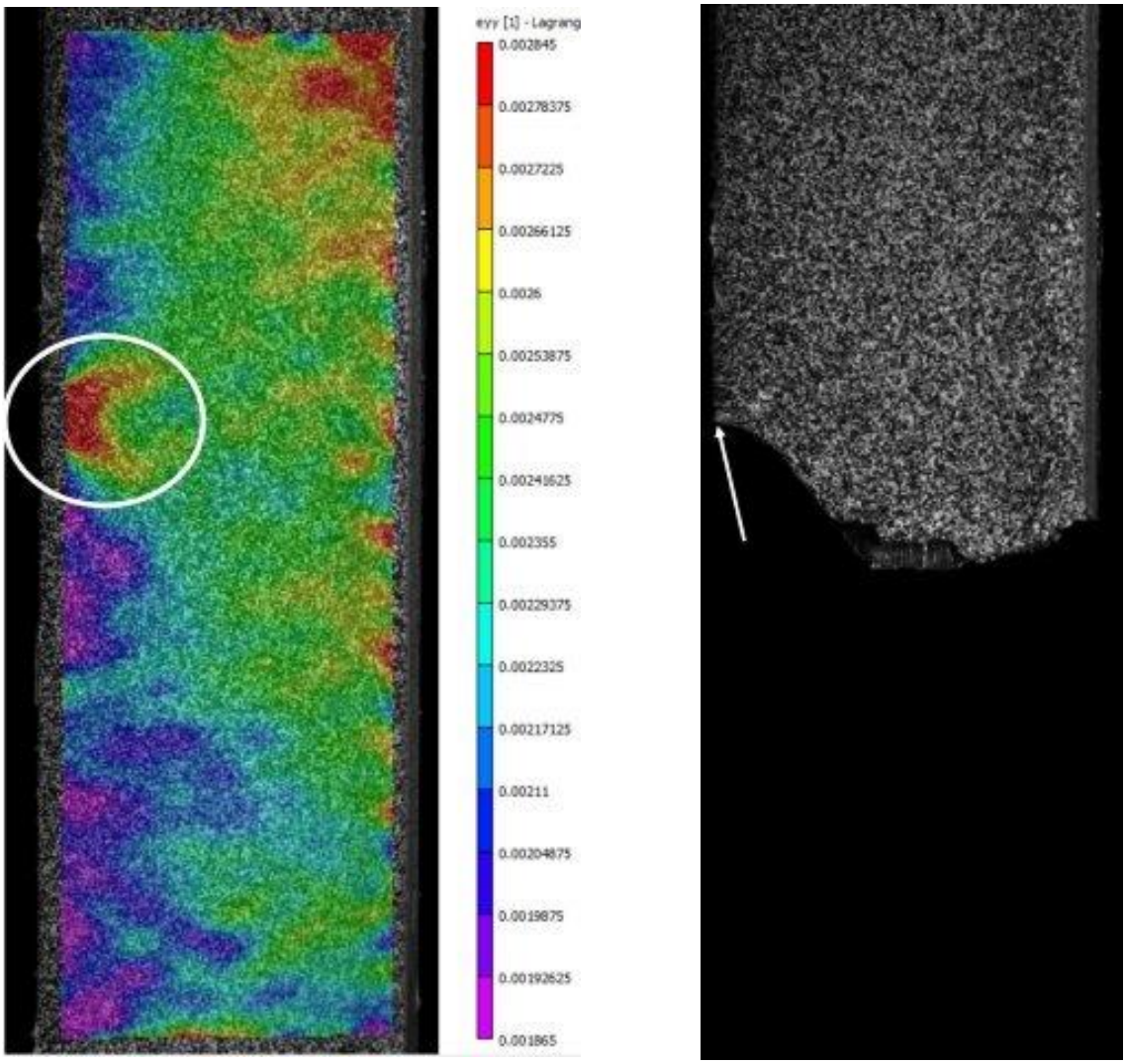

(a) **(b)**

Figure 4.18: DIC analysis of 100 µm nNiCo specimen H1. (a) The last image before fatigue fracture at cycle 6003. The circle indicates the plastic strain contour characteristic of a fatigue crack. (b) The fractured specimen after 7834 cycles, with the fracture origin point indicated by the arrow.

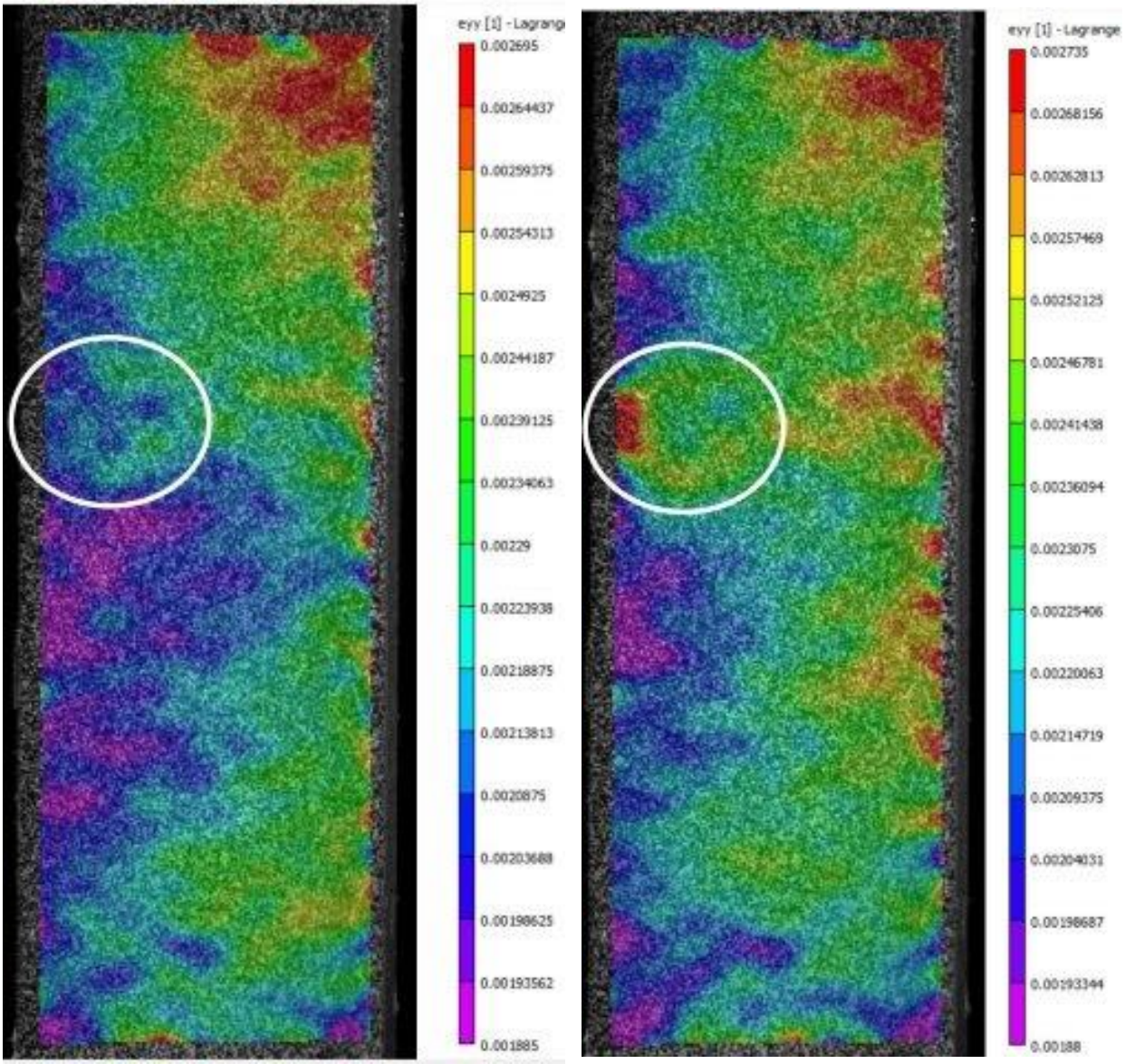

(a) **(b)**

Figure 4.19: DIC analysis of 100 µm nNiCo specimen H1. (a) At cycle 4002 there is no indication of a strain concentration or fatigue crack at the region of the failure origin, indicated by the circle. (b) The next image taken, at cycle 6002, shows an increased strain in the same region.

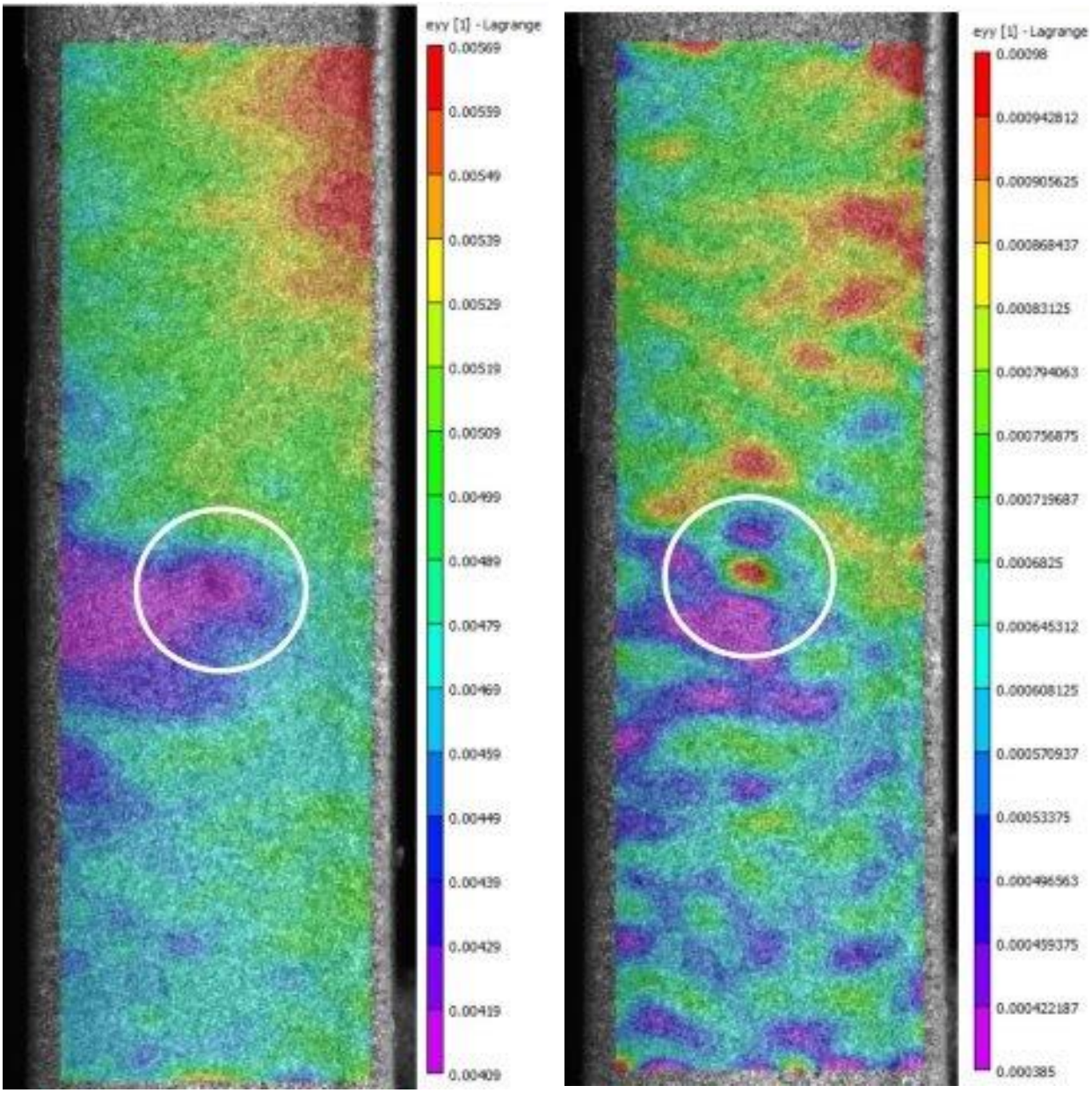

(a) **(b)**

Figure 4.20: DIC analysis of 250 µm nNiCo specimen F12. (a) At the first fatigue cycle, at the maximum applied load, the area around the impact indentation, indicated by the circle, has the lowest strain. (b) At 4,424 cycles, with no applied load, a small area of high strain is observed by the impact indentation.

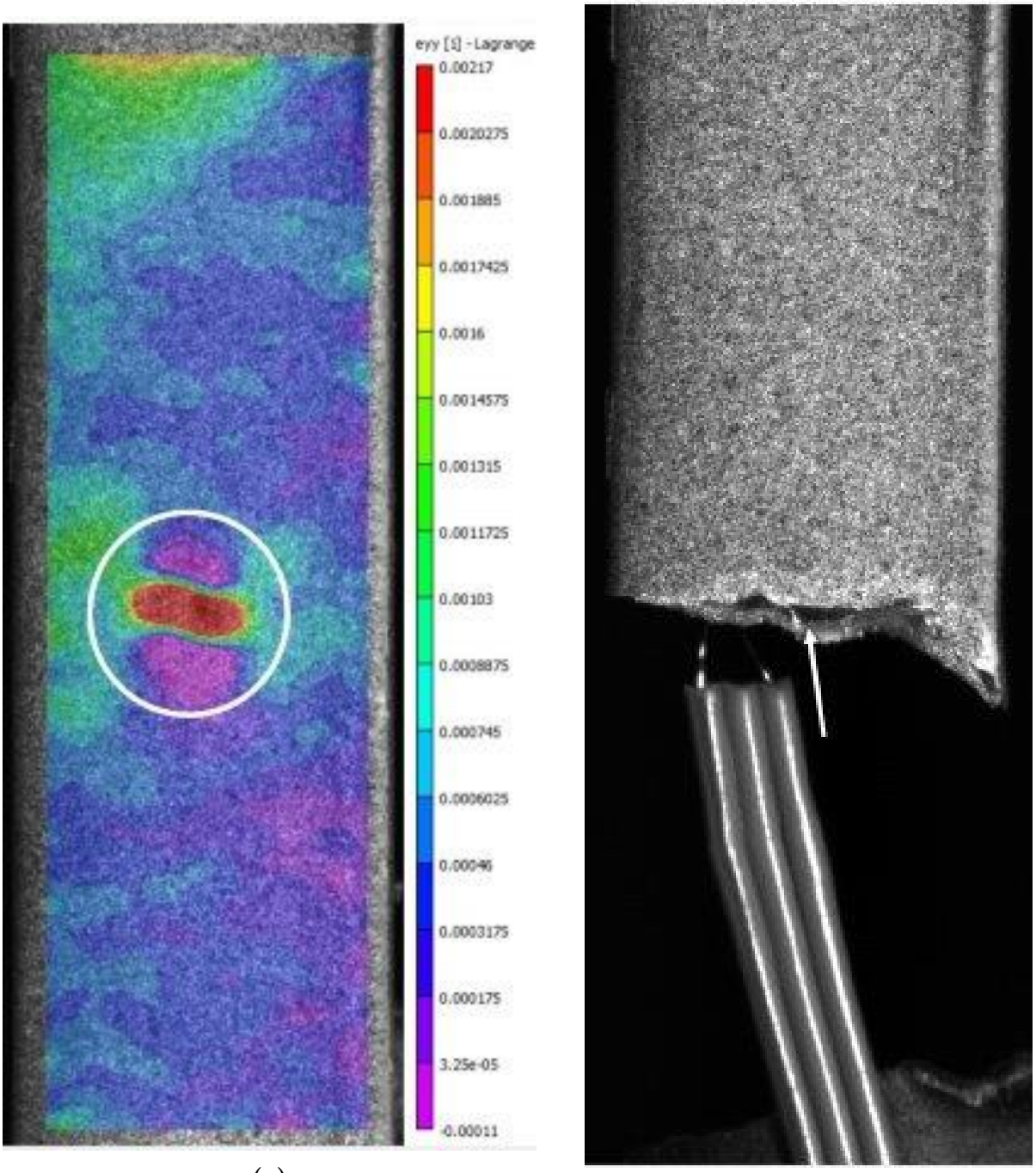

(a) **(b)**

Figure 4.21: DIC analysis of 250 µm nNiCo specimen F12. (a) The last image taken at cycle 6940, with no applied load, showing the strain concentration at the impact indention and fatigue failure origin point. (b) The fractured specimen after 7394 cycles, with the fracture origin point indicated by the arrow.

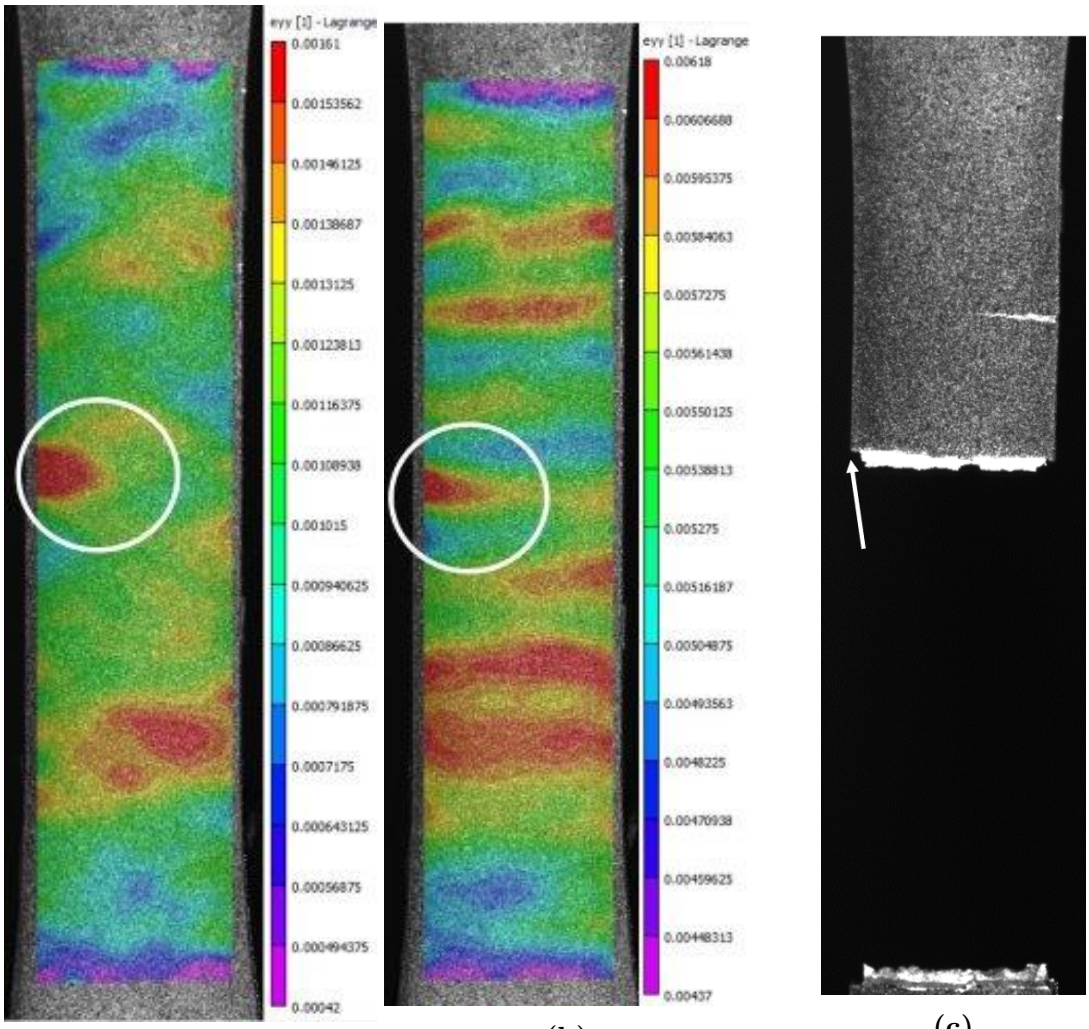

Figure 4.22: DIC analysis of 250 µm nCo specimen E9. (a) The first image taken at the minimum load shows the highest strain at the eventual fracture point. (b) The maximum strain at the the maximum applied load is about 0.6% which was expected. However, this was the last image as the specimen broke as it approached the maximum load. (c) The fracture origin point is indicated by the arrow.

4.2.5 SEM Images

The scanning electron microscope (SEM) at the Ontario Centre for the Characterization of Advanced Materials was used to take images of the fracture surface of the tested specimens, with the goal of more precisely identifying the origin point of the failure. Images of specimens H1, H2, H4, H16, and E9 are included in this section as representative examples.

These images show that the failure initiation point is often at one corner, which is a natural stress concentration, as the coating thickness increases at the corners and along the short edges. Features observed in the coating, such as nodules or indentations, may have also contributed to the failure. During the previous fatigue study done at UTIAS [8], it was thought that debonding contributed to the failure of nNi specimens. However, this was not observed a the failure initiation points on any specimens in this study (with the exception of specimen E9). Debonding was observed in locations opposite to the failure initiation point; it is thought that it occurs due to a shock wave travelling through the specimen at the moment of fracture.

H1 SEM Images

Specimen H1 had a fatigue life of 7,836 cycles. Three potential failure initiation points were observed on the fracture surface, at locations A, B, and C as shown in Figure 4.23. Under magnification, locations A and C appear to be competing failure initiation points.

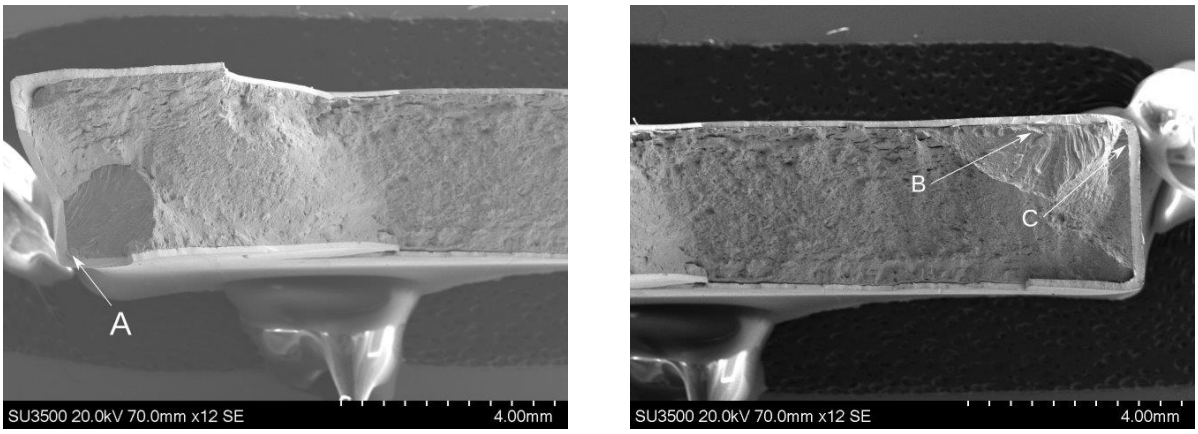

(a) Failure origin point at location A. **(b)** Failure origin points at locations B and C.

Figure 4.23: Fracture surface of specimen H1.

At location A, the coating debonded from the substrate in the corner, leaving the copper interface layer, which is approximately 10 µm thick, attached to the substrate as shown in Figures 4.24 and 4.25. Linear features in the coating are indicated at A', which have been seen in many other specimens near the suspected failure origin point. Magnified images of Location B are shown in Figure 4.26 and 4.27. The area in the circle at B' likely indicates a

region of fast fracture in the substrate. It is shown in greater detail in Figure 4.27.

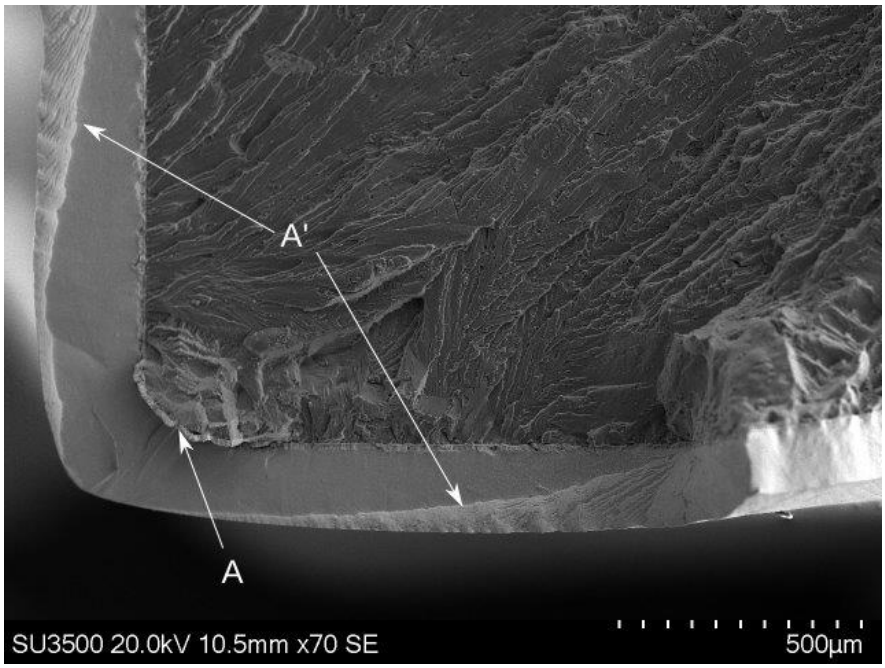

Figure 4.24: Location A on the fracture surface of Specimen H1. Linear features in the coating are indicated by A'.

Magnified images of the coating feature at location C are shown in Figures 4.28, 4.29, and 4.30. It is near the corner diagonal to Location A, and appears to be an indentation in the surface which extends through to the interface layer. This was the only location on the fracture surface of specimen H1 where a feature in the coating was found.

H2 SEM Images

Specimen H2 had a fatigue life of 3,920 cycles. One failure initiation point was observed on the fracture surface at location D as shown in Figure 4.31. A feature in the coating was observed at location E, but it is not likely to have contributed directly to the fatigue failure.

Figure 4.32 and 4.33 show the failure initiation point in more detail. The coating appears to have sheared about halfway through the thickness. Like location A of Specimen H1, the failure has occurred at a corner, and has the same type of linear features radiating from the near the origin point, indicated by D'. The area of coating indicated by the circle in 4.33 is shown in Figure 4.34.

Location E is shown in greater detail in Figures 4.35 and 4.36. The feature in the coating is similar to location C in H1 (Figure 4.30). The difference in thickness between the long edge and the short edge is evident in Figure 4.36, as is the debonding of the substrate from the coating (with the interface layer still adhered to the coating). The appearance of the substrate indicated this is the fast fracture zone.

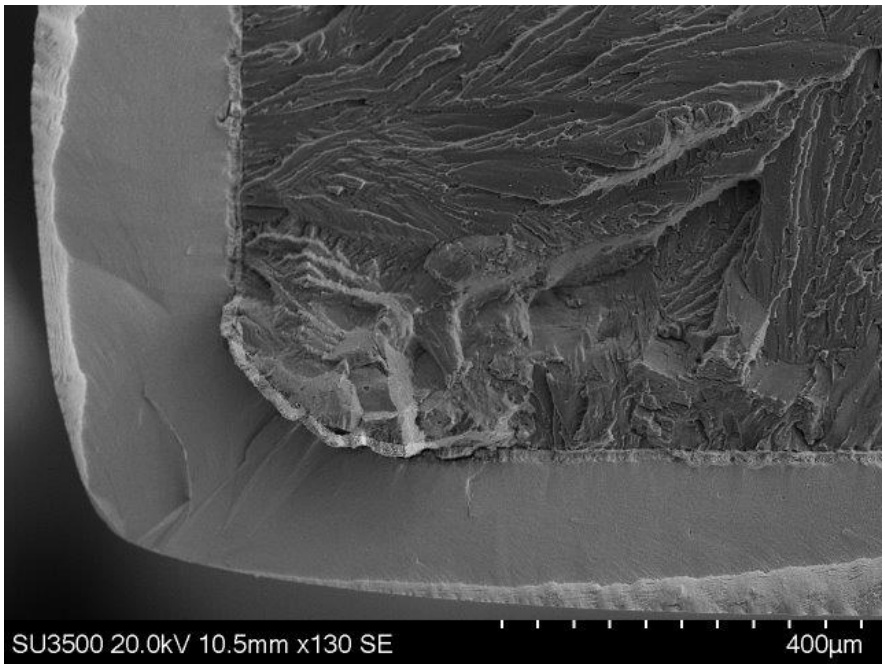

Figure 4.25: Location A on the fracture surface of Specimen H1. The copper interface layer is fully attached to the substrate.

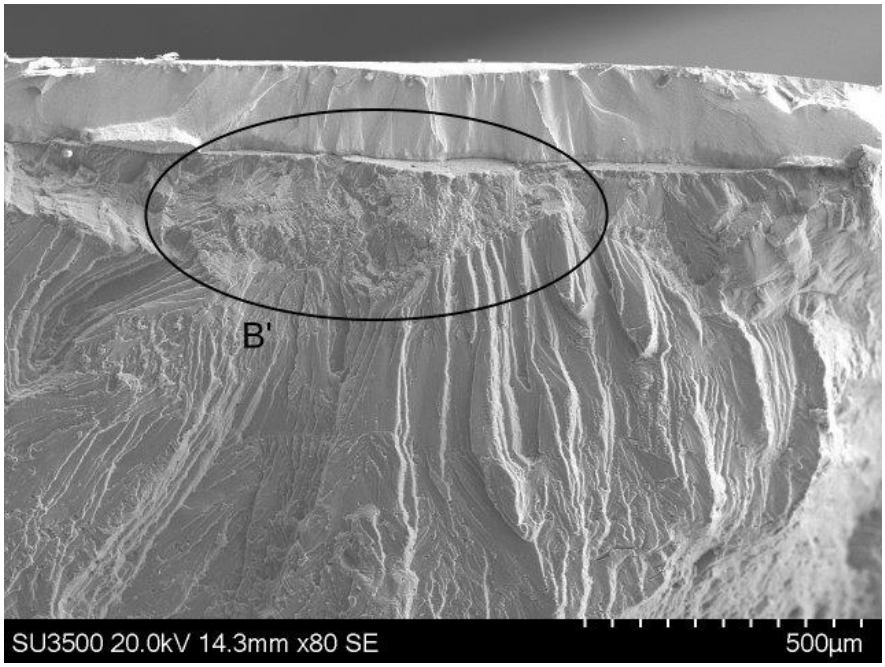

Figure 4.26: Location B' on the fracture surface of Specimen H1. The area in the circle indicates a fast fracture zone in the substrate, and is shown in more detail in Figure 4.27.

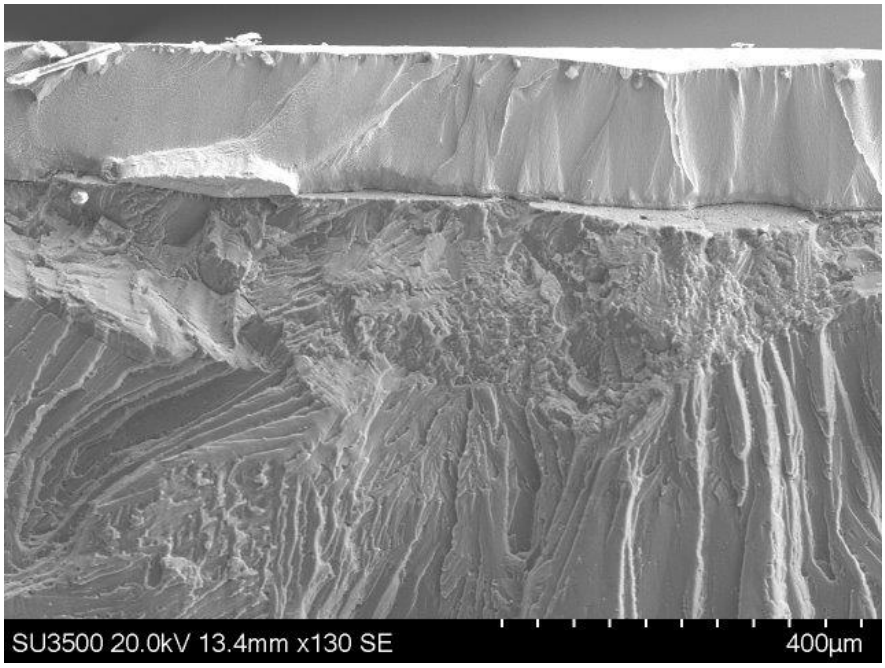

Figure 4.27: Location B' on the fracture surface of Specimen H1.

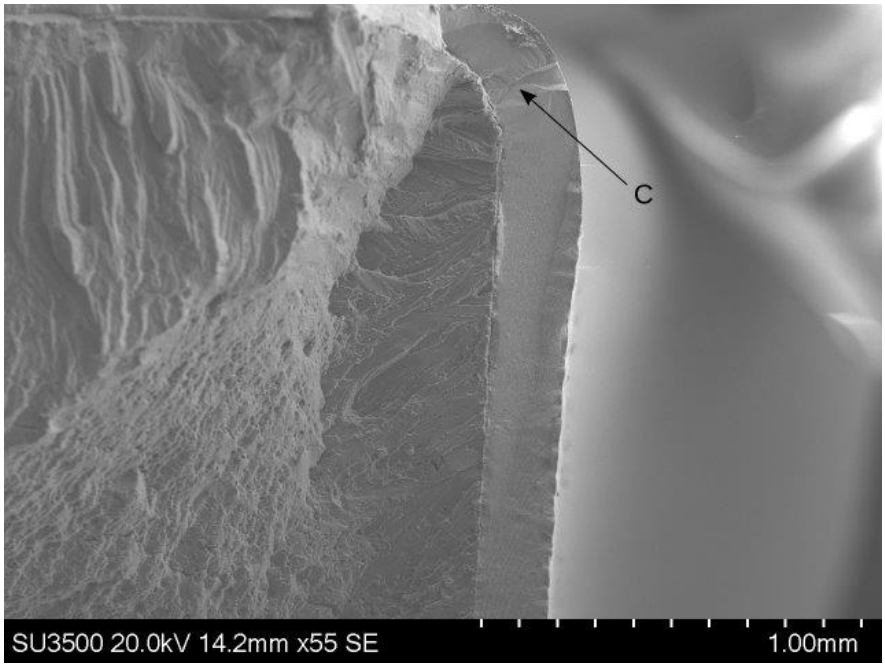

Figure 4.28: Coating feature at Location C in the fracture surface of Specimen H1.

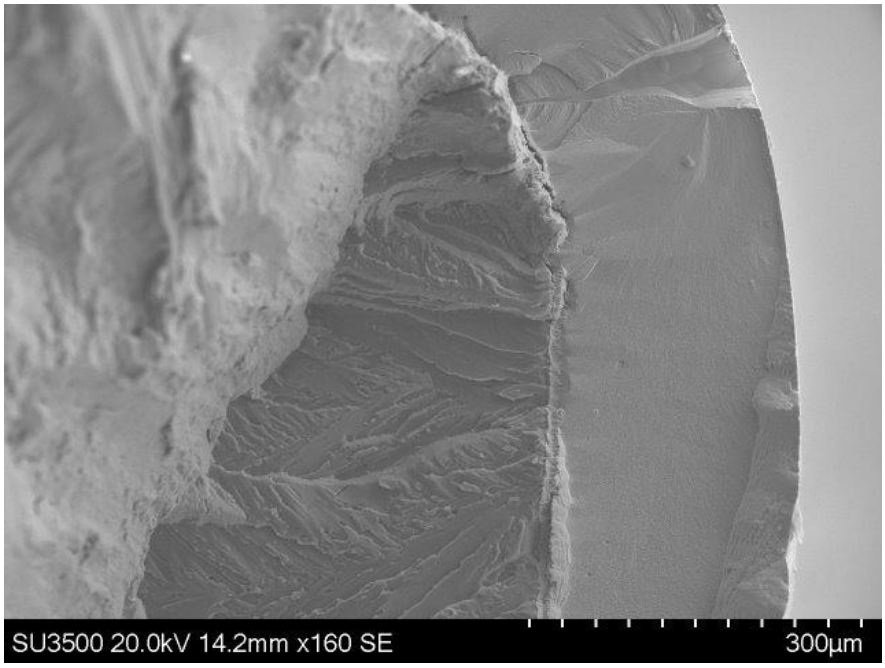

Figure 4.29: Coating feature at Location C in the fracture surface of Specimen H1.

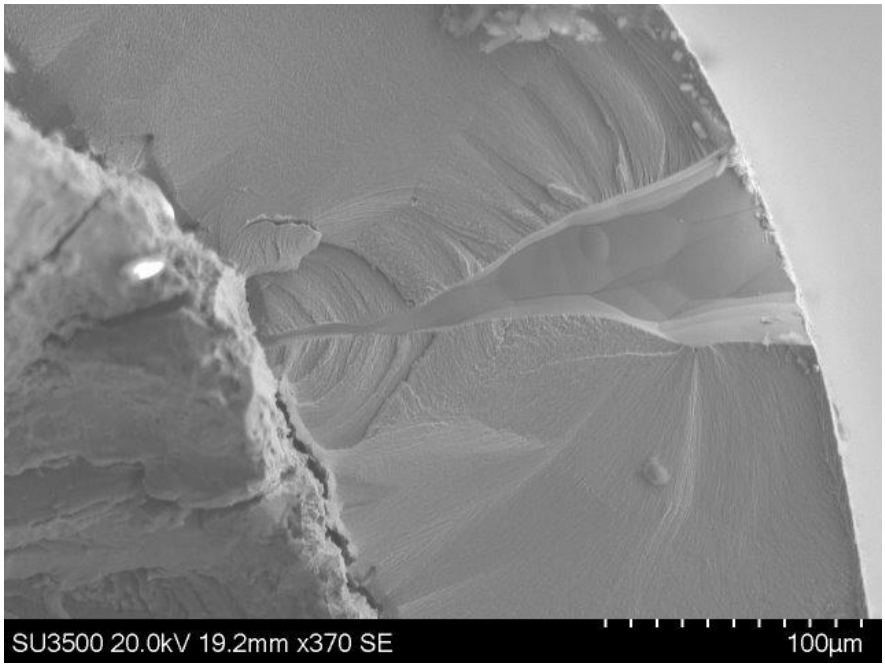

Figure 4.30: Coating feature at Location C in the fracture surface of Specimen H1.

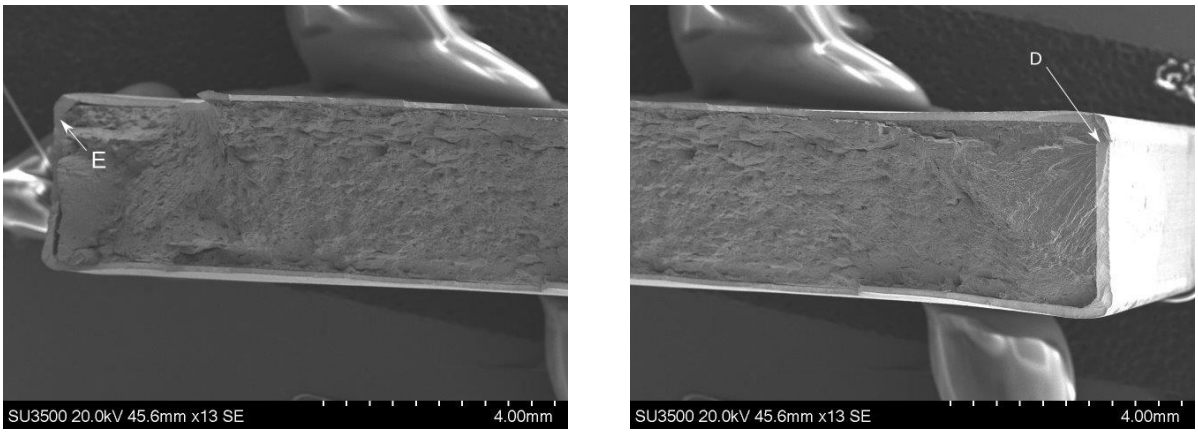

(a) Fracture surface with coating feature at E **(b)** Failure initiation point at D.

Figure 4.31: Fracture surface of specimen H1.

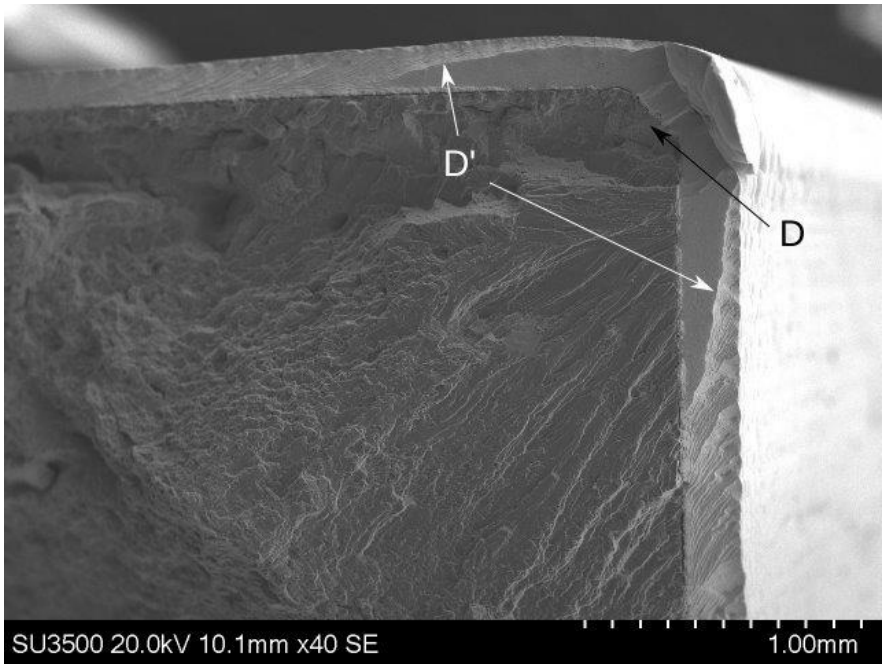

Figure 4.32: Location D on the fracture surface of Specimen H2. Linear features in the coating are indicated by D'.

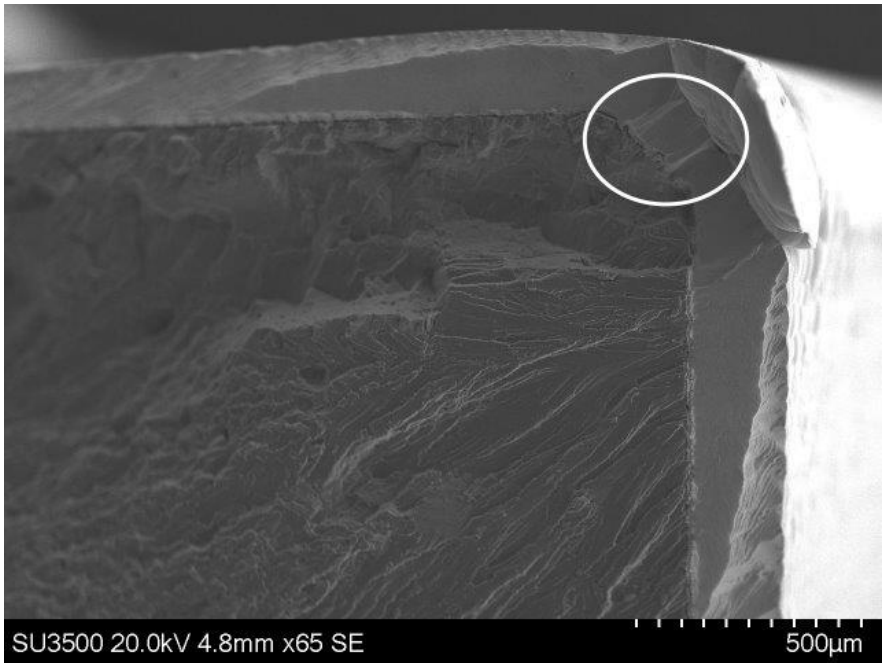

Figure 4.33: Location D on the fracture surface of Specimen H2. The area within the circle can be seen in Figure 4.34.

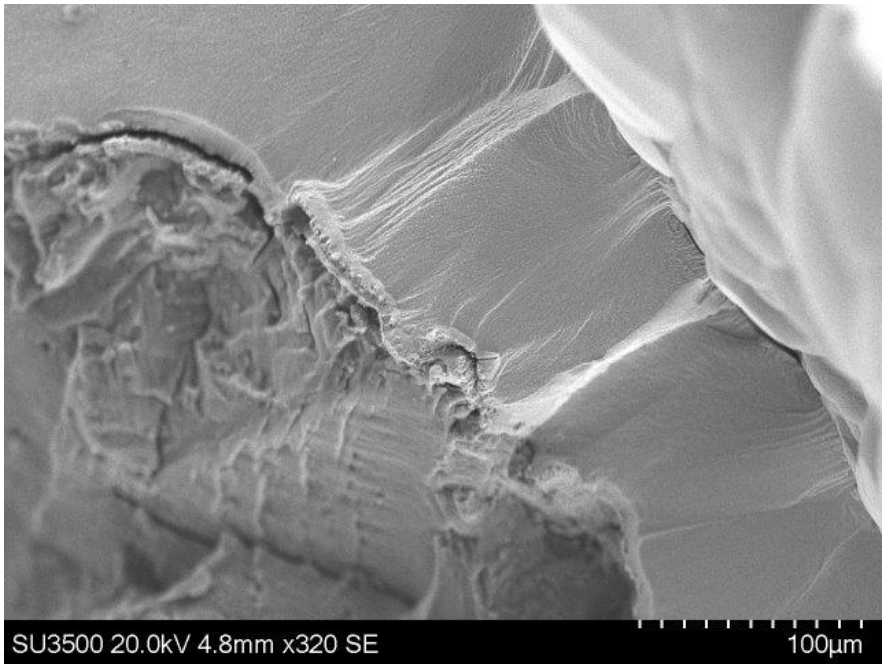

Figure 4.34: Location D on the fracture surface of Specimen H2.

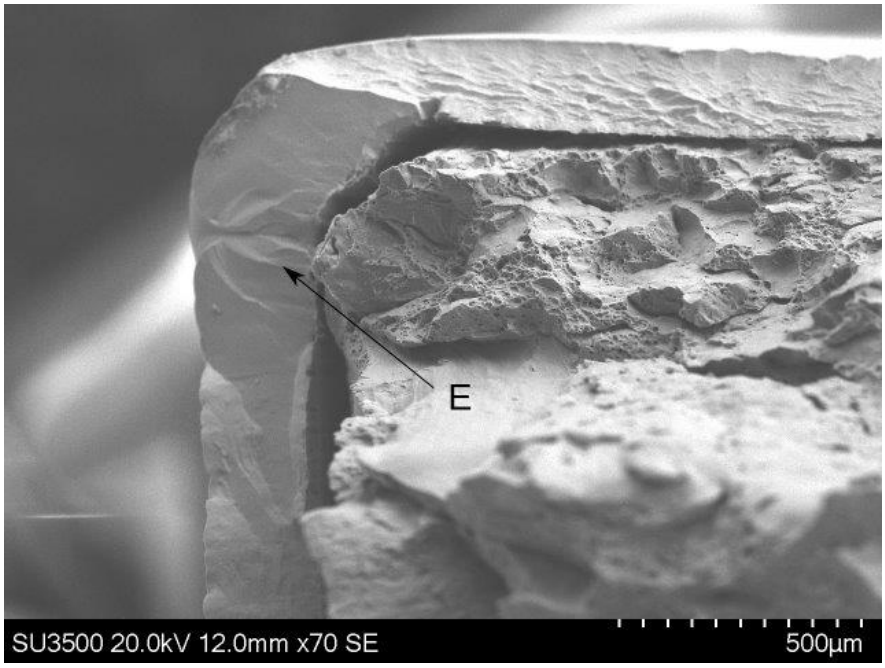

Figure 4.35: Location E in the coating of the fracture surface of Specimen H2.

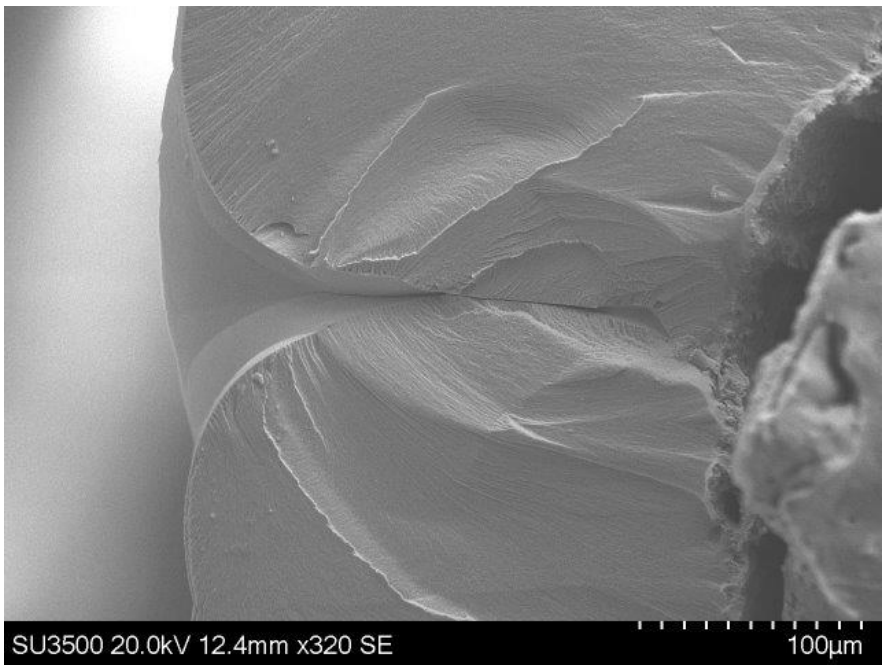

Figure 4.36: Detail of location E in the coating of the fracture surface of Specimen H2.

H4 SEM Images

Specimen H4 underwent an impact of 5.8J, and had a fatigue life of 8,579 cycles. One failure initiation point was observed on the fracture surface at location G as shown in Figure 4.37. The impact site, which away from the fracture surface into the page, is indicated by H.

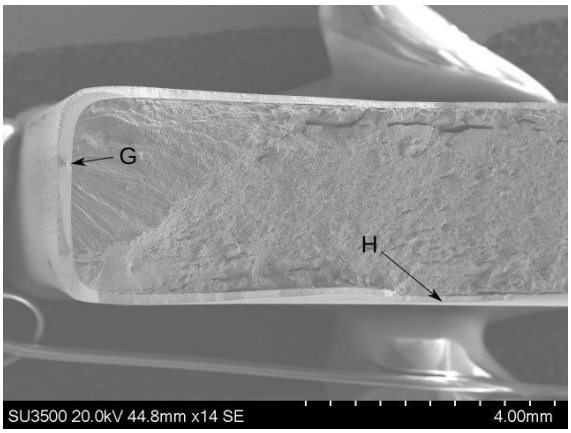

(a) Failure initiation point at G, and projectile impact site at H.

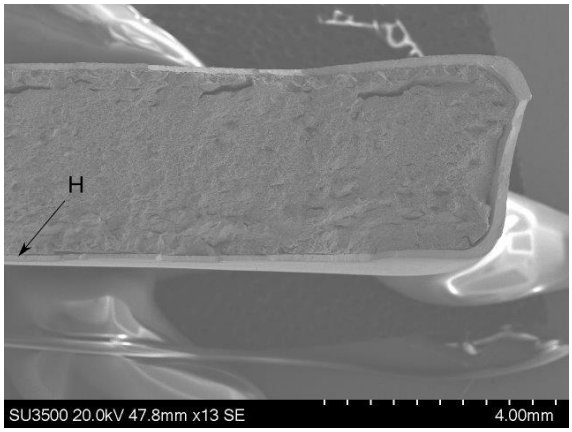

(b) projectile impact site at H.

Figure 4.37: Fracture surface of specimen H4.

Location G is seen in more detail in Figures 4.38, 4.39, and 4.40. It is clear from these images that there is an indentation in the coating which corresponds to the failure initiation point.

Figure 4.41 shows a tilted view of the specimen, near Location H. The impact site is approximately 1 mm away along the specimen's longitudinal axis. This shows that the projectile indention had less effect on the location of the plane of the fracture surface compared to specimens tested with higher impact energies, for example specimen H16 (see Figure 4.48).

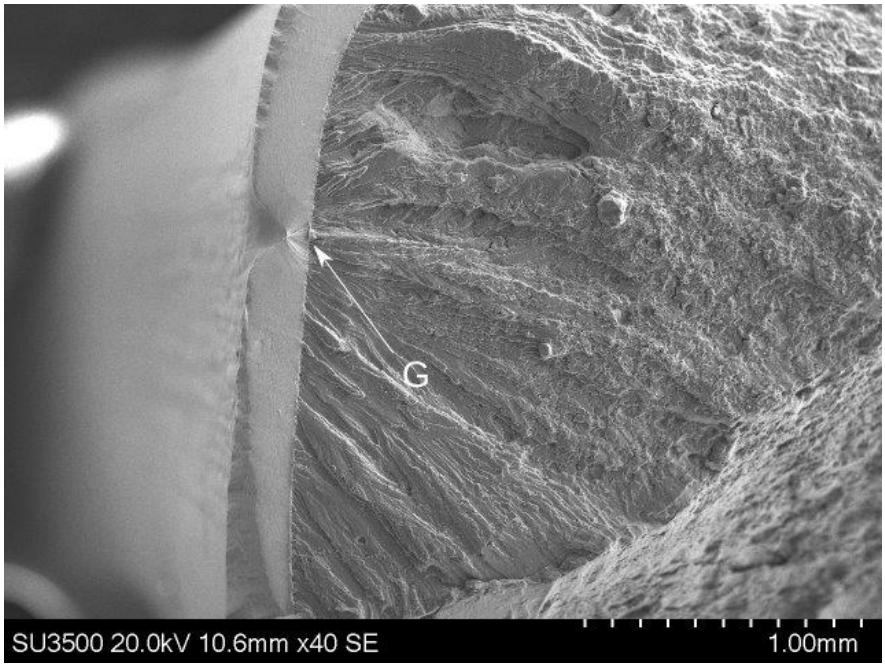

Figure 4.38: Indentation at location G in the coating of the fracture surface of Specimen H4.

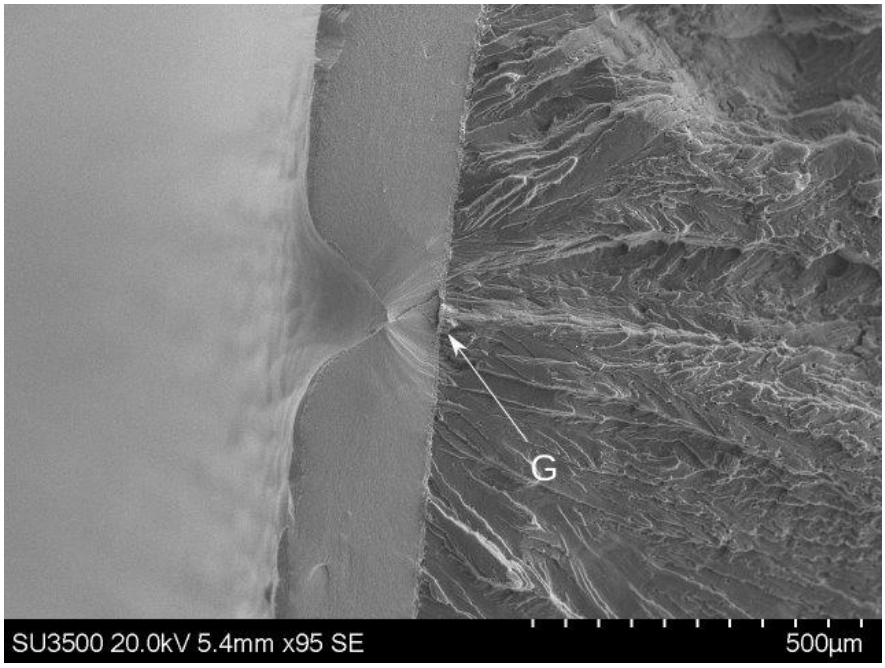

Figure 4.39: Indentation at location G in the coating of the fracture surface of Specimen H4.

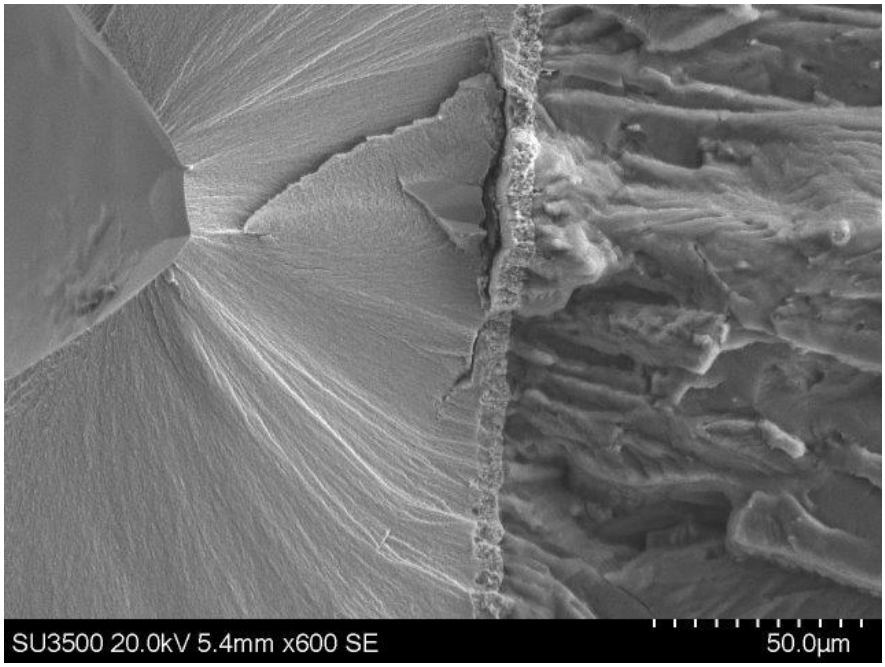

Figure 4.40: Detail of location G in the coating of the fracture surface of Specimen H4.

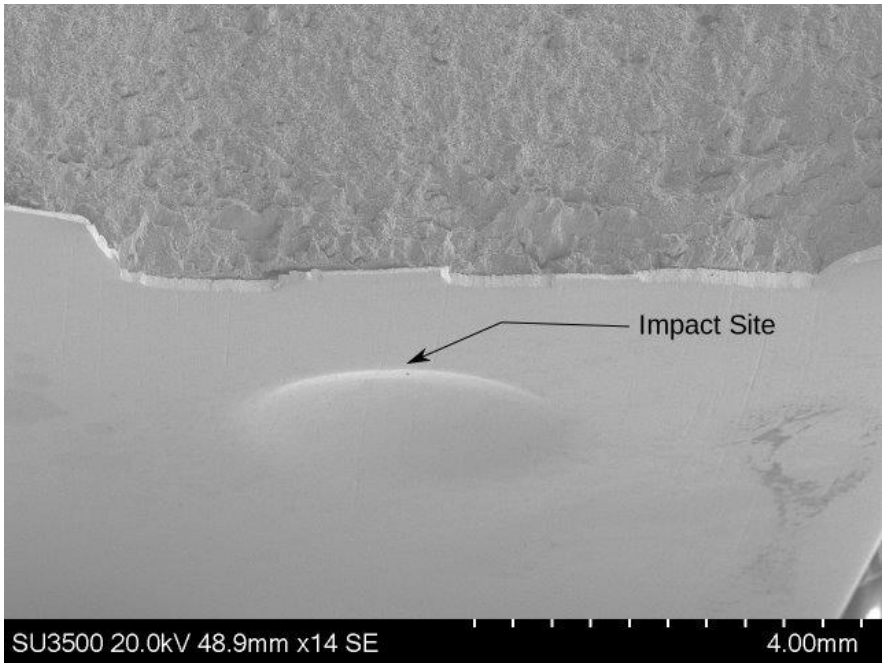

Figure 4.41: Tilted view of the fracture surface near Location H (per Figure 4.37) of Specimen H4, also showing the projectile impact site.

H13 SEM Images

Specimen H13 underwent an impact of 9.7J, and had a fatigue life of 5,673 cycles. Two potential failure initiation points were observed on the fracture surface, at locations I and J as shown in Figure 4.42. The impact site, which is below the fracture surface, is indicated by K.

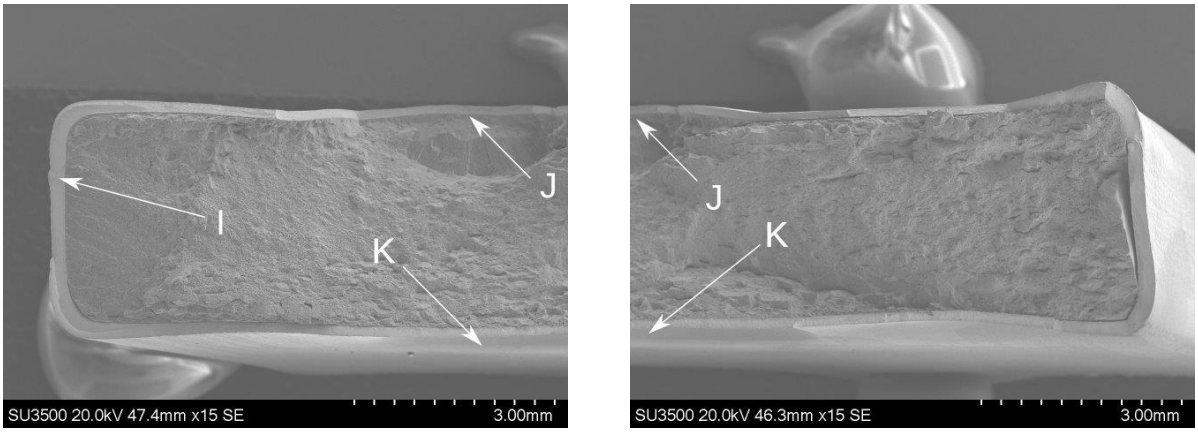

(a) Failure initiation points at Locations I and J, and impact site at Location K.

(b) Failure initiation point at Locations J and impact site at Location K.

Figure 4.42: Fracture surface of specimen H13.

A nodule was found at Location H, which is shown in greater detail in Figures 4.43, 4.44, and 4.45. The specimens were polished in an attempt to remove these features, however, it is more difficult to adequately polish the short edges, and evidently some nodules remained. Location J corresponds to the support side of the indentation created by the projectile impact, where the specimen is in contact with the test jig. This area is shown in greater detail in Figures 4.46 and 4.47. No features appear in the coating in this area.

H16 SEM Images

Specimen H16 underwent an impact of 12.8J, and had a fatigue life was 6,118 cycles. One failure initiation points were observed on the fracture surface at location L, which corresponds to the back of the indentation created by the projectile impact, is shown in Figure 4.48. The impact site, is in line fracture surface (i.e. the specimen broke at the middle of the impact indentation), is indicated at location M.

Location L has a convex shape, relative to the plane of the fracture surface, and is shown in more detail in Figures 4.49 and 4.50. Location M at the impact site is shown in more detail in Figure 4.51.

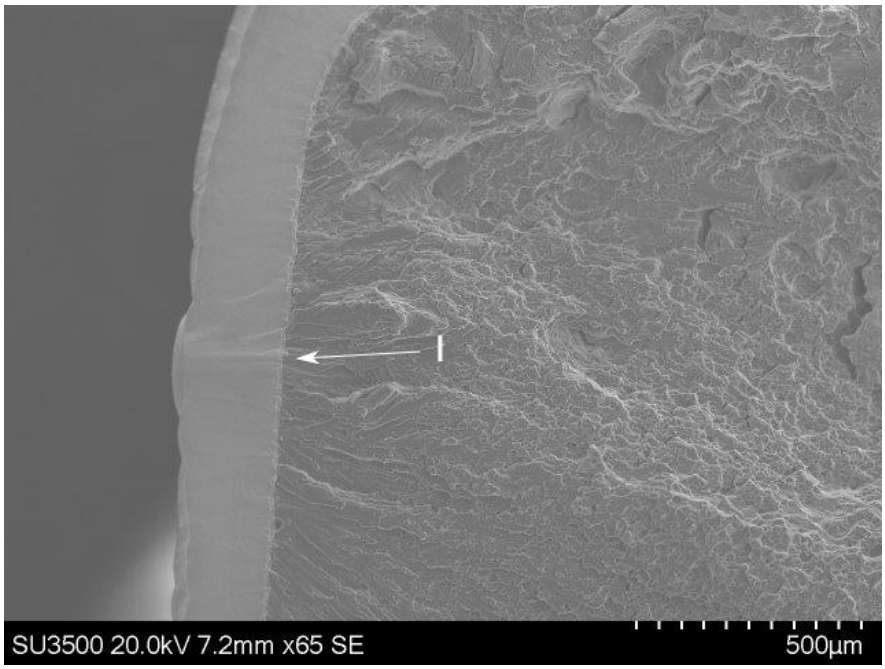

Figure 4.43: Nodule near location I on fracture surface of Specimen H13.

Specimen E9

Specimen E9 had a fatigue life of only one cycle. The fracture surface was imaged using a digital single-lens reflex (DSLR) camera. The images show some voids in the coating at the two corners of the coating, at locations N and O in Figure 4.52. A more detailed view of location N is shown in Figure 4.53. The substrate and the coating are not bonded over much of the specimen width, as indicated at P in Figure 4.52; it is not clear if this happened during the failure or if this was the cause.

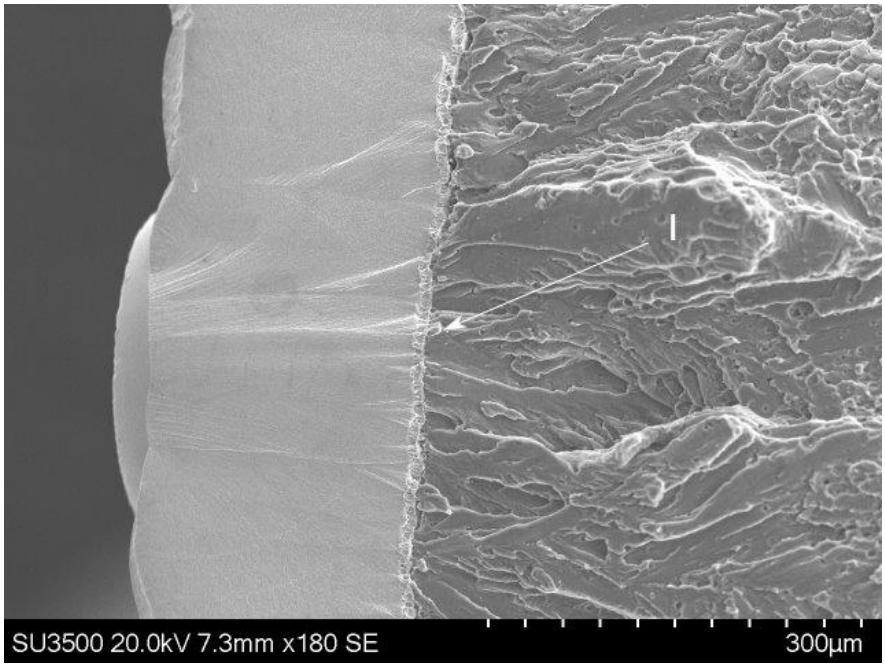

Figure 4.44: Nodule near location I on fracture surface of Specimen H13.

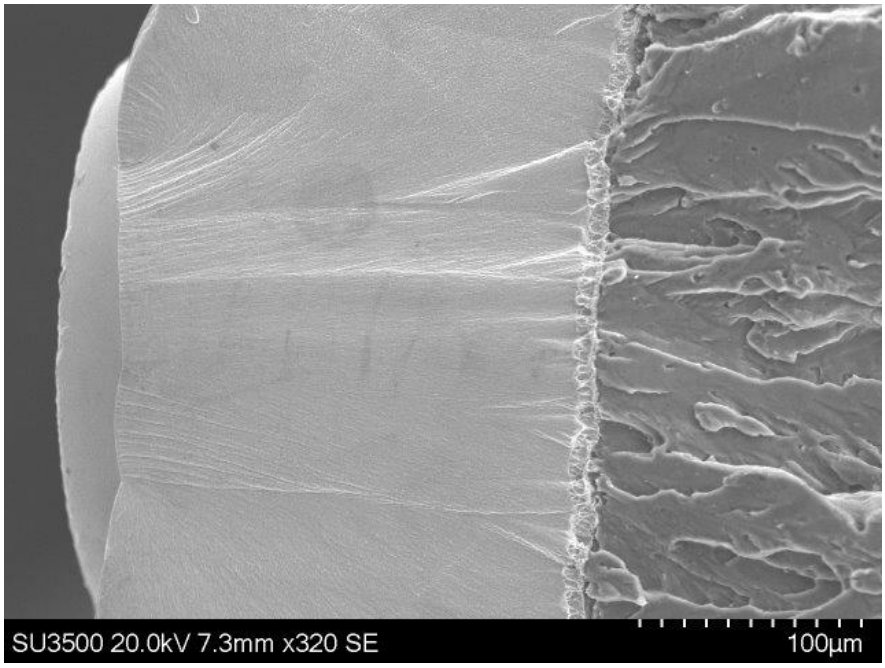

Figure 4.45: Detail view of nodule and coating near location I on fracture surface of specimen H13.

Figure 4.46: Location J on fracture surface of Specimen H13, which corresponds to the support side of the impact indentation.

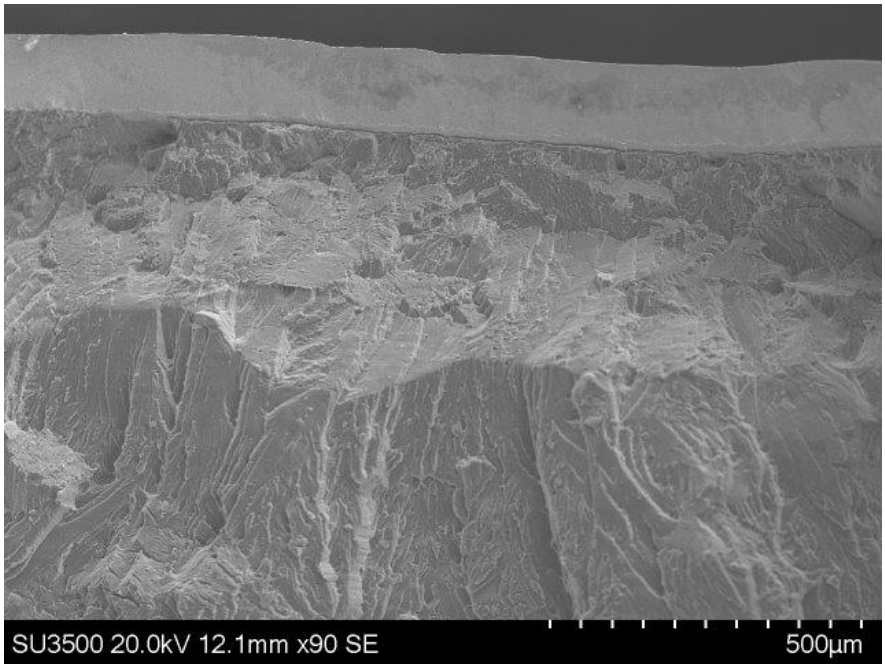

Figure 4.47: Detail view location J on fracture surface of specimen H13.

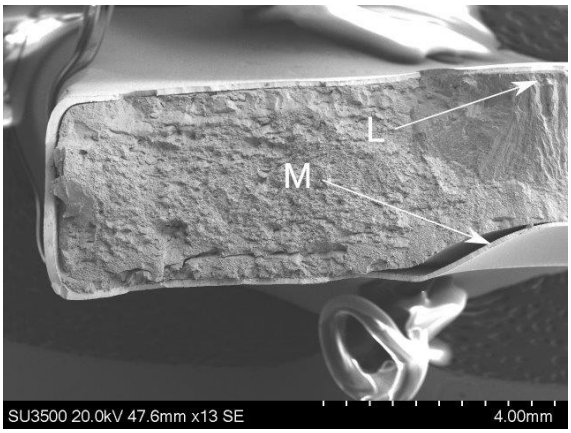

(a) Failure initiation point at locations L and impact site at Location M.

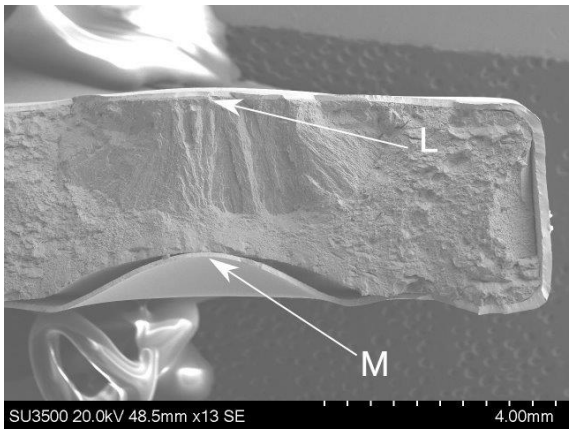

(b) Failure initiation point at locations L and impact site at Location M.

Figure 4.48: Fracture surface of specimen H16.

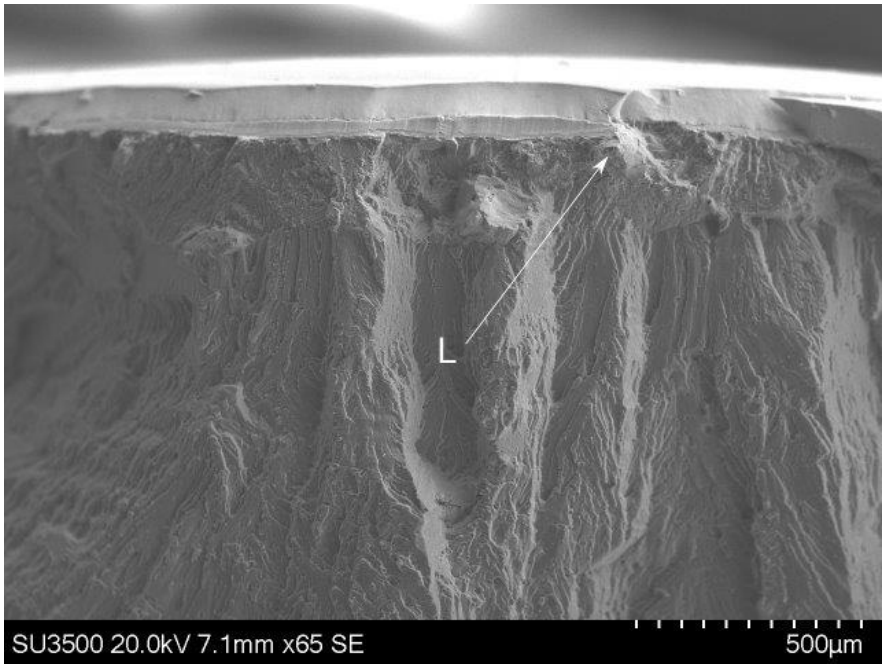

Figure 4.49: Location L on fracture surface of specimen H16.

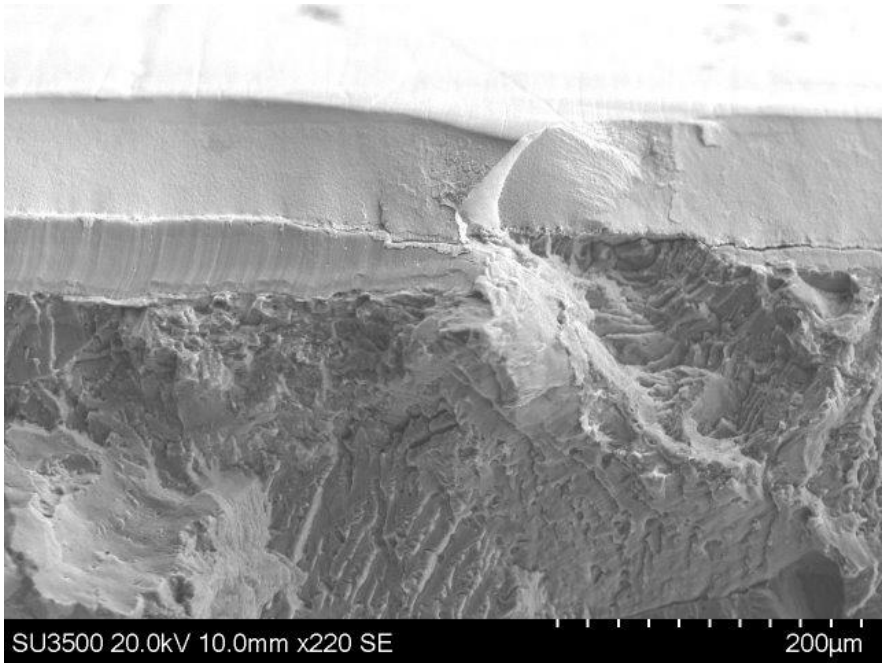

Figure 4.50: Detail view location L on fracture surface of specimen H16.

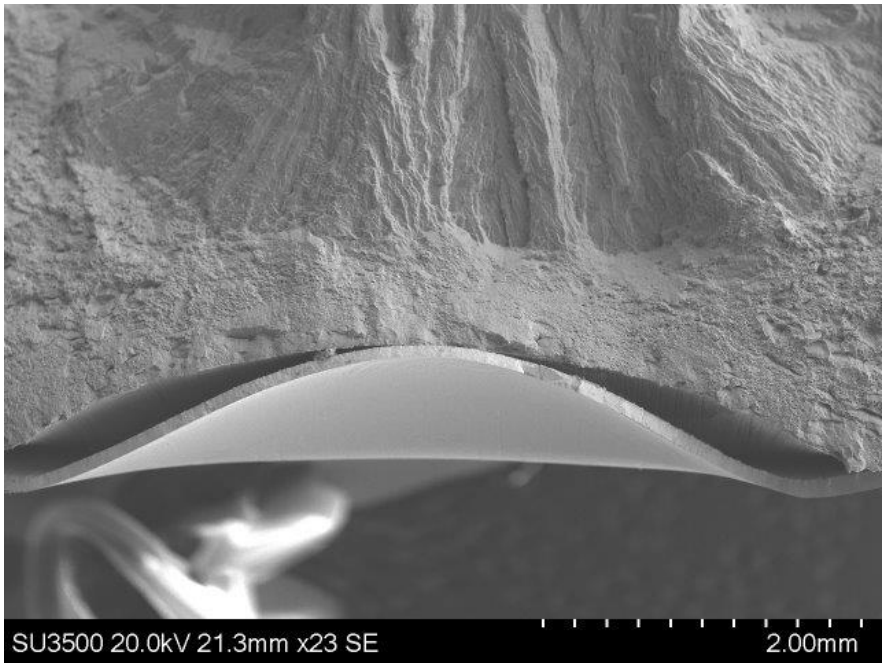

Figure 4.51: Detail view location M near the impact site on fracture surface of specimen H16.

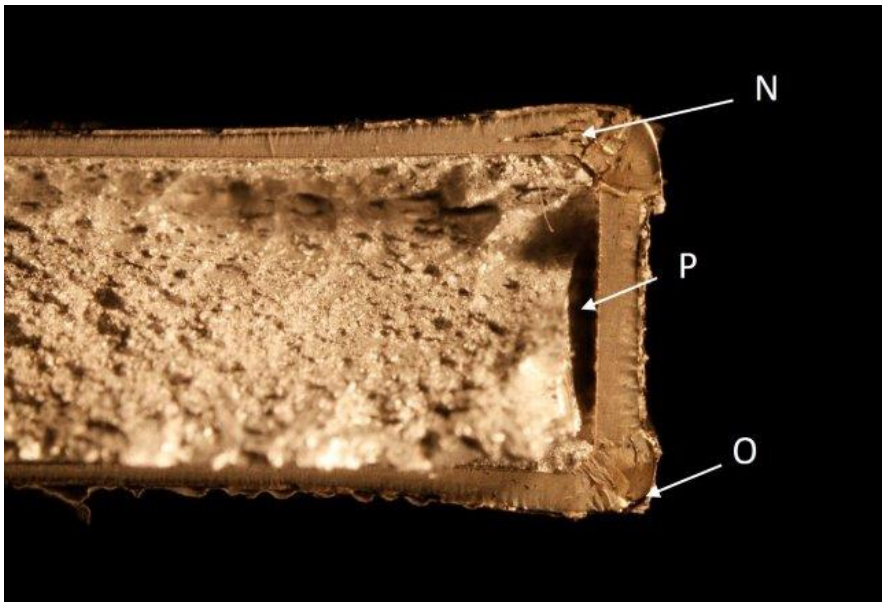

Figure 4.52: A DSLR image of 250 μm nCo specimen E9 showing voids in the coating at locations N and O, and debonding between the substrate and the coating at location P.

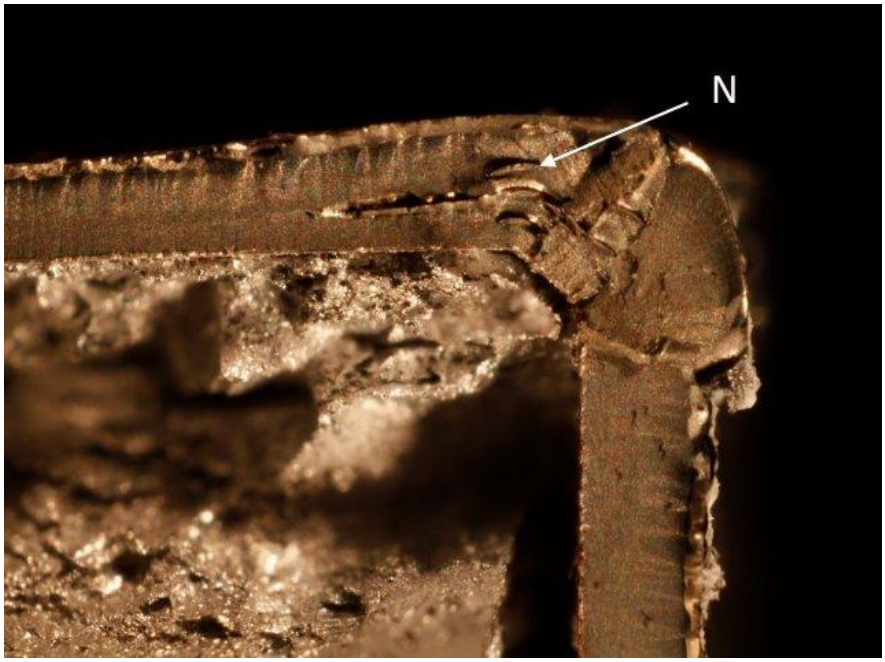

Figure 4.53: A DSLR image of 250 μm nCo specimen E9 showing a detailed view of voids in the coating at location N. These voids may be cause of the failure of the specimen after one fatigue cycle.

4.2.6 Calculation of the Induced Stress in the Substrate and Coating

The coating stresses were obtained based on the assumption that the substrate stress-strain relationship is well-defined, and the strain is equal in the coating and the substrate. Equation 3.3 from Section 3.3.3 is re-arranged as:

$$F_C = F_T - F_S \tag{4.1}$$

If stress-strain curves are generated using Equation 4.1 assume no induced stresses (i.e. stress in both substrate and coating are zero when strain is zero), the coating stress-strain curve has an unrealistic non-linearity around 0.4% strain, as shown in Figure 4.54a.

Moving the substrate curve to the left along the x-axis reduces this non-linearity, which suggests induced stresses are present in the specimen. Figure 4.54b indicates the specimen has an induced tensile stress in the coating, because the coating curve crosses the y-axes at a positive stress value, and an induced compressive stress in the substrate, as the substrate curve crosses the y-axis at a negative value. Based on literature reviews, it is thought these stresses originate in the manufacturing process. The estimated induced stress values are determined by first fitting a polynomial to the coating stress-strain curve. The smoothest curve is determined by minimizing the sum of the squares of the second derivative of the polynomial, and the induced stresses are the values at which the coating and substrate curves cross the y-axis (i.e. at zero strain). The maximum stress seen in the coating and substrate is recalculated to include the induced stress, by adding tensile stresses and subtracting the compressive stress. The substrate stresses remain flat across the entire range of fatigue lives, as shown in Figure 4.55. It is clear that the stresses in the substrate do not dictate the fatigue life. Figure 4.56 shows the S-N curve using the maximum coating stress, which exhibits the expected behaviour of lower stresses resulting in a longer fatigue life. It is not clear at this time what affect, if any, the projectile impact would have on the calculation of the induced stresses. Note that the analysis of induced stresses was first done on cylindrical fatigue test specimens [41]. The stress-strain curves of these specimens had a more dramatic improvement when the smoothing method was applied to calculate the induced strains. This may be due to the more even deposit of coating around the circumference, and no stress concentrations caused by corners.

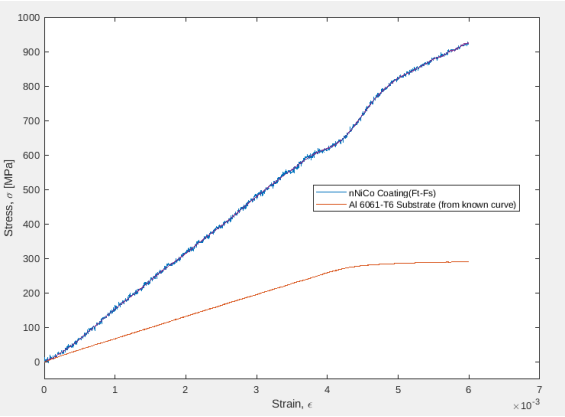

(a)

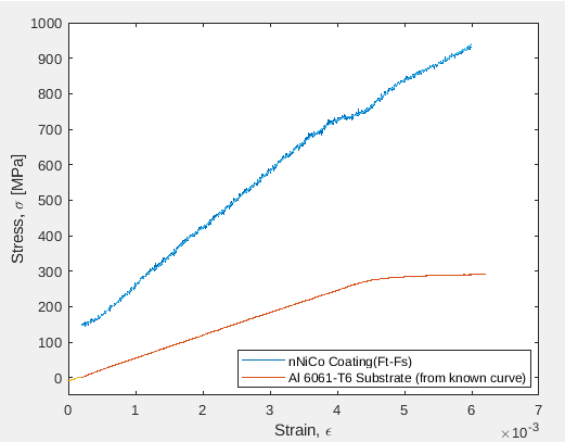

(b) Failure origin points at locations B and C.

Figure 4.54: (a) Substrate and coating stress-strain curves beginning at zero. A non-linearity is seen around 0.4% strain. (b) By shifting the substrate curve along the x-axis, the smoothest curve is determined. At zero stain, the coating has a tensile stress of about 100 MPa, and the substrate has a compressive stress of about 10 MPa.

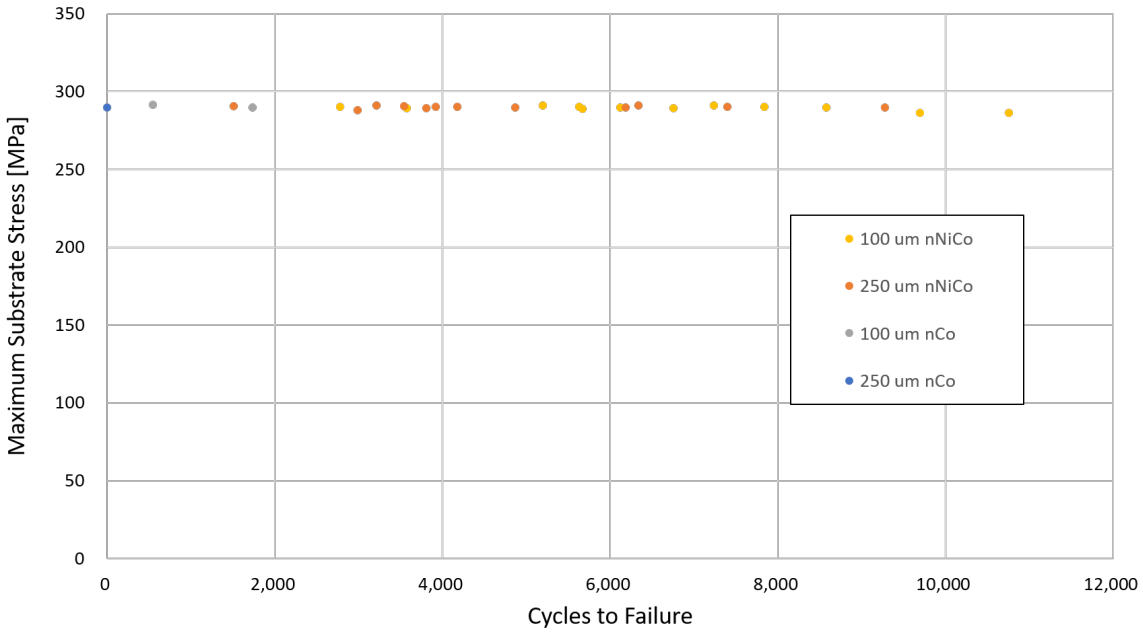

Figure 4.55: Maximum stress in the substrate (including applied and induced) versus cycles to failure for the nNiCo specimens. The substrate stress was very consistent throughout the fatigue tests.

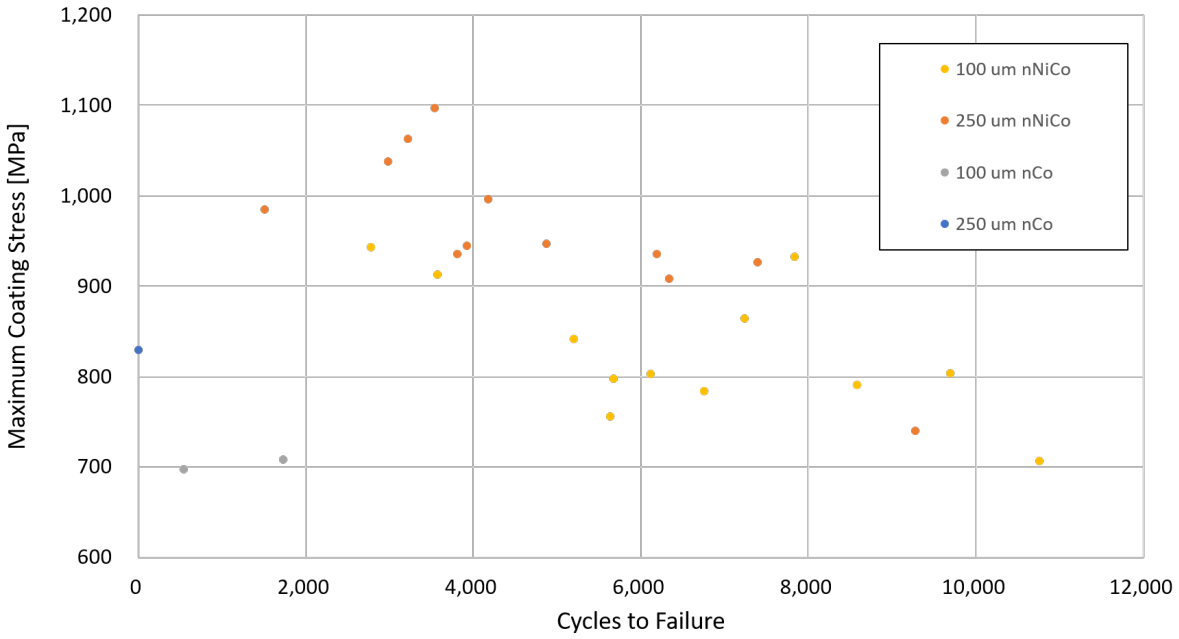

Figure 4.56: Maximum stress in the coating (including applied and induced) versus cycles to failure for the nNiCo specimens. Unlike the substrate stress, there is a correlation between lower coating stress and increased fatigue life.

4.3 Statistical Analysis

From the experimental data, it seems clear that, regardless of impact energy, there is a marked reduction in fatigue lives of the coated specimens compared to the uncoated specimens (Figure 4.1). Among the coated specimens, it also seems evident that the nCo specimens have reduced fatigue lives compared to the nNiCo specimens (Figure 4.2). It seems apparent from Figures 4.55 and 4.56 that the maximum coating stress is relatively strongly correlated to the fatigue life, while the substrate stress is not. However, it is less clear if the is any statistical difference in the fatigue performance between the thin and thick nNiCo coatings, or if the other test variables, including impact energy (Figures 4.2), indentation depth (Figure 4.4), post-impact strain (Figure 4.5), and break location have a significant effect on the fatigue life. In particular, it was expected that there would be a correlation between impact energy and fatigue life, as was found by Draper et al. for example [33]. Therefore, some simple univariate statistical methods have been selected to determine the effect of each variable on the fatigue life using the open-source statistical software RStudio Version 1.2.5019.

Figure 4.57 shows a box plot of the fatigue life data by coating type, with the exception of the single 250 µm nCo specimen E9. The middle 50% of the data for each group are within the grey square, with the whiskers extending to the maximum and minimum values if there are more than two points. The median is represented by the horizontal line and the mean is represented by the "X". These plots show the spread of the data, and how it is concentrated relative to the median. This plot gives an indication of how much better the uncoated specimens behave in fatigue. Note the far right data was conducted at σ_{Smax} of 310 MPa, while all the other tests were conducted at σ_{Smax} of 291 MPa. Figure 4.58 shows box plots of the fatigue lives of the 100 µm nNiCo and 250 µm tests; (a) includes both impact and non-impact specimens (a total of 24 data points), and (b) includes just the impact tests (20 data points). The impact-only data shows there is less spread in the fatigue life data, and the median is skewed lower. Analysis of variance (ANOVA) can be used to calculate the variation between and among groups, and was used by Draper et al. [33] in their analysis of the test variables on post-impact fatigue performance of engine turbine blades. This type of analysis makes several assumptions, including independence within and between groups, equal variance between groups, and normally distributed data [48]. All fatigue tests can be considered independent, since the results of one fatigue test did not influence the results of another. As the standard deviations of the 100 µm nNiCo and 250 µm nNiCo groups are similar, 2444 and 2148 cycles, respectively, the second assumption is considered to have been met. The Shapiro-Wilk test [49] can be used to determine if the data is normally distributed. In RStudio, the `shapiro.test` function calculates two parameters, the w-value and the probability value, or p-value. A w-value of 1.0 indicates the data has a fully normal

distribution. The null hypothesis is that the data is normally distributed, and if the p-value, is less than 0.1 [50], the null hypothesis is rejected [51]. For the nNiCo fatigue data, the w-value was calculated as 0.96365, and the p-value is 0.6191. Thus, according to this test, the distribution of fatigue life is considered to be not significantly different from normal.

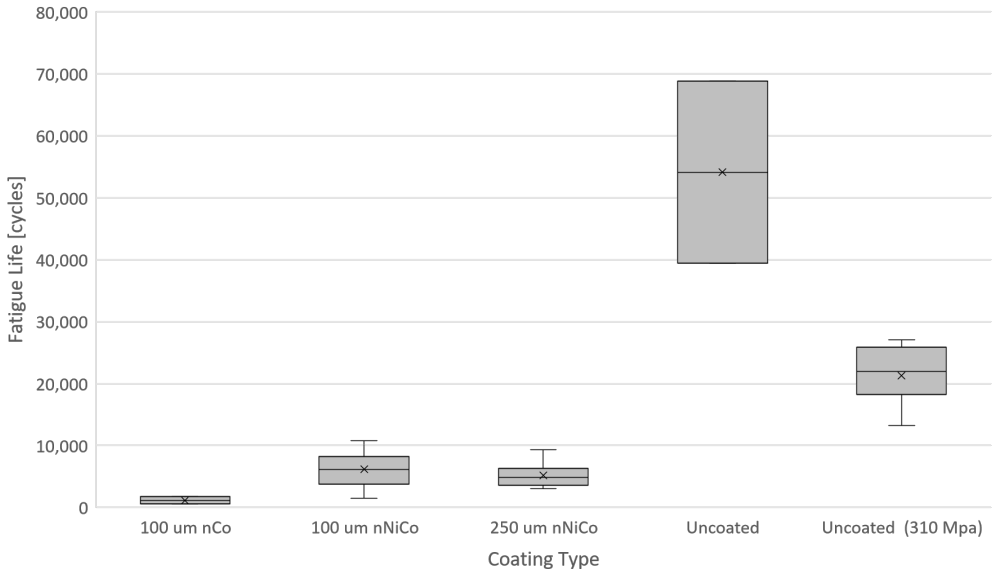

Figure 4.57: Box plot comparing the fatigue life of various coating types. All specimens were included with the exception E9 (250 µm nCo).

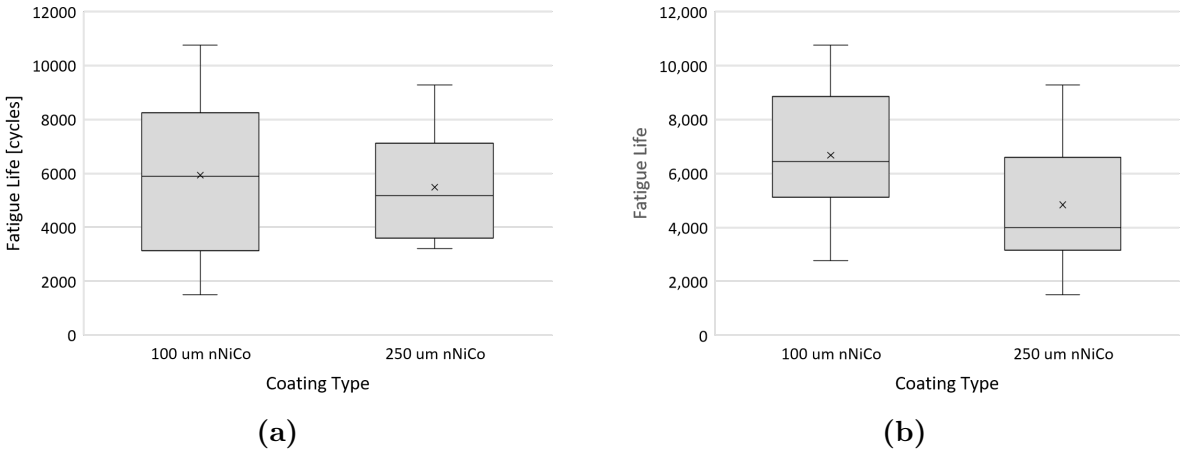

Figure 4.58: Box plots comparing the fatigue life by nNiCo coating thickness for (a) all test specimens and (b) impact test specimens only. The differences between the two groups were determined to be not statistically significant.

In order to determine whether the two nNiCo groups, 100 µm and 250 µm thickness are statistically different with respect to fatigue life, the Kruskal-Wallis test can be used for comparison as this method works with categorical data [48]. It also requires the assumptions

of independence and equal variance, but does not require normality. The null hypothesis is that the groups are equal, and if the calculated p-value is less than 0.05, the null hypothesis is rejected with 95% confidence. The `kruskal.test` function calculated a p-value of 0.1689, which means that the differences in fatigue life between the 100 µm and 250 µm specimens are not statistically significant. Thus both sets of nNiCo fatigue data will be considered as part of one group for the rest of this analysis. The Kruskal-Wallis test can also be used to examine if the break location has a significant effect on the fatigue life. It is classified as either at the impact location, which corresponds to impact energies above 11 J (see Figure 4.48), or near one of the corners (see Figure 4.37). The box plots are shown in Figure 4.59. The `kruskal.test` function calculated a p-value of 0.2159, which means that the two groups are not statistically different with respect to fatigue life, to a greater degree than the coating thickness.

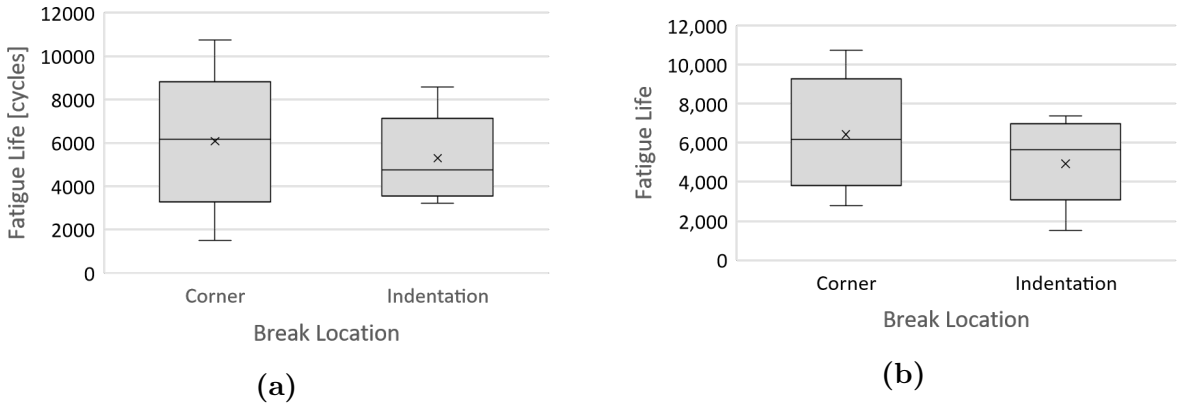

Figure 4.59: Box plots comparing the fatigue life by break location for (a) all test nNiCo specimens and (b) nNiCo impact test specimens only. The differences between the two groups were determined to be not statistically significant.

The `aov` function will produce an ANOVA table for each variable compared with the fatigue life. A full explanation of the contents of the ANOVA table can be found in many sources [48], but of interest here is the p-value. As the break location can also be considered a dependent variable (i.e. a result), the `kruskal.test` was used to compare each numeric variable to the break location. A summary of the p-values for each variable for each test is shown in Table 4.2. The data shows that the total coating stress is the only variable could be considered significant to the fatigue life, with a p-values less than 0.05. The impact energy and coating area have a p-value of less than 0.1 which indicates the null hypothesis can be rejected with 90% confidence that the differences are not due to chance. As the significant p-value is an arbitrary choice [52], these results indicate that impact energy, coating area, and total coating stress all likely have an effect on the fatigue life, while the substrate stress, with a p-value greater than 0.5, likely does not.

Table 4.2: Univariate ANOVA p-value Results for nNiCo Impact Specimens

Variable	ANOVA p-value Fatigue	Kruskal-Wallis p-value Break Location
Impact Energy	0.0834	0.1906
Indentation Depth	0.267	0.2817
Coating Area	0.0904	0.4608
Total Substrate Stress	0.576	0.7509
Total Coating Stress	0.00055	0.4608

The DIC data discussed in Section 4.2.4 was next analysed using the same methods in order determine if the localized post-impact stresses had an effect on the break location. The data is a subset of all impact data with a total of 19 points, including uncoated specimens, and is included in Table 4.3. The impact energy was also included as a comparison, as it is known that the higher energy is correlated with higher strains in the specimen. Table 4.4 shows that the maximum tensile strain (ϵ_t) and compressive strains (ϵ_c) measured through DIC are not significant to the fatigue life or break location outcomes. The maximum strains on the support side have a significant effect on the impact energy as shown by the small p-values (less than 0.05). The maximum tensile strains on the impact side has a significant effect on the fatigue life (p-value of 0.0054).

Table 4.3: Maximum Post-Impact Strains Observed in DIC Images

Variable	Impact side ϵ_c	Impact side ϵ_t	Support side ϵ_c	Support side ϵ_t
P8	-0.0037	0.0109	-0.0056	0.0272
P11	-0.0148	0.0128	-0.019	0.00355
P12	-0.0162	0.0168	-0.021	0.04
H3	-0.00365	0.0032	-0.009	0.0204
H5	-0.00485	0.005	-0.0142	0.0272
H11	-0.0098	0.0094	-0.015	0.0274
H13	-0.0021	0.0031	-0.0112	0.0206
H14	-0.00315	0.0039	-0.0048	0.00625
H16	-0.0435	0.0105	-0.0144	0.0346
F3	-0.00194	0.00114	-0.0012	0.004
F4	-0.00148	0.0018	-0.00245	0.00875
F6	-0.00215	0.005	-0.007	0.0196
F7	-0.00165	0.00395	-0.0078	0.0194
F10	-0.0032	0.00315	-0.011	0.0168
F11	-0.0037	0.00435	-0.0126	0.0156
F12	-0.0015	0.0043	-0.0069	0.0111
F13	-0.00275	0.0053	-0.0088	0.0137
F15	-0.0044	0.00145	-0.0036	0.0116

It is important to note that the number of experiments is relatively small; statistical methods are more robust when there are more data points available, and fatigue data in particular requires large data sets in order to perform proper statistical analysis [38]. These

Table 4.4: Univariate Analysis p-value Results for DIC nNiCo Specimens

Variable	ANOVA p-value Fatigue	ANOVA p-value Impact Energy	Kruskal-Wallis p-value Break Location
Impact side ϵ_c	0.532	0.452	0.5168
Impact side ϵ_t	0.00539	0.102	0.3888
Support side ϵ_c	0.939	2.5e-05	0.4579
Support side ϵ_t	0.653	0.0305	0.5187

results are meant to be taken as an indication the effect of each variable rather than a precise measure. The results of the simple statistical analysis suggest that only the total coating stress is strongly significant in terms of the fatigue life, though impact energy and coating area may have some effect. With more data a two-factor interaction ANOVA could be performed to look at interaction effects between the significant variables. The lack of correlation of any variables to the break location suggests that the root cause lies outside the recorded test data. A limitation of this study was that the fatigue crack growth was not measured, as has been done in other studies [33] [24]. These data may be needed to determine what process or variable dictates the final break location of the fatigue specimens.

Chapter 5

Conclusions and Recommendations

5.1 Summary of Research

In this thesis, the effect of impact damage on the fatigue life of nanocrystalline-coated aluminum was investigated. It was theorized the increased strength, toughness, and hardness of nano materials make them an advantageous alternative to titanium for use in aircraft turbine engine fan blades. To assess the performance of these coatings, the test specimens were subjected to projectile impacts prior to fatigue loading. In total 40 rectangular cross-section specimens were tested, including 13 uncoated aluminum 6061-T6 specimens, 12 100 µm nNiCo specimens, 12 250 µm nNiCo specimens, two 100 µm nCo specimens, and one 250 µm nCo specimens. The impact tests were done using a gas gun with a 2 m barrel with a 9.6 mm inner diameter. Two laser diodes were used to measure the projectile velocity. In total, 26 impact tests were done on an equal number of 100 µm and 250 µm nNiCo specimens, with energy levels ranging from 2.5 to 25 J. Load controlled fatigue tests were run on a MTS 880 uniaxial load frame at either 1.5 or 10 Hz at an R-value of 0.01. The maximum force for all coated specimens corresponded to 0.6% strain in the specimen, measured by a strain gauge glued to the coating, which is a stress of about 291 MPa in the aluminum substrate. Digital image correlation was performed before and after the fatigue tests, and during the fatigue tests to observe the strain field evolution. SEM images of the fracture surfaces were taken after final fracture to investigate the failure origin.

Overall, all coated specimens had substantially shorter fatigue lives than the uncoated specimens; the overall average fatigue life of the uncoated specimens was 26,315 cycles (at σ_{Smax} of 310 MPa) compared to 5160 cycles (at σ_{Smax} of 291 MPa) for the coated specimens. The nNiCo performed better in fatigue than the nCo specimens. The impact energy did not appear to have a strong effect on the fatigue life, and was not found to be a significant to the fatigue life outcome in a univariate analysis. However, all specimens hit with a projectile with an every of above about 11 J broke at the indentation. It was expected that higher impact

energy would be strongly correlated with a lower fatigue life, It was found that the strongest predictor of fatigue life was the total stress in the coating, which included the applied stress and the induced stress. The induced stress likely originate in the electrodeposition process, and may be a benefit or a detriment to the fatigue life depending on whether these stresses are in compression or tension. Coating stress was also the only variable found to be statistically significant to fatigue life, with a p-value less than 0.05. The total stress in the substrate was relatively constant for all tests.

A previous study at UTIAS which looked at the fatigue performance of nNi and nCoP showed that factors such as defects in the substrate or coating, and debonding between of the coating and substrate may lead to low fatigue lives, perhaps lower than the uncoated substrate material. Neither debonding or defects in the aluminum substrate were observed in these experiments. The root cause of the poor performance of the coated specimens in fatigue is thought to be some combination of the geometry, since the coating tends to be thicker at the 90° corners, causing stress concentrations, and from defects observed in the coating. Indentations and nodules on the surface in particular seemed to coincide with failure origin points, as confirmed by SEM images. Voids in the coating likely contributed to the failure of a nCo specimen after one loading cycle. Fatigue tests performed in a parallel experiment on specimens with a cylindrical cross-section showed evidence of the same types of defects. Poor results compared to the uncoated cylindrical specimens often coincided with the presence of defects in the coating. However some specimens had fatigue lives in excess of 200,000 cycles, and these high-life specimens had the lower total coating stress while the subsrate stress remained constant. While the evidence solely on the rectangular cross-section specimens is not promising, the results from the cylindrical tests show that there are advantages to be gained with using these types of nanocrystalline coatings if the coating process can be tightly controlled. The following section discusses some recommendations which might lead to better and more consistent results from these coatings in fatigue loads.

5.2 Recommendation for Future Work

1. Perform more tests to confirm the observed trends, and to ensure a proper statistical analysis can be performed. At least three to six repetitions at every impact energy level would improve the understanding of the results. In addition, varying the load level would allow for a fuller understanding of the stress-strain curve of the coated system.

2. Perform material properties tests on the bulk nanocrystalline material. Results from both tension and fatigue tests on the bulk material would allow for a better understanding of the results from the coated specimens.

3. Control the tolerances on coating thickness during the electroplating process, or have a method of calculating very precise thickness measurements. As the coatings are so thin, even small errors in the measurements are magnified when calculating the stress and properties such as the elastic modulus. Hopefully this might lead to fewer nodules or indentations in the coating.

4. Investigate of how the electrodeposition process can be used to advantageously lower the induced stresses in the coating. One possibility would be to coat one side of the specimen and perform bending tests to calculate the induced stresses more precisely.

5. Use a different specimen cross-section to investigate the post-impact fatigue behaviour, such as an ellipsoid. This shape may promote a more even coating application and reduce the stress concentrations at the corners which seem to be lowering the fatigue life, making it difficult to isolate the effect of the impact damage.

6. Perform impact tests at higher energy levels, up to 40 J or up to projectile velocities of 300 m/s. The required length of the gas gun barrel, projectile diameter and specimen gauge section width need to be considered together when designing the experiment to ensure that the projectile is not too wide.

Bibliography

[1] C. Leyens and M. Peters, eds., *Titanium Alloys for Aerospace Applications: Fundamentals and Applications*. Weinheim: Wiley-VCH, 2003.

[2] B. Cameron, "Encyclopaedia of occupational health and safety 4th edition. chapter 90. aerospace manufacture and maintenance," *http://www.ilocis.org/documents/chpt90e.htm*, Accessed: 2017-11-30.

[3] M. A. Meyers, A. Mishra, and D. J. Benson, "Mechanical properties of nanocrystalline materials," *Progress in materials science*, vol. 51, no. 4, pp. 427–556, 2006.

[4] C. C. Koch, "Structural nanocrystalline materials: an overview," *Journal of Materials Science*, vol. 42, no. 5, pp. 1403–1414, 2007.

[5] S. Tavares and P. De Castro, "An overview of fatigue in aircraft structures," *Fatigue & Fracture of Engineering Materials & Structures*, vol. 40, no. 10, pp. 1510–1529, 2017.

[6] P. Frankel, P. Withers, M. Preuss, H.-T. Wang, J. Tong, and D. Rugg, "Residual stress fields after FOD impact on flat and aerofoil-shaped leading edges," *Mechanics of Materials*, vol. 55, pp. 130–145, 2012.

[7] T. J. Carter, "Common failures in gas turbine blades," *Engineering Failure Analysis*, vol. 12, no. 2, pp. 237–247, 2005.

[8] D. Burot, J. Harris, M. Sakovsky, and C. Steeves, "Fatigue performance of nanocrystalline Ni- or CoP-coated Al 7255," tech. rep., University of Toronto Institute for Aerospace Studies, August 31, 2012.

[9] P. J. G. Dr Edgar Franco, Jialian Wu and P. C. Steeves, "NSERC engage project report: Minimum weight design of nanometal-coated composite pipes," September 13, 2013.

[10] J. J. Gottlieb, "Analytical and numerical studies for the design of a low-speed laboratory projectile launcher," tech. rep., University of Toronto Institute for Aerospace Studies, 2013.

[11] S. Suresh, *Fatigue of Materials*. Cambridge University Press, 2nd ed., 2004.

[12] H. Gleiter, "Nanostructured materials: basic concepts and microstructure," *Acta Materialia*, vol. 48, no. 1, pp. 1–29, 2000.

[13] J. H. Luong, K. B. Male, and J. D. Glennon, "Boron-doped diamond electrode: synthesis, characterization, functionalization and analytical applications," *Analyst*, vol. 134, no. 10, pp. 1965–1979, 2009.

[14] P. Barai and G. J. Weng, "Mechanics of a nanocrystalline coating and grain-size dependence of its plastic strength," *Mechanics of Materials*, vol. 43, no. 9, pp. 496–504, 2011.

[15] R. Zhu, X. Zhang, Y. Li, and J. Zhou, "Impact behavior and constitutive model of nanocrystalline Ni under high strain rate loading," *Materials & Design*, vol. 49, pp. 426–432, 2013.

[16] J. R. Trelewicz and C. A. Schuh, "The Hall–Petch breakdown at high strain rates: optimizing nanocrystalline grain size for impact applications," *Applied Physics Letters*, vol. 93, no. 17, p. 171916, 2008.

[17] R. A. Prado and J. Benfer, "Nanocrystalline coatings provide hard chrome alternative," *https://www.serdp-estcp.org/News-and-Events/Blog/Nanocrystalline-Coatings-Provide-Hard-Chrome-Alternative*, Accessed: 2017-11-30.

[18] C. Ma, S. Wang, and F. Walsh, "The electrodeposition of nanocrystalline cobalt–nickel–phosphorus alloy coatings: a review," *Transactions of the IMF*, vol. 93, no. 5, pp. 275–280, 2015.

[19] K. Mroz, A. Bigos, S. Kucharski, K. Dolinski, and E. Bełtowska-Lehman, "Ni-W electrodeposited coatings on low carbon steel substrate: fatigue observations," *Journal of Materials Engineering and Performance*, vol. 23, no. 10, pp. 3459–3466, 2014.

[20] S. Zhang and X. Zhang, "Toughness evaluation of hard coatings and thin films," *Thin Solid Films*, vol. 520, no. 7, pp. 2375–2389, 2012.

[21] J. G. Kaufman, *Properties of aluminum alloys: fatigue data and the effects of temperature, product form, and processing*. ASM International, 2008.

[22] J. T.-P. Yao and W. Munse, "Low-cycle fatigue of metals," *Literature Review*, 1961.

[23] P. Chowdhury and H. Sehitoglu, "Mechanisms of fatigue crack growth–a critical digest of theoretical developments," *Fatigue & Fracture of Engineering Materials & Structures*, vol. 39, no. 6, pp. 652–674, 2016.

[24] H. Padilla and B. Boyce, "A review of fatigue behavior in nanocrystalline metals," *Experimental Mechanics*, vol. 50, no. 1, pp. 5–23, 2010.

[25] K.-D. Bouzakis, G. Skordaris, E. Bouzakis, S. Makrimallakis, S. Kombogiannis, and O. Lemmer, "Fatigue strength of diamond coatings' interface assessed by inclined impact test," *Surface and Coatings Technology*, vol. 237, pp. 135–141, 2013.

[26] N. Rossini, M. Dassisti, K. Benyounis, and A.-G. Olabi, "Methods of measuring residual stresses in components," *Materials & Design*, vol. 35, pp. 572–588, 2012.

[27] A. El-Sherik, J. Shirokoff, and U. Erb, "Stress measurements in nanocrystalline Ni electrodeposits," *Journal of Alloys and Compounds*, vol. 389, no. 1-2, pp. 140–143, 2005.

[28] S. Pathak, M. Guinard, M. G. Vernooij, B. Cousin, Z. Wang, J. Michler, and L. Philippe, "Influence of lower current densities on the residual stress and structure of thick nickel electrodeposits," *Surface and Coatings Technology*, vol. 205, no. 12, pp. 3651–3657, 2011.

[29] S. Hadian and D. Gabe, "Residual stresses in electrodeposits of nickel and nickel–iron alloys," *Surface and Coatings Technology*, vol. 122, no. 2-3, pp. 118–135, 1999.

[30] T. Borvik, M. Langseth, O. S. Hopperstad, and K. A. Malo, "Perforation of 12 mm thick steel plates by 20 mm diameter projectiles with flat, hemispherical and conical noses - part i: Experimental study," *International Journal of Impact Engineering*, vol. 27, no. 1, pp. 19–35, 2001. Cited By :178.

[31] F. Morinire, R. Alderliesten, and R. Benedictus, "Modelling of impact damage and dynamics in fibre-metal laminates a review," *International Journal of Impact Engineering*, vol. 67, no. Supplement C, pp. 27 – 38, 2014.

[32] Z. Li, R. Feng, Y. Wang, and L. Wang, "Experimental study on the effect of dents induced by impact on the fatigue life of 2024-t3 aluminum alloy plate," *Engineering Structures*, vol. 137, pp. 236–244, 2017.

[33] S. Draper, M. Nathal, B. Lerch, J. Pereira, C. Austin, and O. Erdmann, "The effect of ballistic impacts on the high-cycle fatigue properties of ti-48al-2nb-2cr (atomic percent)," *Metallurgical and Materials Transactions A*, vol. 32, no. 11, pp. 2743–2758, 2001.

[34] H. Jiang, M. Rühle, and E. Lavernia, "On the applicability of the x-ray diffraction line profile analysis in extracting grain size and microstrain in nanocrystalline materials," *Journal of Materials Research*, vol. 14, no. 2, pp. 549–559, 1999.

[35] A. Karimpoor, K. Aust, and U. Erb, "Charpy impact energy of nanocrystalline and polycrystalline cobalt," *Scripta materialia*, vol. 56, no. 3, pp. 201–204, 2007.

[36] G. Skordaris, "Temperature-dependent fatigue strength of diamond coating-substrate interface quantified via the shear failure stress," *Journal of Materials Engineering and Performance*, vol. 24, no. 9, pp. 3335–3342, 2015.

[37] G. Skordaris, "Quantification of PVD film adhesion with critical shear stress by using dynamic simulation of the inclined impact test," *Journal of Materials Rngineering and Performance*, vol. 22, no. 11, pp. 3192–3198, 2013.

[38] J. Schijve, "Statistical distribution functions and fatigue of structures," *International Journal of Fatigue*, vol. 27, no. 9, pp. 1031–1039, 2005.

[39] A. E466-15, "Standard practice for conducting force controlled constant amplitude axial fatigue tests of metallic materials," *ASTM Int.*, 2015.

[40] E. M. Jones, "A good practices guide for digital image correlation," *International Digital Image Correlation Society*, 2018.

[41] S. Cheung, "Predicting the fatigue life of nanometal-coated aluminum," *Master's dissertation, University of Toronto, Toronto, ON*, In progress.

[42] H. Mughrabi, H. Höppel, and M. Kautz, "Fatigue and microstructure of ultrafine-grained metals produced by severe plastic deformation," *Scripta Materialia*, vol. 51, no. 8, pp. 807–812, 2004.

[43] F. Cardarelli, *Materials Handbook: A Concise Desktop Reference*. Springer Science & Business Media, 2008.

[44] J. Giallonardo, U. Erb, K. Aust, and G. Palumbo, "The influence of grain size and texture on the Young's modulus of nanocrystalline nickel and nickel–iron alloys," *Philosophical Magazine*, vol. 91, no. 36, pp. 4594–4605, 2011.

[45] S. K. Paul and S. Tarafder, "Cyclic plastic deformation response at fatigue crack tips," *International Journal of Pressure Vessels and Piping*, vol. 101, pp. 81–90, 2013.

[46] S. Rabbolini, P. G. Luccarelli, S. Beretta, S. Foletti, and H. Sehitoglu, "Near-tip closure and cyclic plasticity in ni-based single crystals," *International Journal of Fatigue*, vol. 89, pp. 53–65, 2016.

[47] N. Brown, "Effect of shot peening prior to electroplating on the fatigue properties of an alloy steel," *Department of Mines and Technical Surveys, Canadian Government Publications*, vol. R23, 1958.

[48] D. L. Hahs-Vaughn and R. G. Lomax, *Statistical Concepts - A Second Course*. Routledge, 2013.

[49] S. Shaphiro and M. Wilk, "An analysis of variance test for normality," *Biometrika*, vol. 52, no. 3, pp. 591–611, 1965.

[50] "R Studio Documentation," *https://www.rdocumentation.org*, Accessed: 2019-12-09.

[51] P. Royston, "Remark AS R94: A remark on algorithm AS 181: The w-test for normality," *Journal of the Royal Statistical Society. Series C (Applied Statistics)*, vol. 44, no. 4, pp. 547–551, 1995.

[52] M. Cowles and C. Davis, "On the origins of the 0.05 level of statistical significance.," *American Psychologist*, vol. 37, no. 5, p. 553, 1982.